

South Dakota State University

# Open PRAIRIE: Open Public Research Access Institutional Repository and Information Exchange

---

Theses and Dissertations

---


2016

## Urea Pre-treatment of N<sub>2</sub>-annealed Transition Metal Oxides for Low Cost and Efficient Counter Electrodes in Dye-sensitized Solar Cell

Hytham Elbohy

*South Dakota State University*

Follow this and additional works at: <http://openprairie.sdstate.edu/etd>

 Part of the [Electrical and Computer Engineering Commons](#), [Engineering Science and Materials Commons](#), and the [Materials Science and Engineering Commons](#)

---

### Recommended Citation

Elbohy, Hytham, "Urea Pre-treatment of N<sub>2</sub>-annealed Transition Metal Oxides for Low Cost and Efficient Counter Electrodes in Dye-sensitized Solar Cell" (2016). *Theses and Dissertations*. 1096.

<http://openprairie.sdstate.edu/etd/1096>

This Dissertation - Open Access is brought to you for free and open access by Open PRAIRIE: Open Public Research Access Institutional Repository and Information Exchange. It has been accepted for inclusion in Theses and Dissertations by an authorized administrator of Open PRAIRIE: Open Public Research Access Institutional Repository and Information Exchange. For more information, please contact [michael.biondo@sdstate.edu](mailto:michael.biondo@sdstate.edu).

UREA PRE-TREATMENT OF N<sub>2</sub>-ANNEALED TRANSITION METAL OXIDES  
FOR LOW COST AND EFFICIENT COUNTER ELECTRODES IN DYE-  
SENSITIZED SOLAR CELL

BY

HYTHAM ELBOHY

A dissertation submitted in partial fulfillment of the requirements for the

Doctor of Philosophy

Major in Electrical Engineering

South Dakota State University

2016



## ACKNOWLEDGEMENT

My deep gratitude goes first to Dr. Qiquan Qiao as dissertation advisor, who expertly guided and supported me through my PhD research at the Center of Advanced Photovoltaics, South Dakota State University. His valuable suggestions and continuous encouragements have helped me to conduct my research successfully and attain skills to be an independent researcher.

My appreciations extend to Dr. David Galipeau, Dr. Cheng Zhang, Dr. Huitian Lu, and Dr. Hyeun Joong Yoon for their important role and support as committee members.

I am also grateful to Dr. Steven Hietpas and the Department of Electrical Engineering at South Dakota State University for extending all the administrative support so that I can carry out my PhD dissertation research.

I am thankful to all my colleagues, especially Prashant Poudel, Amit Thapa, Swaminathan Venkatesan, Ashish Dubey, Nirmal Adhikari, Bjorn Vaagensmith, Khan Mamun Reza and Eman Gamal in helping me to complete my experiments.

Finally, I am grateful to my family for their constant support, patience during my PhD studies.

## TABLE OF CONTENTS

LIST OF FIGURES	viii
LIST OF TABLES	xii
ABSTRACT	xiii
<b>Chapter 1: Introduction</b>	<b>1</b>
1.1 Background	1
1.2 Previous Work	5
1.2.1 Carbon materials	7
1.2.2 Polymers	9
1.2.3 Metal compounds	12
1.3 Motivation	16
1.4 Objectives	16
<b>Chapter 2: Theory</b>	<b>18</b>
2.1 Solar cell configuration and operation principles	18
2.1.1 Silicon Solar Cells	
2.2 Operating principle of dye-sensitized solar cells (DSSCs) and charge transfer kinetics in DSSCs	22
2.3 Solar cell efficiency and processes that govern performance	25
2.4 Kinetics of triiodide reduction reaction at counter electrodes	29
2.5 Cyclic voltammetry	29
2.6 Electrochemical impedance spectroscopy	32
2.7 UV-Vis absorption spectroscopy	34

2.8	Mott-Schottky analysis	36
2.9	Urea reaction mechanism with metal oxide at high temperatures	38
2.10	Oxygen vacancies effect on the band gap diagram of metal oxide	39
<b>Chapter 3: Experimental Procedures</b>		<b>41</b>
3.1	Materials and Device fabrication procedures	41
3.1.1	Materials	41
3.1.2	Counter electrode fabrication	41
3.1.3	Photoanode fabrication	44
3.1.4	Dye-sensitized solar cell device assembly	45
3.2	Materials and Device characterizations	47
3.2.1	UV-Visible absorbance spectra	48
3.2.2	Raman Spectroscopy	49
3.2.3	Scanning electron microscopy	49
3.2.4	Current-voltage (I-V) characterizations	49
3.2.5	Electrochemical impedance spectroscopy	51
3.2.6	Cyclic voltammetry and Mott-Schottky measurements	53
<b>Chapter 4: Results and Analysis</b>		<b>54</b>
4.1	Scanning electron microscopy (SEM) and Energy dispersive X-ray spectroscopy (EDS)	54
4.1.1	SEM and EDS for WO <sub>3</sub> counter electrode films before and after urea-pretreatment	54
4.1.2	SEM and EDS for SnO <sub>2</sub> counter electrode films before and after urea-pretreatment	56

4.1.3	SEM and EDS for ZnO counter electrode films before and after urea-pretreatment	59
4.2	Mott-Schottky measurement for Band structure analysis	62
4.2.1	Mott-Schottky plot for n-type WO <sub>3</sub> metal oxide in triiodide/iodide electrolyte	62
4.2.2	Mott-Schottky plot for n-type SnO <sub>2</sub> metal oxide in triiodide/iodide electrolyte	63
4.2.3	Mott-Schottky plot for n-type ZnO metal oxide in triiodide/iodide electrolyte	65
4.3	Raman spectroscopy analysis	68
4.3.1	Raman spectroscopy for WO <sub>3</sub> counter electrode films before and after urea pre-treatment	68
4.3.2	Raman spectroscopy for SnO <sub>2</sub> counter electrode films before and after urea pre-treatment	69
4.3.3	Raman spectroscopy for ZnO counter electrode films before and after urea pre-treatment	71
4.4	Optical band gap determination	72
4.4.1	Optical band gap values of WO <sub>3</sub> counter electrode films before and after urea pre-treatment	72
4.4.2	Optical band gap values of SnO <sub>2</sub> counter electrode films before and after urea pre-treatment	73
4.4.3	Optical band gap values of ZnO counter electrode films before and after urea pre-treatment	75
4.5	Cyclic voltammetry	76
4.5.1	Cyclic voltammetry measurements of WO <sub>3</sub> counter electrode films before and after urea pre-treatment.	78
4.5.2	Cyclic voltammetry measurements of SnO <sub>2</sub> counter electrode films before and after urea pre-treatment.	80
4.5.3	Cyclic voltammetry measurements of ZnO counter electrode films before and after urea pre-treatment.	82

4.6	Electrochemical impedance spectroscopy (EIS)	83
4.6.1	Electrochemical impedance spectroscopy of $\text{WO}_3$ counter electrode films before and after urea pre-treatment	83
4.6.2	Electrochemical impedance spectroscopy of $\text{SnO}_2$ counter electrode films before and after urea pre-treatment	86
4.6.3	Electrochemical impedance spectroscopy of $\text{ZnO}$ counter electrode films before and after urea pre-treatment	88
4.7	Current-Voltage characteristics (J-V)	91
4.7.1	Current-Voltage characteristics of $\text{WO}_3$ counter electrode films before and after urea pre-treatment	92
4.7.2	Current-Voltage characteristics of $\text{SnO}_2$ counter electrode films before and after urea pre-treatment	95
4.7.3	Current-Voltage characteristics of $\text{ZnO}$ counter electrode films before and after urea pre-treatment	99
<b>Chapter 5</b>	<b>Conclusions</b>	105
5.1	Summary	105
5.2	Conclusions	108
5.3	Future work	109
<b>References</b>		110



## LIST OF FIGURES

Figure 1.1	Types of energy sources and percentage of energy consumption in U. S. in 2016 (compiled by Institute for Energy Research, IER 2016).	3
Figure 1.2	Best research solar cell efficiency reported over the last three decades (compiled by national Renewable Energy Laboratory, 2016).	4
Figure 2.1	Solar irradiance spectrum.	19
Figure 2.2	The Device structure of passivated emitter, rear locally diffused (PERL) single crystalline silicon solar cell.	20
Figure 2.3	Band diagram of a p-n junction solar cell.	21
Figure 2.4	Schematic of DSSC.	23
Figure 2.5	Schematic of DSSC with energy level diagram. The dye is electronically excited after absorption of a light photon raising an electron from the highest occupied molecular orbital (HOMO) energy level of the dye to the lowest unoccupied molecular orbital (LUMO) energy level.	23
Figure 2.6	The plot of the J-V curve resulting from both (—) dark and (—) light current. The efficiency parameters are also labeled. Dashed lines identify the area used to calculate fill factor.	26
Figure 2.7	The equivalent circuit of the solar cell.	27
Figure 2.8	J-V curve with arrows showing the effects that series and shunt resistances have on the curve's appearance. A dashed line represents zero current density.	28
Figure 2.9	Schematic of a reaction at a counter electrode.	29
Figure 2.10	Schematic of an electrode reaction.	30
Figure 2.11	A cyclic potential sweep. (b) A cyclic voltammogram.	31
Figure 2.12	(a) Energy level diagram of the electrode and species, O without application of the potential. (b) Energy level diagram of the electrode and species after application of a negative	32

	potential (reduction process). (C) Energy level diagram of the electrode and species after application of positive potential (oxidation process).	
Figure 2.13	(a) Nyquist plot of a symmetrical cell. (b) An equivalent circuit of the symmetrical cell for the fitting of the Nyquist plot.	33
Figure 2.14	The possible electronic transitions of $\pi$ , $\sigma$ , and n electrons.	34
Figure 2.15	Absorption of light by a solution of absorbing material.	35
Figure 2.16	Band structure for iodide/triiodide ( $I^-/I_3^-$ ) and n-type metal oxide before and after contact.	37
Figure 2.17	The effect of oxygen vacancies on metal oxide band diagram.	40
Figure 3.1	Different counter electrodes fabricated of pristine films (P-WO <sub>3</sub> , P-SnO <sub>2</sub> and P-ZnO), N <sub>2</sub> -annealed films (N-WO <sub>3</sub> , N-SnO <sub>2</sub> , and N-ZnO) and Urea pretreated N <sub>2</sub> -annealed film with different urea wt% of urea pre-treated metal oxides (U3, U5, U9, U16, and U33).	43
Figure 3.2	Schematic of DSSC device assembly.	46
Figure 3.3	An example of Tauc plot.	48
Figure 3.4	Schematic of UV-Visible absorption spectroscopy.	48
Figure 3.5	Photograph of Current density-voltage measurement setup.	50
Figure 3.6	Schematic of a symmetrical electrochemical cell used for EIS measurement.	51
Figure 3.7	The functional diagram of an EIS experiment.	52
Figure 3.8	Functional diagram of a cyclic voltammetry (CV).	53
Figure 4.1	SEM images for pristine WO <sub>3</sub> (P-WO <sub>3</sub> ), N <sub>2</sub> -annealed WO <sub>3</sub> (N-WO <sub>3</sub> ) and urea pre-treated N <sub>2</sub> -annealed WO <sub>3</sub> with different urea wt% (U3-WO <sub>3</sub> , U5-WO <sub>3</sub> , U9-WO <sub>3</sub> , U16-WO <sub>3</sub> , and U33-WO <sub>3</sub> ).	55

Figure 4.2	Oxygen wt% for $\text{WO}_3$ film before and after urea pre-treatment with different urea wt%.	56
Figure 4.3	SEM images for pristine $\text{SnO}_2$ (P- $\text{SnO}_2$ ), $\text{N}_2$ -annealed $\text{SnO}_2$ (N- $\text{SnO}_2$ ) and urea pre-treated $\text{N}_2$ -annealed $\text{SnO}_2$ with different urea wt% (U3- $\text{SnO}_2$ , U5- $\text{SnO}_2$ , U9- $\text{SnO}_2$ , U16- $\text{SnO}_2$ , and U33- $\text{SnO}_2$ ).	57
Figure 4.4	Oxygen Wt% for $\text{SnO}_2$ film before and after urea pre-treatment with different urea wt%.	59
Figure 4.5	SEM images for pristine $\text{ZnO}$ (P- $\text{ZnO}$ ), $\text{N}_2$ -annealed $\text{ZnO}$ (N- $\text{ZnO}$ ) and urea pre-treated $\text{N}_2$ -annealed $\text{SnO}_2$ with different urea wt% (U3- $\text{ZnO}$ , U5- $\text{ZnO}$ , U9- $\text{ZnO}$ , U16- $\text{ZnO}$ , and U33- $\text{ZnO}$ ).	60
Figure 4.6	Oxygen Wt% for $\text{SnO}_2$ film before and after urea pre-treatment with different urea wt%.	61
Figure 4.7	Mott-Schottky plot for $\text{WO}_3$ counter electrode before and after urea pre-treatment with different urea wt%.	63
Figure 4.8	Mott-Schottky plot for $\text{SnO}_2$ counter electrode before and after urea pre-treatment with different urea wt%	65
Figure 4.9	Mott-Schottky plot for $\text{ZnO}$ counter electrode before and after urea pre-treatment with different urea wt%.	67
Figure 4.10	Raman spectroscopy of $\text{WO}_3$ counter electrode before and after urea pre-treatment with different urea wt%.	69
Figure 4.11	Raman spectroscopy of $\text{SnO}_2$ counter electrode before and after urea pre-treatment with different urea wt%.	70
Figure 4.12	Raman spectroscopy of $\text{ZnO}$ counter electrode before and after urea pre-treatment with different urea wt%.	71
Figure 4.13	Tauc plot for $\text{WO}_3$ before and after urea pre-treatment with different urea wt%.	73
Figure 4.14	Tauc plot for $\text{SnO}_2$ before and after urea pre-treatment with different urea wt%.	74
Figure 4.15	Tauc plot for $\text{ZnO}$ before and after urea pre-treatment with different urea wt%.	76

Figure 4.16	Cyclic voltammetry plot for iodide/triiodide electrolyte.	77
Figure 4.17	Cyclic voltammetry plot for iodide/triiodide electrolyte with $\text{WO}_3$ counter electrode before and after urea pre-treatment with different urea wt%.	79
Figure 4.18	Cyclic voltammetry plot for iodide/triiodide electrolyte with $\text{SnO}_2$ counter electrode before and after urea pre-treatment with different urea wt%.	81
Figure 4.19	Cyclic voltammetry plot for iodide/triiodide electrolyte with $\text{ZnO}$ counter electrode before and after urea pre-treatment with different urea wt%.	83
Figure 4.20	Equivalent circuit used of symmetric dummy cell used for EIS measurement modeling and fitting.	84
Figure 4.21	Nyquist plot for symmetrical dummy cells of $\text{WO}_3$ counter electrode before and after urea pre-treatment with different urea wt%.	86
Figure 4.22	Nyquist plot for symmetrical dummy cells of $\text{SnO}_2$ counter electrode before and after urea pre-treatment with different urea wt%.	88
Figure 4.23	Nyquist plot for symmetrical dummy cells of $\text{ZnO}$ counter electrode before and after urea pre-treatment with different urea wt%.	90
Figure 4.24	Current density-voltage ( $J$ - $V$ ) for DSSC devices with $\text{WO}_3$ CEs before and after urea treatment with different urea wt% in comparison with Pt CE based devices.	94
Figure 4.25	Current density-voltage ( $J$ - $V$ ) for DSSCs devices with U5- $\text{WO}_3$ CEs with different thicknesses.	95
Figure 4.26	Current density-voltage ( $J$ - $V$ ) for DSSC devices with $\text{SnO}_2$ CEs before and after urea treatment with different urea wt% in comparison with Pt CE based devices	97
Figure 4.27	Current density-voltage ( $J$ - $V$ ) for DSSCs devices with U9- $\text{SnO}_2$ CEs with different thicknesses.	98

Figure 4.28	Current density-voltage ( $J$ - $V$ ) for DSSC devices with ZnO CEs before and after urea treatment with different urea wt% in comparison with Pt CE based devices.	101
Figure 4.29	Current density-voltage ( $J$ - $V$ ) for DSSCs devices with U16-ZnO CEs with different thicknesses.	102

#### LIST OF TABLES

Table 4.1	Flat band potential values ( $V_{fb}$ ) calculated from Mott-Schottky plot for $WO_3$ , $SnO_2$ , and ZnO CEs before and after urea treatment with different wt%.	70
Table 4.2	EIS fitted parameters extracted from Nyquist plots of respective dummy cells with $WO_3$ , $SnO_2$ , and ZnO CEs before and after urea treatment with different wt% in comparison with Pt CE based device.	96
Table 4.3	The performance of DSSC devices based on $WO_3$ , $SnO_2$ , and ZnO CEs before and after urea treatment with different wt% in comparison to Pt CE based device.	110

## ABSTRACT

UREA PRE-TREATMENT OF N<sub>2</sub>-ANNEALED TRANSITION METAL OXIDES FOR  
LOW COST AND EFFICIENT COUNTER ELECTRODES IN DYE-SENSITIZED  
SOLAR CELLS

HYTHAM ELBOHY

2016

Photovoltaic cells have shown great promise as an alternative to fossil fuel-based energy sources. Dye-sensitized solar cells (DSSCs) have shown potential as low-cost replacement to silicon solar cells owing to their reduced material costs and simple fabrication techniques. Platinum (Pt) was used as a catalyst in the counter electrode for DSSCs. Metal oxides have been used as an alternative material to Pt. The introduction of oxygen vacancies inside metal oxides helps to facilitate electron transport to the electrolyte to enhance the reduction process of triiodide ions. Annealing n-type metal oxides under a reducing agent gas such as hydrogen (H<sub>2</sub>) at temperature  $\geq 400$  °C helps to introduce more oxygen vacancies. In this dissertation, a novel method was developed to convert the electro-catalytically inactive commercial n-type WO<sub>3</sub>, SnO<sub>2</sub>, and ZnO into highly active WO<sub>3-x</sub>, SnO<sub>2-x</sub> and ZnO<sub>1-x</sub> as counter electrodes (CEs) for DSSCs. These new metal oxides replaced Pt by controlling the number of introduced oxygen vacancies. All the metal oxides including WO<sub>3</sub>, SnO<sub>2</sub>, and ZnO were pre-treated with urea at different wt% before annealing under N<sub>2</sub> environment at 470 °C for 2 hr. At high temperatures (e.g., 300-400

°C), urea easily decomposes to ammonia which then decomposes to H<sub>2</sub> and N<sub>2</sub> gases. Higher wt% of urea leads to more reducing H<sub>2</sub> gas and hence helps to create more oxygen vacancies. The urea treatment significantly improved the catalytic activity of all metal oxides, and solar cell power conversion efficiency (PCE) of DSSCs was increased by urea pre-treatment. All other characterizations including SEM, EDS, and Mott-Schottky performed for urea pre-treatment of WO<sub>3</sub>, SnO<sub>2</sub> and ZnO support the hypothesis that urea treatment helps create oxygen vacancies (shallow defects states) in metal oxides. These oxygen vacancies facilitate the redox process in the iodide/triiodide electrolyte. The density of these oxygen vacancies can be engineered by controlling the urea wt% during the treatment. Compared to previous work by only annealing metal oxides in N<sub>2</sub> or H<sub>2</sub> without any pre-treatment, this new method using urea pre-treatment is more efficient to maximize the performance of DSSC devices.

## Chapter 1: Introduction

### 1.1 Background

The demand of energy has skyrocketed over centuries throughout the world. Current energy consumption of the world is over ten terawatts (TW) and expected to increase over 30 TW by 2050 [1]. The majority of energy consumption is manifested by fossil fuels such as coal and natural gas. However, fossil fuels have main drawbacks including adverse environmental impacts and limited resources [1]. The emission of CO<sub>2</sub> has detrimental effects on the environment including global warming [2]. More CO<sub>2</sub> in the air also leads to more CO<sub>2</sub> in the ocean, which is known to acidify the water, causing the breakdown of coral reefs. These are significant reasons to transit from fossil fuels to alternative clean and sustainable sources of energy.

Alternative energy sources include nuclear, hydrothermal, biomass, wind, and solar energy. Each has advantages and disadvantages. Currently, only 5% of the world's energy (20% in the U. S.) comes from nuclear [3, 4]. For nuclear, a large amount of uranium and power plants are required to meet the energy demand. The disadvantages are the nuclear waste and only 40-year lifetime of each plant on average. To meet the current energy consumption, new nuclear plant facilities need to be built every year for the next 30 years, without considering the plants that need to be decommissioned [4].

Biomass, which is generated from plant-based materials, can be a carbon neutral source [5] and supports U. S. agricultural industries. Unfortunately, biomass is a fuel that needs to be manufactured for use and still produces carbon dioxide during the processing. Geothermal utilizes thermal energy in the earth's deep reservoirs. There is a limited source of geothermal. Availability is a hindrance because it only occurs in certain regions.



Utilization of geothermal does not directly generate greenhouse gasses, but there is a fear of the releasing of harmful gasses. Also, it may adversely affect geyser and hot springs activities in these regions [6]. The advantages of using wind energy are that it exists naturally and just needs to be captured/converted into electrical energy and it produces no detrimental effects. However, wind energy is location-dependent. Dams are a form of hydroelectric energy. The hydropower can start and stop during their use, and store energy for future need. Other environmental benefits from dams include water reservoir for irrigation and lakes for recreation.

Solar energy has a similar advantage to wind as the energy naturally occurs and only needs to be captured and converted into electricity. The advantage of solar energy is that it is a permanent source of energy. A total of 120,000 TW of power strikes the earth continuously where only about 13 TW of energy are needed [7]. The disadvantage is the need for storing the energy that is not immediately used because the amount of sunlight varies day to day and there is no sunlight at night. According to Institute for Energy Research (IER) in the United States, only 0.5% of the total power consumption is supplied by solar energy in 2016 as shown in figure1.1.

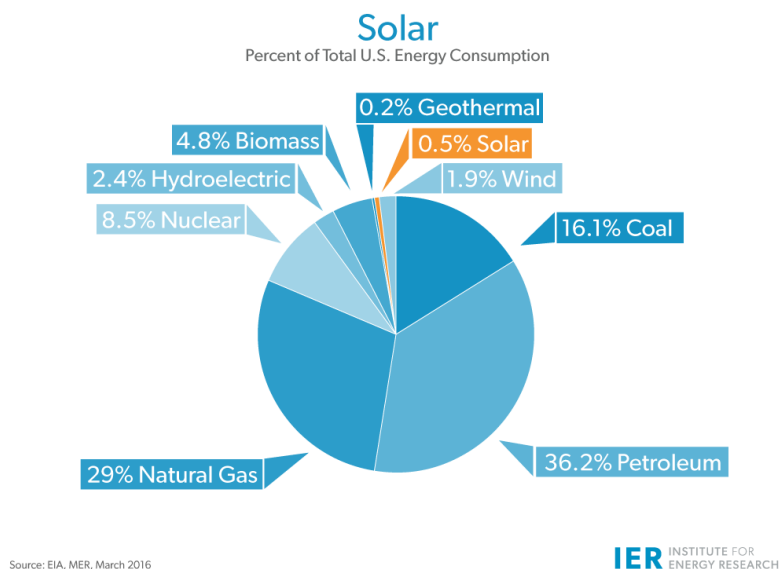


Figure 1.1 Types of energy sources and percentage of energy consumption in U. S. in 2016 (Source: Institute for Energy Research, IER 2016).

The photovoltaic effect was observed for the first time in 1839 by Becquerel [8] where he discovered a current in AgCl solution when illuminated with the light. The first solid state solar cell based on selenium foils was reported by Fritts in 1883 [9] with power conversion efficiency (PCE) lower than 1 %. The major improvement in photovoltaic cells was reported in 1954 [10] by Chapin, Fuller and Pearson at Bell Labs with 6% PCE based on silicon p-n junction. Since then, an enormous number of studies have been conducted to enhance the silicon solar cell efficiency reaching beyond 24% [11] for solar cells based on single crystalline silicon and beyond 20% [12] for solar cells based on polycrystalline silicon.

Photovoltaic cells convert sunlight directly into electricity. Current photovoltaic cells in the market are silicon based solar cells [13, 14]. Crystalline silicon (c-Si) solar cells are not economical due to its high cost of raw materials and production. The c-Si solar cells

require high purity silicon wafers and sophisticated vacuum fabrication processing. To overcome this problem, thin film and organic materials based solar cells were proposed and fabricated. Figure 1.2 shows the highest reported efficiency trends for different types of solar cells fabricated in research laboratories from 1975 to 2016. Several types of solar cells are shown such as single and multi-junction GaAs, crystalline silicon, thin film CIGS and CdTe, dye-sensitized, polymer, perovskite and quantum dot solar cells. Some of the observed efficiencies include 24.7% for monocrystalline Si solar cells, 44.4% for multi-junction InGaAs/GaAs/InGaP, 20.4% for CdTe solar cells, 11.9% for DSSCs and 10.6% for tandem polymer solar cells.

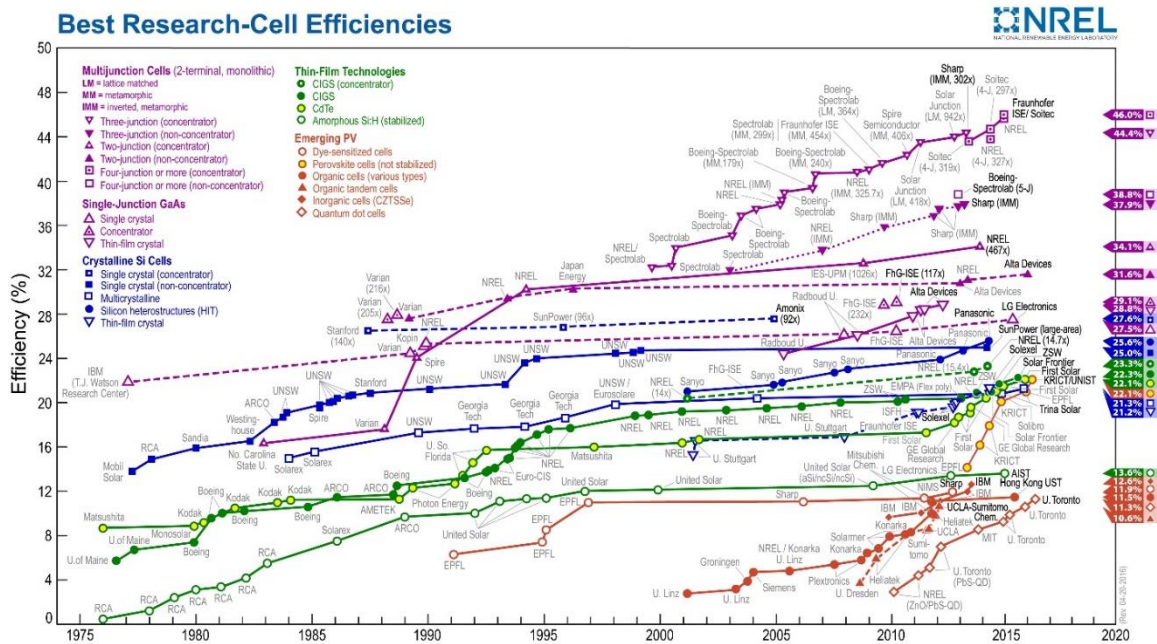


Figure 1.2 Best research solar cell efficiency reported over the last three decades (compiled by National Renewable Energy Laboratory, 2016).

Materials such as amorphous silicon (a-Si), copper indium gallium selenide (CIGS), cadmium tellurium (CdTe) have shown promise as alternatives to c-Si to reduce

material cost as these films are orders of magnitude thinner than c-Si solar cells. Solar cells using these materials have shown moderate efficiency (6-20%) [15] in labs but have failed to compete against c-Si due to several limitations such as light-induced degradation in a-Si [16], high temperature processing for CIGS and CdTe solar cells, inhomogeneity of chemical composition on large area substrates [16, 17] and indium and tellurium scarcity for mass scale production for both CdTe and CIGS solar cells [18].

Dye-sensitized solar cells (DSSCs) originated in the 1960s when Heinz Gerischer and coworkers discovered the sensitization of semiconductors [19]. Using a monolayer of a fluorescein dye on a thin ZnO semiconductor film, a microampere current was seen when the electrode was in contact with electrolyte solution under light illumination. A dye molecule attached to a semiconductor surface absorbs sunlight. The excited electrons are injected into the semiconductor. The electrolyte functions as a mediator to transport electrons to reduce dye molecules.

DSSCs consist of a dye coated TiO<sub>2</sub> semiconducting layer on FTO glass substrate (Photoanode) and a coating of few tens of nanometers thickness of platinum catalysts on FTO glass (Counter electrode). These two electrodes are sandwiched using a polymer spacer (60-100 micron thick) and ionic liquid electrolyte with I<sup>-</sup>/I<sub>3</sub><sup>-</sup> redox couples is used as a charge carrier in between the electrodes.

## **1.2 Previous work**

In 1839, the first photovoltaic effect was observed by Becquerel [20] when he noticed current flow through metal electrode in the electrolytic cell under light illumination.

In 1991, the first dye-sensitized solar cell was introduced by O'Regun and Gratzel with a PCE of 7.9 % [21]. The device consisted of photo-anode, electrolyte, and CE. The photoanode was comprised of ~ 10 microns ( $\mu\text{m}$ ) thick of mesoporous nanocrystalline titanium dioxide ( $\text{TiO}_2$ ) film deposited on transparent fluorine tin doped dioxide (FTO) substrate using doctor-blading. The photoanode was sensitized with trimeric ruthenium dye, which absorbs sunlight.

A PCE of ~ 10% was achieved in 1993 by Nazeeruddin [22]. The  $\text{TiO}_2$  film with a thickness of ~ 8 - 12  $\mu\text{m}$  was treated with  $\text{TiCl}_4$  and then sensitized with the  $\text{N}_3$  ruthenium dye. The advantage of  $\text{N}_2$  dye was to absorb light up to ~ 800nm compared to ~ 750 nm for the dye reported by O'Regun. Dye-sensitized photoanode was immersed in 4-*tert*-butylpyridine (TBP) solution. This treatment improved the charge transfer from dye molecules to  $\text{TiO}_2$  because TBP suppressed electron back recombination (dark current) at the  $\text{TiO}_2$ /electrolyte interface. This led to the enhancement of open circuit voltage ( $V_{OC}$ ) and fill factor ( $FF$ ). Barbe et al. explained that  $\text{TiCl}_4$  broadens the necking between  $\text{TiO}_2$  particles for enhanced electron percolation. Thus the short-circuit current ( $J_{SC}$ ) was increased [23].

In 2001, a black dye was introduced by Nazeeruddin et al. as a broad spectrum light absorbing and efficient sensitizers for DSSCs [24]. The new dye has an absorption range up to 920nm in the NIR region. Photocurrent generated for ~18  $\mu\text{m}$  thick photoanode with black dye was  $J_{SC} \sim 20 \text{ mA/cm}^2$  which was higher than the value obtained with  $\text{N}_3$  dye.

In 2005, Ito et al. employed a 4  $\mu\text{m}$  thick light scattering layer onto a  $\text{TiCl}_4$ -treated 14  $\mu\text{m}$  thick mesoporous  $\text{TiO}_2$  layer [25]. This multi-layered photoanode sensitized with  $\text{N719}$  dye produced ~ 10.6% efficiency with  $J_{SC} = 18.7 \text{ mA/cm}^2$ ,  $V_{OC} = 0.798 \text{ V}$  and  $FF =$

0.713. They also used FTO substrates coated with a thin layer of the compact TiO<sub>2</sub> layer. This thin under-layer compact TiO<sub>2</sub> reduced the recombination of photo-generated electrons with triiodide ions at the FTO/electrolyte interface.

In DSSC devices, the CE acts as a catalyst for the iodide/triiodide redox electrolyte regeneration and electron collector coming through the external circuit. The CE materials have been under intense investigation [17, 24, 26-33]. Due to its excellent catalytic activity, Pt has been using widely. However, Pt is expensive. To overcome this issue, many Pt-free and low-cost materials have been used as CE catalysts such as carbon materials and metal compounds.

### **1.2.1 Carbon nanomaterials**

Carbon nanomaterials are a good candidate as a catalyst because they are inexpensive, abundant, and corrosion resistant and have excellent catalytic activity towards redox electrolyte. The first use of carbon materials as a CE of DSSC was in 1996 by Kay and Gratzel [26]. They used a mixture of graphite and carbon black as a catalyst as well as a lateral current collector due to its high lateral conductivity. The device showed an overall PCE % of ~ 6.7%.

Carbon black (CB) was used as CE due to its high surface area-to-volume ratio, high conductivity and excellent electrocatalytic activity towards iodide/triiodide (I<sup>-</sup>/I<sub>3</sub><sup>-</sup>) electrolyte. Murakamiet et al. varied the thickness of CB CE [27]. It was noticed that the FF of the DSSC device increases with increasing the thickness of CB film; also charge transfer resistance of CE decreases. This observation was referred to that thicker CB film possesses high catalytic activity and conductivity and hence overall device performance.

In 2012, P. Srinivasu et al. used mesoporous carbon material as CE synthesized using the nano-casting technique [34]. Amongst all carbon based materials, mesoporous carbon has a great attention due to its high internal surface area, pore volume, tunable and narrow pore diameter. The large surface area helps in the penetration of electrolyte which resulted in giving an efficiency around 7.1% which was greater than that for activated carbon CE.

Graphene, which is one single atomic layer of graphite became a subject of extensive research after its discovery in 2004 [35]. Graphene has many advantages such as high carrier mobility ( $\sim 10,000 \text{ cm}^2/\text{Vs}$ ) [35-37], high specific area ( $2630 \text{ m}^2/\text{g}$ ) [38], excellent thermal conductivity ( $\sim 3000 \text{ W/Mk}$ ) [39], high Young's modulus ( $\sim 1 \text{ TPa}$ ) [40], and high optical transparency (97.7%) [41]. Due to its unique properties, graphene is considered as an excellent candidate to replace Pt as DSSC CE.

In 2011, Zhang et al. synthesized graphene nanosheets (GNs) by exfoliation of graphite followed by hydrazine reduction treatment [42]. The maximum obtained device efficiency was 6.8%. This synthesization method also showed that annealing temperature of GNs had a significant impact on overall device performance. The optimized temperature was found  $\sim 400 \text{ }^\circ\text{C}$  in which beyond this temperature, the film will peel off from the substrate due to the presence of an organic binder.

In 2011, Kavan et al. showed that the catalytic performance of GNs was affected by the defects and oxygen containing functionalized groups [43]. Also, he sported that The GNs synthesized from graphite by oxidation-reduction technique have lattice defects which could be considered as active catalytic sites for redox electrolyte. Mathew et al. discovered that the catalytic activity towards triiodide ions reduction could be increased by increasing

the number of functional groups with oxygen in a graphene sheet [44]. On the other hand, XU et al. showed that reduced graphene oxide (RGO) functionalized with –NHCO- group possessed higher catalytic activity than original RGO [45].

Carbon nanotubes (CNTs) captured more attention after the discovery in 1991 [46]. CNTs consist of concentric graphite cylinders at either end, and they align naturally into ropes and are held together by Van-der-Waals force. CNTs can be classified into three structures according to their number of rolled walls; single-walled carbon nanotubes (SWCNT), multi-walled (MWCNT) and double-walled (DWCNT). CNTs are catalytically active towards the redox ions of electrolyte in DSSC devices [47-51]. SWCNT and MWCNTs structures are used in DSSC as a CE because it has tunable surface areas and controllable defect edges that could facilitate the electron transport for better triiodide ( $I_3^-$ ) reduction process. MWCNT web was synthesized and used as a CE of DSSC by Nouredine et al. [52] and investigated its catalytic performance with different electrolytes. The device efficiency was ~ 4.2% for 20 layers of MWCNT web showing higher surface area and good electrocatalytic activity towards the electrolyte compared to Pt.

### 1.2.2 Polymers

Conductive polymers such as PEDOT-PSS, polypyrrole (PPy), polyaniline (PANI), etc. have been used in the Dye-sensitized solar cell as CEs because of its transparency and flexibility.

In 2003, Hayase et al. used PEDOT-PSS as a CE for quasi-solid DSSCs [18]. It was found that the performance of this polymer CE was better than Pt for ionic liquid electrolyte indicated by lower charge transfer resistance ( $R_{CT}$ ) at CE/electrolyte interface. However, for the organic liquid electrolyte, the result was opposite.



Yanagida et al. showed that the high viscosity and low conductivity of ionic liquid electrolyte led to a high concentration of  $I_2$ ; therefore, the porous PEDOT-PSS CE was better than Pt in the case of the ionic liquid electrolyte [17].

In 2009, Pringle et al. deposited PEDOT film on ITO/PEN flexible substrate using electrodeposition technique with different deposition times. He showed that 5 sec deposition time was enough to achieve high transparent and efficient PEDOT film. PCE value of  $\sim 8\%$  was produced using organic liquid electrolyte [16].

Ho et al. deposited PProDOT-Et<sub>2</sub> film on FTO substrate by the electropolymerization method [15]. The pore size of the PProDOT-Et<sub>2</sub> film was regulated by changing the charge capacities (10, 20, 40, 80, 120, 160, and 200 mC/ cm<sup>2</sup>). When the charge capacity reached 40 mC/ cm<sup>2</sup>, the PProDOT-Et<sub>2</sub> film owned the largest active surface area, generating the best catalytic ability. The DSSCs using this polymer CE yielded PCE value of 5.20%, close to that of the DSSCs using Pt CEs. They also compared the catalytic activities of PEDOT, PProDOT, and PProDOT-Et<sub>2</sub>. The DSSCs using PProDOT-Et<sub>2</sub> and PProDOT CEs showed PCE values of 7.88% and 7.08%, which were much higher than that of the DSSCs using PEDOT CE (3.93%).

Zhang et al. used polyethylene glycol (PEG) and acetylene black (AB) to modify PEDOT-PSS films as CEs for DSSCs [53]. The catalytic activity for triiodide reduction was improved by adding PEG, which acted as both conductivity promoting and binding agent. Catalytic activity was further improved by adding a little amount of AB. The DSSCs using a PEG/PEDOT/PSS/AB composite CE exhibited a PCE of 4.39%, slightly lower than the Pt CE based DSSCs (4.50%).

Xia et al. synthesized polypyrrole (PPy) film on FTO substrate using vapor-phase polymerization (VPP) and electropolymerization technique (EP) [54]. The PPy particle prepared by the VPP method exhibited a uniform size of 100-150 nm, while the PPy synthesized with an EP method had a larger particle size of 200-300 nm. The DSSCs using the PPy CEs gave PCE values of 3.4% VPP-PPy and 3.2% EP-PPy, both lower than that of the Pt CE based DSSCs (4.4%).

Im et al. synthesized a PPy spherical nanoparticle with a uniform size of 85 nm and used it as CE for DSSCs [55]. The conductivity was improved by treating the PPy with HCl. After optimization, the DSSCs using PPy CE showed PCE of 7.73%, as compared to the DSSCs using Pt CE (8.20%).

Transparent polyaniline (PANI) CE was fabricated by Zhao et al. via in situ polymerization method on FTO substrate [56]. The device showed a PCE value of 6.54% for the front side of illumination and PCE of 4.26% at rear-side illumination.

He et al. investigated the doping effect of  $\text{H}_2\text{SO}_4$  in the nanostructured PANI with different doping level and its impact on the catalytic activity of PANI CE [39]. It was found that the specific area of PANI CEs increase by increasing the concentration of  $\text{H}_2\text{SO}_4$  from 0.15 to 0.35 M which can improve the catalytic activity towards  $\text{I}^-/\text{I}_3^-$  redox reaction. The PCE of DSSCs using PANI CE was 5.57% which is close to that of DSSCs using Pt CE (~6%).

### **1.2.3 Metal compounds**

Since 2009, metal compounds have been applied in DSSCs as CE catalysts to replace the expensive Pt CE. The compounds contain carbides, nitrides, oxides, sulfides, oxides.

Lee et al. prepared tungsten carbide (WC) and used in DSSCs as the CE [57]. The device performance showed 6.61% PCE value with polymer derived method and ~ 7% PCE value for a micro-assisted method which still lower than that of DSSCs using Pt CE (8.23%).

Ma et al. introduced tungsten carbide (WC) and molybdenum carbide ( $\text{Mo}_2\text{C}$ ) as CE catalysts of DSSCs [58]. The device performance using these commercial materials as CEs showed PCE values of 5.35% and 5.7% respectively. However, these values were much lower than the corresponding PCE of the Pt CE base DSSC device (7.89%). They attributed the low device efficiency to the large particle size and little surface area of the two carbides. Later, the same group synthesized WC and  $\text{W}_2\text{C}$ , and the device performance was found to be 6.68% and 6.23% for  $\text{W}_2\text{C}$  and WC respectively. Compared to the large-sized WC particle the nanoscale WC showed much enhancement regarding its catalytic activity [59].

Other metal carbides such as TiC, VC, NbC,  $\text{Cr}_3\text{C}_2$ ,  $\text{Ta}_4\text{C}_3$ , and SiC have been introduced in iodide electrolyte based DSSCs as CEs [60-62]. Moreover, carbides CEs have been used for catalyzing the regeneration of the redox of  $\text{T}^+/\text{T}_2$ . The DSSCs using TiC, VC, and  $\text{Cr}_3\text{C}_2$  CEs produce PCE values of 4.96%, 4.06%, and 4.54% respectively.

Go et al. used TiN nanotube as a CE of DSSCs. The synthesis process was performed by the anodization of Ti foil, followed by simple nitridation [63]. The device performance showed PCE value of 7.73% which was higher than that of the Pt-based device (7.45%).

Cui et al. synthesized TiN sphere CE and it was found that the device performance was higher than that of TiN flat CEs due to the presence of the hierarchical structure of the

TiN spheres [64]. After optimization, the maximum PCE value reached 7.83%, which was 30% greater than that of Pt-based DSSCs.

Also, nanoparticles synthesis of TiN, VN, CrN, NbN and ZrN have been performed and used as CEs in DSSCs [60]. The PCE values were 6.23% (TiN), 5.92% (VN), 5.44% (CrN), 1.2% (NbN) and 3.68% (ZrN), respectively. Further, Mo<sub>2</sub>N and W<sub>2</sub>N prepared on Ti sheet by sputtering method have been used as CEs. The DSSCs performance using these two nitride CEs produces PCE values of 5.81% and 6.38% for Mo<sub>2</sub>N and W<sub>2</sub>N, respectively.

Gao et al. used the nitridation method for some metal oxides precursors (MoO<sub>2</sub>, WO<sub>3</sub>, Fe<sub>2</sub>O<sub>3</sub>) to produce MoN, WN, and Fe<sub>2</sub>N metal nitrides, respectively [65]. The corresponding DSSCs showed PCE values of 5.57%, 3.67% and 2.65% for MoN, WN, and Fe<sub>2</sub>N, respectively.

Gratzel et al. prepared semitransparent CoS film on ITO/PEN which was then introduced into DSSCs as a novel CE catalyst [66]. The Tafel polarization curves showed a significant slope for CoS CE, indicating a large  $J_0$  on the CoS electrode surface, comparable to Pt electrode. The DSSCs using CoS CE showed a PCE of 6.5%, equal to the Pt CE based DSSCs.

Tuan et al. reported the development of Co<sub>9</sub>S<sub>8</sub> nanocrystals as cost-effective CE catalyst for large-area DSSCs [67]. Single 2 cm sized DSSCs using Co<sub>9</sub>S<sub>8</sub> CEs showed an average PCE of 7.0%, slightly lower than Pt CE based DSSCs. While Ho et al. [68] used a CoS nanorod array as CE catalyst in DSSCs, producing a PCE of 7.67%, similar to Pt CE based DSSCs (7.7%). Also, Cu<sub>1.8</sub>S, Ni<sub>3</sub>S<sub>2</sub>, and Co<sub>8.4</sub>S<sub>4</sub> have been used by Batabyal et al. [69] as CEs in DSSCs and produced PCE values of 3.79%, 7.01%, and 6.5%, respectively.

Cen et al. fabricated and compared the DSSCs performance based on (130) and (211) facet of  $\text{Bi}_2\text{S}_3$  [70]. He concluded that (130) faceted  $\text{Bi}_2\text{S}_3$  has higher performance due to its high electronic conductivity, larger surface energy, and the position of conduction band minima which facilitate electron transfer from CEs to triiodide. Also, the same group [71] prepared a semitransparent film of  $\text{Fe}_2\text{S}_3$  on TTO/PEN substrate and used as a CE in DSSCs producing 7.31% PCE value. Further,  $\text{MoS}_2$  and  $\text{WS}_2$  were synthesized and used as CEs in DSSCs by Ma et al. [72]. The results showed that both metal sulfide performs very well regarding triiodide reduction. PCE values reports were 7.59 % and 7.73 % for  $\text{MoS}_2$  and  $\text{WS}_2$ , respectively which were comparable to the Pt-based device (7.64%).

Transition oxides metal oxides also have been used as catalysts in DSSCs due to its promising catalytic activity. Ma et al. used  $\text{WO}_2$  nanorods as the CE in DSSCs showing high catalytic activity towards iodide/triiodide electrolyte with PCE value as high as 7.25% close to 7.57% which produced by Pt-based DSSCs [73]. Similar to  $\text{WO}_3$ ,  $\text{WO}_{2.72}$  showed higher catalytic activity and overall performance with PCE value of 8.03 % which is very close to the Pt-based device (8.08%). The fundamental reason for this high performance of CE was not so clear and required more study [74].

Further,  $\text{V}_2\text{O}_5$ ,  $\text{ZrO}_2$ ,  $\text{TaOx}$ ,  $\text{TiO}_2$ ,  $\text{Nb}_2\text{O}_5$ ,  $\text{Cr}_2\text{O}_3$ ,  $\text{MoO}_2$  and  $\text{RuO}_2$  were introduced into DSSCs as CE catalysts. The device performance using  $\text{Nb}_2\text{O}_5$ ,  $\text{V}_2\text{O}_5$ , and  $\text{TaOx}$  showed decent PCE values of 4.84, 5.4 and 6.79% [60-62]. On the other hand,  $\text{TiO}_2$ ,  $\text{ZrO}_2$ ,  $\text{Cr}_2\text{O}_3$  and  $\text{MoO}_2$  showed poor catalytic activity for triiodide reduction. For  $\text{Nb}_2\text{O}_5$ , three different crystal structures of hexagonal (H- $\text{Nb}_2\text{O}_5$ ), orthorhombic (O- $\text{Nb}_2\text{O}_5$ ) and monoclinic (M- $\text{Nb}_2\text{O}_5$ ) were synthesized and investigate the impact of crystal structure on its catalytic activity [75].

It was found that the catalytic activity of transition metal oxides toward iodide-triiodide electrolyte could be enhanced significantly by annealing metal oxide under hydrogen ( $H_2$ ) or nitrogen ( $N_2$ ) gas atmosphere at a high temperature ( $\sim 470$ - $500$  °C) [76-79]. The idea is to introduce oxygen vacancies inside metal oxides by removing oxygen atoms in the form of  $NO_2$  gas or  $H_2O$  vapor. The oxygen vacancy was proved to facilitate the electron transport from CEs to iodide/triiodide electrolyte and hence make the reduction process of triiodide faster and hence improve the overall device performance.

Although catalytic activity of metal oxide was enhanced significantly by the annealing under  $N_2$  or  $H_2$  environment, the overall performance was still lower than that of the Pt-based device. Also, more analysis and characterizations should be done to investigate the impact of oxygen vacancies concentrations inside metal oxide to obtain the optimum conditions for higher device performance.

In 2015, Song et al. used ammonia ( $NH_3$ ) gas treatment to efficiently reduce  $WO_3$  films to use it as CE for DSSCs [80]. They found that treating  $WO_3$  films with  $NH_3$  is more efficient than  $N_2$  or  $H_2$  treatment reported before. The photovoltaic performance showed that device based on  $NH_3$ -treated  $WO_3$  CE is has a PCE value of 5.9% which was very comparable to that DSSC using standard Pt CE (with PCE of 6%). However, this method has a serious drawback using  $NH_3$  gas treatment which can cause health problems. Also, this technique is not a controllable process and cannot obtain conditions at which device performance produce its highest efficiency.

In this work, a novel method was created using urea pre-treatment of n-type commercial metal oxides such as  $WO_3$ ,  $SnO_2$  and  $ZnO$  prior annealing under  $N_2$  environment to control oxygen vacancies density in metal oxides for improved device

performance in a more controllable way by varying the amount of urea used in the treatment and obtain the optimum condition for the highest device performance. Compared to the previous work done by only annealing in  $N_2$  or  $H_2$  individually, the new proposed method is more efficient and finely controlled technique to maximize the performance of DSSC devices. This new treatment technique is also safer and more environmentally friendly than annealing under  $NH_3$  gas which could cause health problems.

### **1.3 Motivation**

There is a need for materials with high conductivity, high surface area, high abundance and low cost to replace the high expensive platinum as CE in DSSCs.

### **1.4 Objectives**

The objectives are to a) investigate urea treatment of n-type metal oxides ( $WO_3$ ,  $SnO_2$ , and  $ZnO$ ) as CEs in dye-sensitized solar cells, b) study the effect of increasing urea wt% on DSSCs performance and obtain the optimum conditions for the best overall device efficiency, c) obtain power conversion efficiency (PCE) higher than 9%. To achieve these objectives, the following tasks are established.

- 1) Fabricate urea pre-treated  $WO_3$ ,  $SnO_2$ , and  $ZnO$  CEs annealed under a nitrogen atmosphere at  $470\text{ }^\circ\text{C}$  for 2 hr with different urea doping wt%.
- 2) Characterize the surface morphology of all fabricated CE films using scanning electron microscopy (SEM) and Raman spectroscopy.

- 3) Fabricate DSSCs with three different metal oxides before and after urea pretreatment and perform current density-voltage (J-V) to calculate PCE values and compare them to the Pt-based device.
- 4) Perform electrochemical impedance spectroscopy (EIS), cyclic voltammetry (CV) and Mott-Schottky (MS) measurements for all fabricated CEs.



## Chapter 2: Theory

### 2.1 Solar cells and their operating principles

Solar cells absorb sunlight and convert it into electricity. Various types of solar cells (inorganic, organic, and hybrid) exist, all of which use common processes to generate electricity: light (photons) absorption, charge generation, transport of energized charge carriers and charge extraction from the device.

#### 2.1.1 Silicon Solar Cells

Silicon solar cells are based on the principle of P-N junction diode where P and N indicate for p-type and n-type semiconductors. N-type semiconductor is a silicon crystal that has been doped with a pentavalent element (valency of 5) such as phosphorus (P), Arsenic (As) or Antimony (Sb). Phosphorus has 5 valence electrons whereas silicon has 4. Thus, when a phosphorous atom bonds with four Si atoms, it has one electron left unbounded. At room temperature, these free electrons will often change places with nearby bound electrons. There is always a supply of free, mobile electrons available to carry current [60, 75]. The P-type semiconductor in which silicon crystal is doped with atoms of trivalent (valency of 3) element such as boron (B), aluminum (Al), gallium (Ga) or Indium (In). Boron has three valence electrons. Thus, when a boron atom shares its valence electrons with four neighboring Si atoms, one of the bond has missing electrons or called holes. At room temperature, these free holes will often change places with nearby bound electrons. These mobile holes are always available for conduction in the semiconductor. In the P-N silicon solar cell, the photons incident on the absorber leads to the formation of free electrons and holes which flow to the respective electrodes due to the presence of an internal

electric field. Fig 2.1 shows the solar energy received on earth per unit area versus wavelength. Crystalline silicon has a band gap of 1.1 eV corresponding to 1127 nm and therefore, Si can absorb all wavelengths lower than 1127 nm. The ideal band gap for photovoltaic conversion is 1.5 eV as it balances absorption loss and thermalization loss. GaAs has a bandgap of 1.42 eV and has optimum properties for photovoltaic applications. However, due to lattice mismatch between gallium and arsenic, it has to be grown by expensive molecular beam epitaxial methods to reduce lattice strain and hence is not cost effective regarding the large scale of photovoltaic applications. Silicon, on the other hand, is cheap and abundant and has fewer processing issues, hence is the most common material for photovoltaic applications.

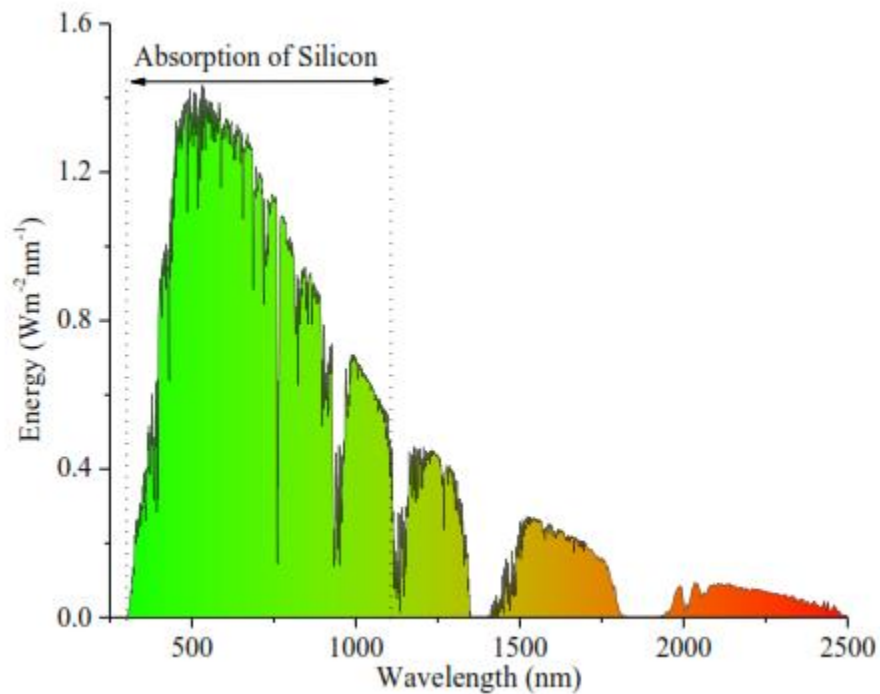


Figure 2.1 Solar irradiance spectrum [61].

Fig 2.2 shows the device structure of a typical passivated emitter, rear locally-diffused (PERL) single crystalline silicon solar cell [62]. The solar cell is constructed using a 400  $\mu\text{m}$  thick p-type silicon wafer [74]. The wafer is doped with boron to reduce the resistivity to 100  $\Omega\text{-cm}$  which acts as an absorber. Heavily doped  $\text{p}^+$  regions are formed by local diffusion of boron underneath the absorber layer followed by deposition of metal films as the rear contact. A thin n-type junction is formed on top of the absorber layer by a shallow phosphorus diffusion followed by heavy doping of phosphorous to form  $\text{n}^+$  layer. The top surface is etched to form an inverted pyramid structure to aid as an anti- reflection layer [73]. Finger-like metal contacts are deposited on top surface which forms the front contact. Silicon oxide interfaces are formed at  $\text{n}^+$  and  $\text{p}^+$  regions to suppress surface recombination [72].

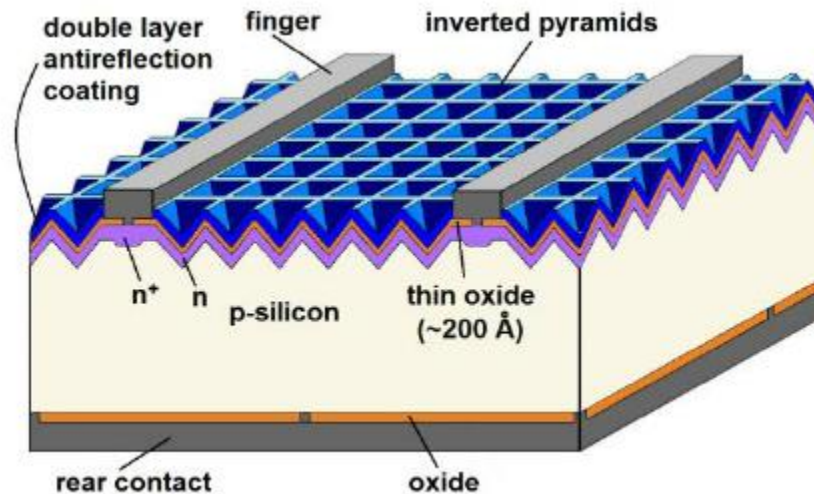


Figure 2.2 The device structure of passivated emitter, rear locally-diffused (PERL) single crystalline silicon solar cell [62].

The band diagram of a p-n junction solar cell is shown in Fig 2.3. The p-region has

a higher work function ( $E_{fp}$ ) compared to the vacuum level due to a higher concentration of holes, while the n-region has a lower work function ( $E_{fn}$ ) due to a higher concentration of electrons. When the two regions are not in contact, there is no band bending. However, when there exists a metallurgical junction between two, a depletion region is formed due to the difference in the charge carrier concentrations leading to band bending at the junction between p and n regions. The regions away from the junctions are known as a quasi-neutral region while the region in the vicinity of contact is called the space charge or depletion region. When photons are incident at the p or n-type region electrons from the valence band (VB) are excited to the conduction band (CB). Excitation of electrons to the conduction band leads to the formation of holes in the valence band. The electron-hole pairs are separated to free electrons and free holes at the junction due to the internal electric field. The internal electric field is caused by the potential difference between the two regions called the built-in potential ( $V_{bi}$ ). The free electrons flow through the n-side and free holes flow through p side and get collected at cathode and anode respectively.

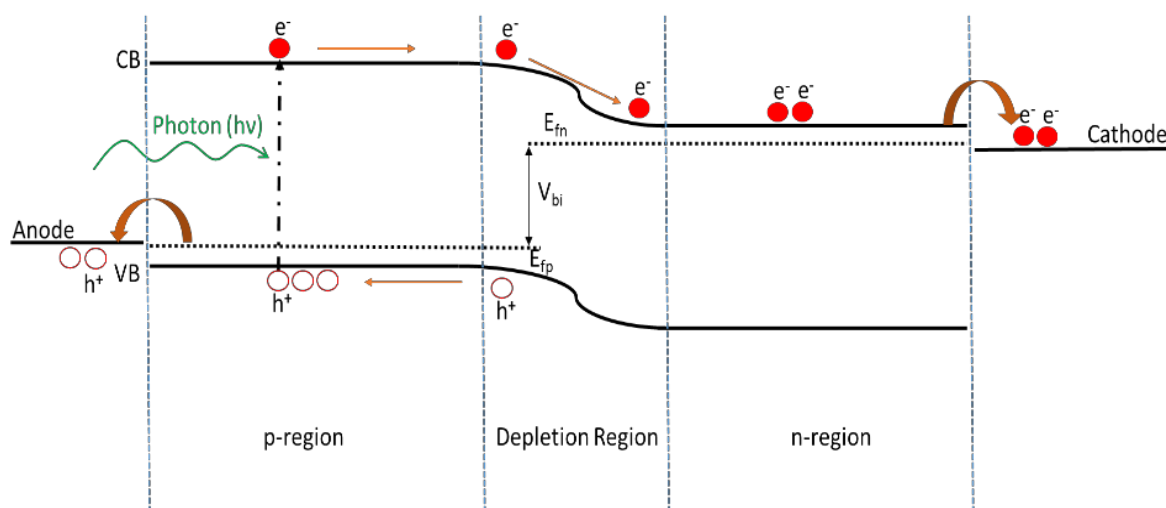


Figure 2.3 Band diagram of a p-n junction solar cell.

The depletion region or space charge region shown in Fig 2.3 is formed at the

junction of p and n-type layers due to diffusion of opposite charges across the junction caused by a concentration gradient. The width of the depletion region is calculated by knowing the doping concentration of p ( $N_A$ ) and n ( $N_D$ ) layers and under thermal equilibrium for a homojunction as:

$$W = \sqrt{\frac{2\epsilon V_{bi}}{q} \left( \frac{1}{N_A} + \frac{1}{N_D} \right)} \quad (2.1)$$

where  $\epsilon$  is the dielectric permittivity of the semiconductor,  $q$  is the elementary charge having a value of  $1.602 \times 10^{-19}$  C and  $V_{bi}$  is the built-in potential between the quasi-Fermi levels of p and n layers.

## 2.2 Operating principle of DSSC and charge transfer kinetics in DSSC

DSSC consists of two transparent FTO substrates (such as fluorine doped tin dioxide-glass substrates), one of which is a photoanode coated with mesoporous nanocrystalline  $ncTiO_2$  film and the other FTO is a CE coated with a thin film catalyst such as platinum and used as CE (Figure 2.4). A monolayer of dye molecules is chemically anchored onto the surface of the mesoporous- $TiO_2$ , and an electrolyte containing a redox couple ( $I/I_3^-$ ) is injected into the space between the photoelectrode and the CE. The excited dye molecule ( $S^*$ ) injects a photoelectron from the LUMO level into the conduction band of the  $TiO_2$ , and the dye molecule becomes oxidized ( $S^+$ ). The injected photoelectron travels through the mesoporous- $TiO_2$  film up to the transparent conducting side of the photoanode.

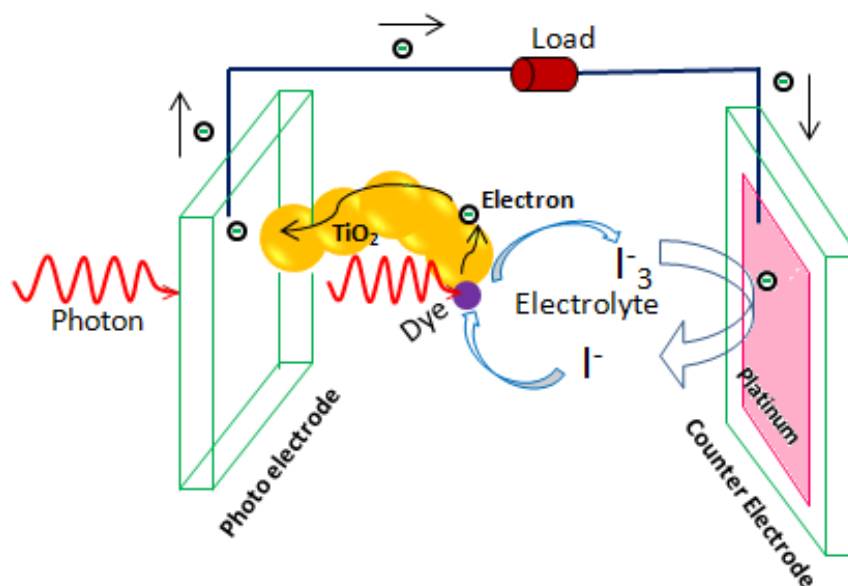


Figure 2.4. Schematic of a DSSC. Modified from ref [37]

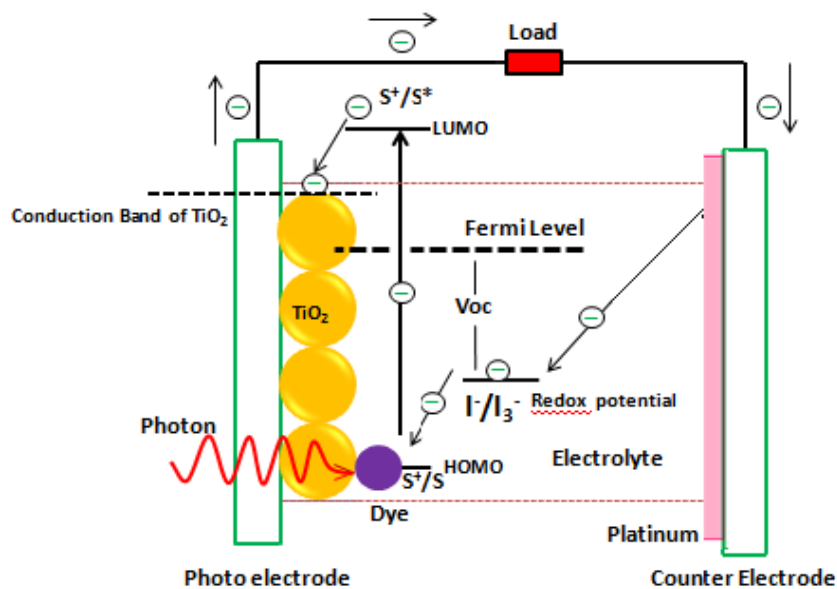


Figure 2.5 Schematic of DSSC with energy level diagram. Modified from ref [68, 69]. The dye is electronically excited after absorption of a light photon raising an electron from (HOMO) energy level of the dye to (LUMO) energy level.

After the electron travels along an external circuit containing a load and arrives at the CE, it combines with a tri-iodide to yield an iodide ion [81]:



The iodide (I) then diffuses in the electrolyte and arrives at the dye-sensitized porous TiO<sub>2</sub> film of the photoanode. The iodide gives an electron to the oxidized dye (S<sup>+</sup>) and turns into a tri-iodide [81]:



The photocurrent from DSSCs depends on several factors, including the HOMO and the LUMO energy levels of the dye molecule. During the photo-excitation of a dye molecule, the photoelectron is pumped from the HOMO to the LUMO by an incident light photon with energy greater than or equal to the energy difference between the two energy levels. Hence, a small value for the energy gap between the LUMO and the HOMO enables even low energy light photons in the solar spectrum to pump the electrons at the LUMO level of dye molecules and eventually increases the current from the device.

The current from the device is also influenced by the recombination mechanism that may take place in the device. To avoid recombination of an injected photoelectron with the oxidized dye, ultrafast injection of the photoelectron from the photo-excited dye molecule into the TiO<sub>2</sub> film and the subsequent regeneration of the oxidized dye by transferring an electron from the iodide (I) in the electrolyte are essential. Efficient sensitizers, in general, meet this criterion. For instance, the electron injection from an N<sub>3</sub> dye adsorbed on the TiO<sub>2</sub> surface of a nanoparticle takes place in the order of a femtoseconds and regeneration of the dye occurs in the order of nanoseconds, whereas the recombination of the injected electron (in the conduction band of the TiO<sub>2</sub>) with oxidized

dye requires a microsecond to a millisecond [65, 82]. Hence, such recombination can be practically negligible in DSSCs.

However, other recombination processes may take place in DSSCs. One of them is the recombination of the injected electron at the  $\text{TiO}_2$  surface to triiodide ( $\text{I}_3^-$ ) in the electrolyte. Another is the recombination of the photoelectron from the conducting surface of FTO substrate with the triiodide in the electrolyte. These two recombination processes can result in a dark current in the DSSC and decrease both current and PCE of the device [65].

### 2.3 Solar cell efficiency and processes that govern performance

The efficiency of solar cell is the measure of how well it can convert the light energy to electrical energy, called the overall power conversion efficiency,  $\eta$ ,

$$\eta = \frac{J_{SC} \times V_{OC} \times FF}{P_{IN}} \quad (2.4)$$

$J_{SC}$  is the short circuit current density,  $V_{OC}$  is the open circuit voltage, and  $FF$  is fill factor, and  $P_{IN}$  is the incident optical power density. Current-voltage  $J$ - $V$  curve is produced, which is seen in Figure 2.6, the efficiency parameters are labeled.  $J_{SC}$  is the maximum current that is able to flow through the cell under white light illumination, without an externally applied voltage.  $V_{OC}$  is the maximum voltage that must be applied to force the current to zero; it is a measure of the voltage the solar cell maintains when current is not allowed to pass through the cell. The product of  $J_{SC}$  and  $V_{OC}$  gives the larger area enclosed by the



dashed lines and the maximum power produced by the cell indicated by  $P_{MAX}$  is the smaller dashed area.  $FF$  is the ratio,

$$FF = \frac{P_{MAX}}{J_{SC} \times V_{OC}} \quad (2.5)$$

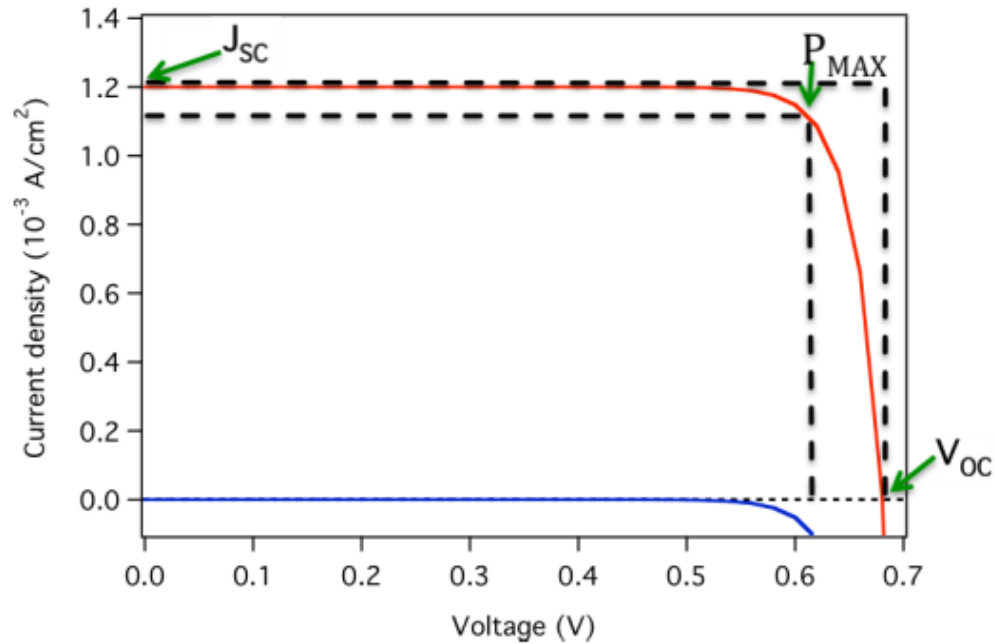


Figure 2.6 Plot of the J-V curves resulting from both (—) dark and (—) light current.

The efficiency parameters are also labeled in Figure 2.6. Dashed lines identify the area to calculate fill factor (FF). FF is a measure of the fullness or squareness of the  $J$ - $V$  curve. Resistive losses cause the curve to be rounded with a reduced  $P_{MAX}$ . Solar cells and their J-V curves are governed by the diode equation. After adapted to solar cell efficiency parameters, the diode equation is

$$J = J_{ph} - J_{dark} = J_{ph} - J_o \times \left( \exp \frac{qV}{nkT} - 1 \right) \quad (2.6)$$

Where  $J_{ph}$  is the photocurrent, which is diminished by opposing dark current,  $J_{dark}$ ,  $J_0$  is the interfacial exchange current,  $q$  is the electron charge,  $V$  is Voltage,  $n$  is the identity factor.  $k$  is Boltzman's constant, and  $T$  is temperature. At zero applied voltage, the  $J_{dark}$  is zero. As  $V$  increases from zero,  $J_{ph}$  remains constant but  $J_{dark}$  increases until  $J_{dark} = J_{ph}$  at  $V_{oc}$ ,

$$V_{OC} = \frac{nkT}{q} \ln\left(\frac{J_{SC}}{J_0} + 1\right) \quad (2.7)$$

Equation 2.4 is modeled using the equivalent circuit in figure 2.7. In this circuit,  $I_{ph}$  is represented by a current source;  $I_d$  is the diode dark current, ( $R_s$ ) is called as series resistance, ( $R_{sh}$ ) is parallel or shunt resistance connected to a load with resistance  $R_L$ .

Equation 2.6 could be rewritten as

$$I(V) = \frac{V - IR_s}{R_{sh}} + I_0 \left( e^{\frac{qV}{nkT}} - 1 \right) - I_{ph} \quad (2.8)$$

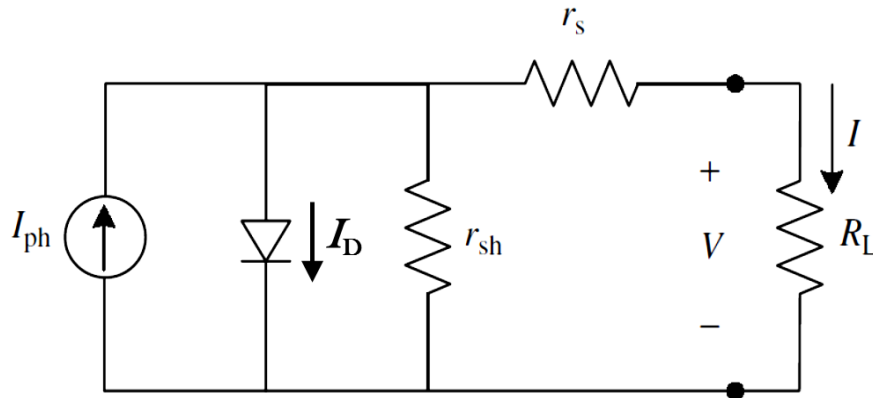


Figure 2.7 Equivalent circuit of solar cell [63].

Resistive losses are also discussed since they have effects on cell efficiency. Series resistance occurs along the path the current takes through the cell. Losses occur at the

contacts and the interfaces. Series resistance is exhibited as a reduction in fill factor by a ‘pulling in’ of the curve from the  $V_{OC}$  edge of the  $J$ - $V$  curve, seen in Figure 2.8. No other parameters are affected until this resistance is large enough to reduce  $J_{SC}$ . Shunt resistance is due to mishaps in cell fabrication. With module defects, current is able to flow via different routes and the photocurrent is reduced. Shunt resistance exhibited by ‘pulling down’ the current from the top of the curve, also seen in Figure 2.8, and when it is large enough it can cause a decrease in  $V_{OC}$ .

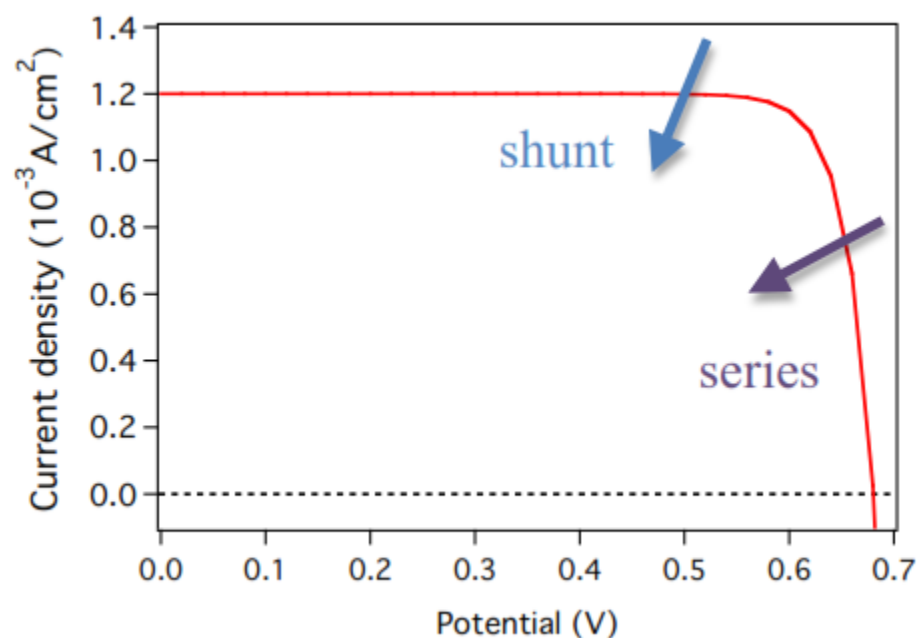


Figure 2.8 J-V curve with arrows showing the effects that series and shunt resistances have on the curve shape. The dashed line represents zero current density.

#### 2. 4 Kinetics of triiodide reduction reaction at CEs

Figure 2.9 shows a schematic of iodide/triiodide reaction at the CE interface. Triiodide ions, generated at the photoanode, diffuse to the CE and receive electrons at the

CE to reduce into iodide ions. This reaction occurring at the CE is represented by

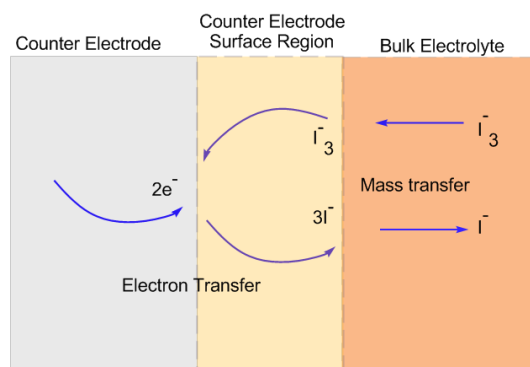


Figure 2.9 Schematic of electron transfer reaction at a CE.

The rate of electron transfer greatly depends on CE materials. For example, the electron transfer rate at bare FTO without any catalyst material is much slower compared with the electron transfer rate for platinized FTO-. A catalyst improves a reaction by reducing the required activation energy ( $E_a$ ). Therefore, the reaction or charge transfer at the CE/electrolyte interface in DSSCs is enhanced by a catalyst. In order to characterize the reaction at the CEs, the reaction is modeled with a resistance called charge transfer resistance ( $R_{CT}$ ). Under dark and open circuit conditions, a small value of  $R_{CT}$  implies a fast reaction whereas a large value of the  $R_{CT}$  indicating a sluggishness of the reaction at the CE/electrolyte interface [57].

## 2.5 Cyclic voltammetry

Cyclic voltammetry (CV) is an excellent technique used to get useful information about electrochemical reactions. In this technique, a cyclic potential sweep is applied to the CE immersed in the stable solution of redox couple electrolyte under study, and the current flow from the CE is monitored. Figure 2.10 shows a generic one electron transfer electrode reaction.

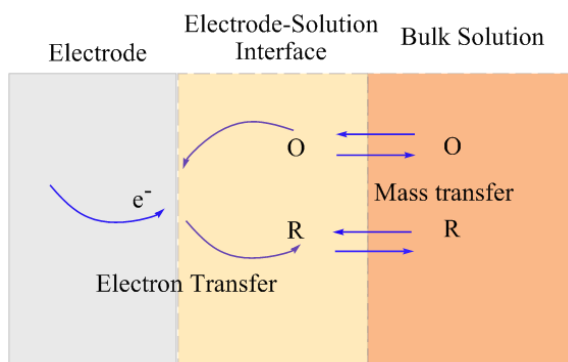


Figure 2.10 Schematic of the electrode reaction.

The reaction is represented by equation:



where  $O$  and  $R$  are oxidized and reduced species (redox couples) in a solution. Figure 2.14a shows a cyclic potential sweep and Figure 2.11b shows corresponding cyclic voltammetry curve. When the potential increases from an initial value ( $E_i$ ), as seen in Figure 2.11b, a small- transient non-faradaic current (a doubled layered capacitive current) appears. As the potential ramps up linearly with time beyond  $E_o$  (a threshold voltage), the Fermi-level of the electrode is raised above the energy level of vacant orbitals in the species,  $O$  (Figures 2.11 a & b). The electrons in the electrode cross the electrode-solution interface and reduce the species  $O$  into another species,  $R$  in the solution via reaction (2.9) and faradaic current flows in the electrode. A further increase in the negative potential accelerates the reduction of  $O$  species and causes the depletion of  $O$  species at the electrode/electrolyte interface. The depletion of the  $O$  species creates a huge concentration gradient of the  $O$  species between the electrode/electrolyte interface and the bulk solution. This concentration gradient enhances fast diffusion of  $O$  species from the bulk towards the interface, and the faradic current reaches a maximum or peak value called the cathodic

peak current ( $I_{pc}$ ) at the applied voltage,  $E_{pa}$ . Even though the applied voltage increases beyond  $E_{pa}$ , the cathodic current decreases continuously because the concentration gradient decreases as time proceeds.

As the potential reaches value of  $E_V$ , the direction of the potential ramp reverses and the potential proceeds towards the positive direction. When the potential approaches a value of  $E_0$ , the Fermi-level of the electrode is lowered, and electron transfer from  $R$  species into the electrode becomes more favorable, and  $R$  species are oxidized to  $O$  species via the reaction (Figure 2.12 c):

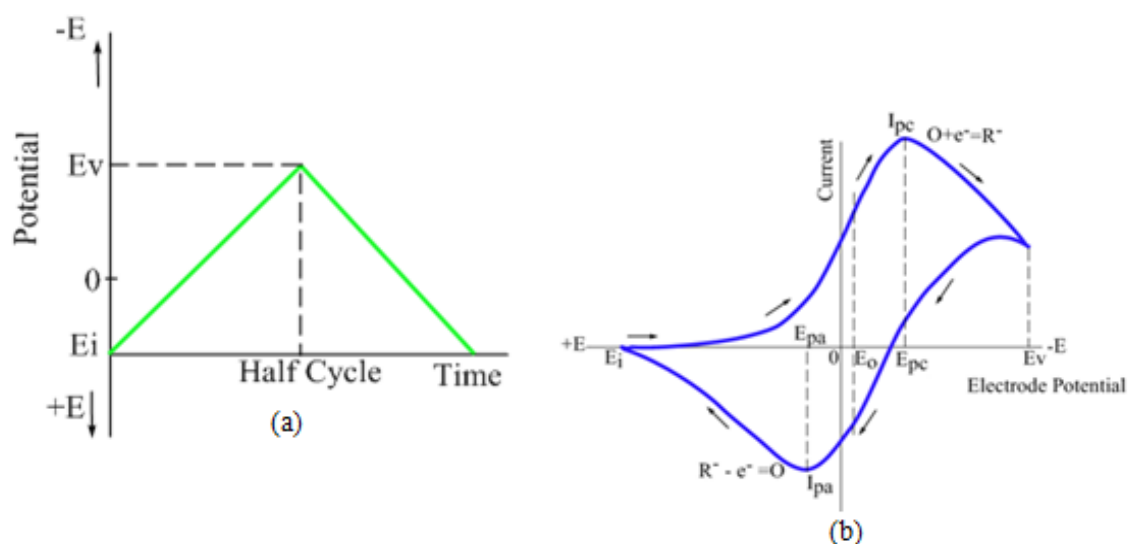


Figure 2.11 (a) Cyclic potential sweep and (b) cyclic voltammogram.

Figure 2.12 shows (a) energy level diagram of the electrode and species without application of the potential, (b) energy level diagram of the electrode and species after application of a negative potential (reduction process) and (c) energy level diagram of the electrode and species after application of positive potential (oxidation process). These diagrams were modified from ref. [57]. Faradaic current flows in the electrode, and another

peak current called the anodic peak current ( $I_{pa}$ ) appears as the positive potential increases to  $E_{pa}$  (Figure 2.16 b) [57].

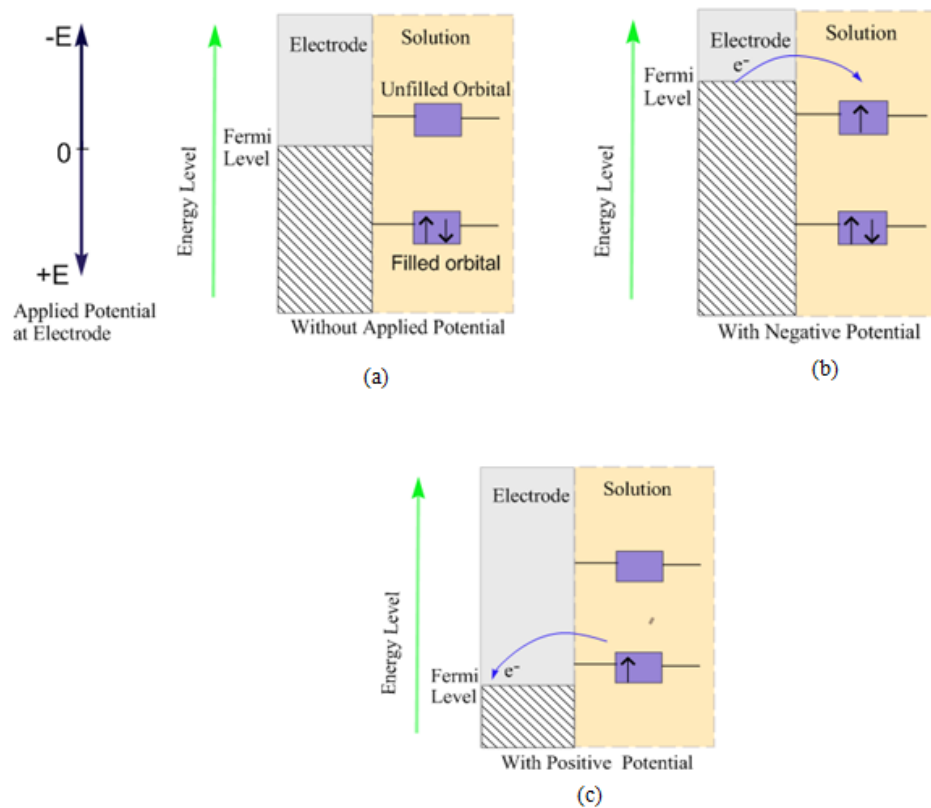


Figure 2.12 (a) Energy level diagram of the electrode and species without application of the potential. (b) Energy level diagram of the electrode and species after application of a negative potential (reduction process). (c) Energy level diagram of the electrode and species after application of positive potential (oxidation process). Modified from ref. [63].

## 2.6 Electrochemical impedance spectroscopy

Electrochemical impedance spectroscopy (*EIS*) is a useful technique to evaluate the catalytic property of CEs (CEs) for the reduction of triiodide ions [39, 83]. The catalytic property of CEs can be characterized by measuring the charge transfer resistance ( $R_{CT}$ ) at the electrolyte/CE interface. A smaller value of  $R_{CT}$  implies a fast reduction of triiodide

ions [39]. The  $R_{CT}$  is often determined by the electrochemical impedance spectroscopy (EIS) of symmetrical CE cells [39, 56]. Figure 2.13a and b show the Nyquist plot (impedance spectrum) of a symmetrical CE cell and the equivalent circuit used to fit the spectrum, respectively [39].

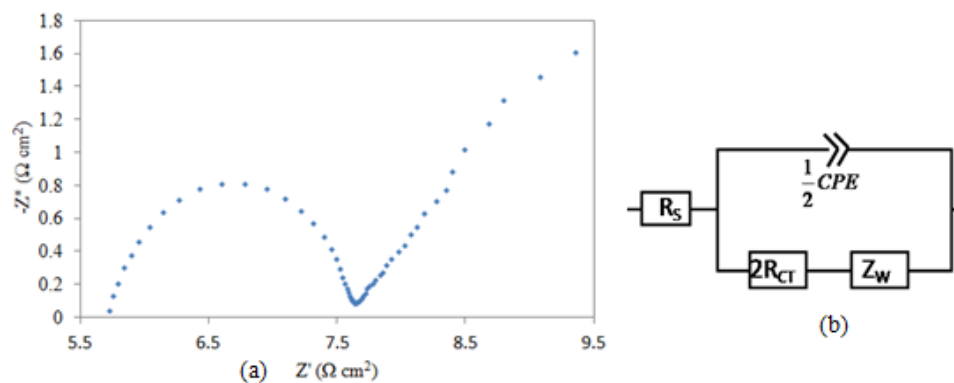


Figure 2.13 (a) Nyquist plot of a symmetrical cell and (b) an equivalent circuit of the symmetrical cell for the fitting of the Nyquist plot. Modified from ref. [39].

The equivalent circuit is comprised of charge transfer resistance ( $R_{CT}$ ) at the CE/electrolyte interface, series resistance ( $R_S$ ), constant phase element (CPE) or capacitance value for imperfect capacitors, and Warburg diffusion impedance ( $Z_W$ ). The high-frequency semicircle (the first semicircle from the left in the Figure 2.13a) results from the charge transfer process at the CE/electrolyte interface, while the low-frequency arc is due to the Nernst diffusion impedance ( $Z_W$ ) of the  $I/I_3^-$  redox couple in a thin layer of electrolyte [53-55]. The CPE represents the double layer capacitance at the interface between the CE and the electrolyte. The impedance of the CPE is expressed as [27, 39],

$$Z_{CPE} = \frac{1}{Y_0} (j\omega)^{-\beta} \quad (2.10)$$

where  $Y_0$  is the CPE parameter,  $\beta$  can be any value between 0 and 1. An ideal capacitance



has an exact semicircle with a  $\beta$  value of 1. However, several factors including surface roughness, porous films, a leaky capacitor, and non-uniform current distribution can lead to a non-ideal capacitance at the interface between the CE and the electrolyte, causing the semicircle to depress into an ellipse in the Nyquist plots [27, 39]. This depression typically causes the  $\beta$  value to decrease below 1. The  $R_s$  is the series resistance of the symmetrical cell.

## 2.7 UV-Vis absorption spectroscopy

UV-visible absorption spectroscopy is a good technique to measure the electronic transition within a material when exposed to light. The absorption of *UV* / visible light is related to outer electrons excitations. The material will absorb the light with a wavelength that matches the energy difference between the three possible electronic transition ( $\sigma$ -bonding,  $\pi$ -bonding, n-bonding to their higher anti-bonding molecular orbitals) within the molecule as shown in figure 2.14.

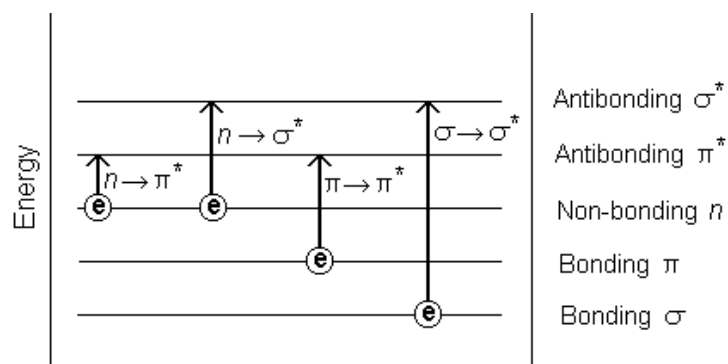


Figure 2.14 Possible electronic transitions of  $\pi$ ,  $\sigma$ , and  $n$  electrons [84].

The light absorption of material increases as the light beam attenuation increases inside the material. The absorbance is directly proportional to the path length  $b$ , solution

concentration  $c$  in case of liquid material. Beer's Law states that

$$A = \epsilon bc \quad (2.11)$$

Where  $\epsilon$  is the constant of proportionality and called the molar absorptivity.

Experimentally, according to Beer's Law, measurements are usually made in terms of transmittance ( $T$ ) which can be defined as:

$$T = \frac{I}{I_0} \quad (2.12)$$

Where  $I$  is the light intensity after crossing the absorbing material while  $I_0$  is the initial light intensity as shown in figure 2.15. The relation between absorbance ( $A$ ) and transmittance ( $T$ ) is given by,

$$A = -\log T = -\log \frac{I}{I_0} \quad (2.13)$$

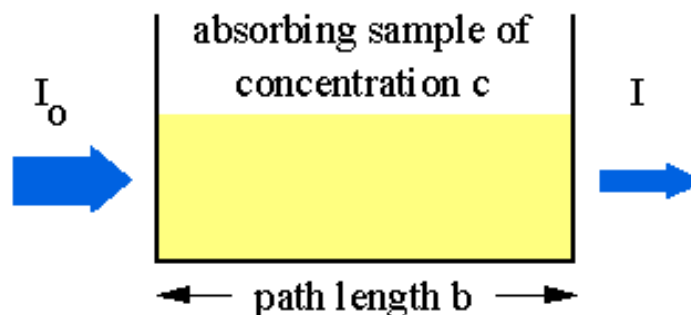


Figure 2.15 Absorption of light by a solution of absorbing material [70].

## 2.8 Mott-Schottky analysis

Mott-Schottky measurements could be a very helpful tool to calculate defect states density and Fermi-level position change upon electrochemical reaction for semiconductors or metal oxide materials when in contact with the electrolyte. As shown in figure 2.16,

before contact, fermi-level of metal oxide is in a different position than the redox potential of redox electrolyte.

When n-type metal oxide semiconductors in contact with the electrolyte, band bending at electrolyte/semiconductor interface will occur due to the energy difference in Fermi level positions for both metal oxide and electrolyte. Fermi level of n-type semiconductor, before soaked in electrolyte, is close to the conduction band and higher in position (lower in energy) than the Fermi level position of the electrolyte. After contact, band bending is upward shifted as shown in figure 2.16. Due to the formation of band bending, depletion region or space charge region will build up where no charges will be located in this region and will only be located outside the depletion region. Due to charge accumulation outside the depletion region, a capacitance will be build up called Mott-Schottky capacitance ( $C_{SC}$ ) and this capacitance will decrease with increasing band bending or depletion region at the electrolyte/metal oxide interface. To reduce band bending or depletion region, a negative potential is needed to be applied to metal oxide. Lower band bending requires lower negative potential to flatten the band bending.

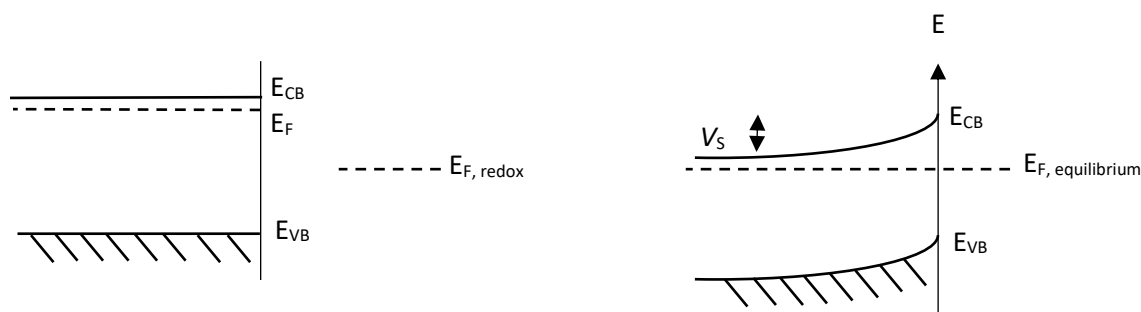


Figure 2.16 Band structure for iodide/triiodide ( $I^-/I_3^-$ ) and n-type metal oxide before and after contact.

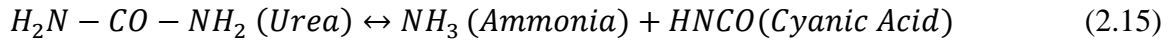
The relation which can control this change in band bending is called Mott-Schottky relation and described by equation 2.14.

$$\frac{1}{C_{SC}^2} = \frac{2}{\epsilon\epsilon_0 N_D} \left( V_A - V_{fb} - \frac{kT}{e} \right) \quad (2.14)$$

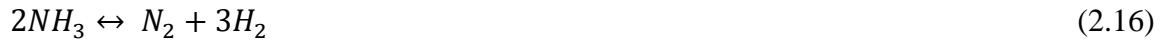
Where  $V_{fb}$  is the flat band potential, which is the potential needed to flatten the band bending at the CE/electrolyte interface,  $C_{sc}$  is the space charge capacitance,  $\epsilon$  is the dielectric constant of metal oxide,  $\epsilon_0$  is the permittivity of free space,  $N_D$  is the dopant density, and  $V_A$  is the applied potential vs. Ag/AgCl reference cell. According to the hypothesis that oxygen vacancies introduces shallow states close to both conduction and valence bands. As a result, new tail states will be formed and the conduction band (CB) will be downshifted while the valence band (VB) will be upshifted. Using Mott-Schottky measurements, flat band potential ( $V_{fb}$ ) could be calculated by plotting  $1/C_{sc}^2$  vs applied DC voltage from – ve voltage to + ve voltage. The flat band potential ( $V_{fb}$ ) value will give us an indication of fermi level position and how much the band bending occurs after contact with metal oxide with electrolyte. According to equation 2.14, the line intercept with potential axis will give the value of  $V_{fb}$  and hence how much the band bending produced after soaking the metal oxide in the electrolyte.

## 2.9. Mechanism of urea reaction with metal oxide at high temperatures

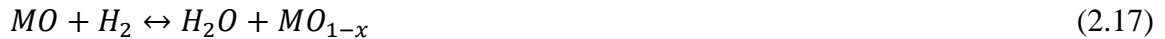
To explain why the number of pores and voids increases with increasing urea content, the reaction of urea with the metal oxide material at high-temperature annealing was discussed. Urea started to decompose into two main products, ammonia ( $\text{NH}_3$ ) and cyanic acid (HCNO) at 250 °C. It fully decomposed when the temperature reached ~300 °C according to reaction equation 2.15 reported previously [15-18].



By increasing the temperature to above 400 °C, ammonia (NH<sub>3</sub>) decomposes into Hydrogen (H<sub>2</sub>) and Nitrogen (N<sub>2</sub>) gases as seen reaction equation 4.2 [47, 52, 85]. Hydrogen gas (H<sub>2</sub>) is known as reducing agent [49, 50] for many metal oxides which could be used as gas sensors. At temperatures higher than 400 °C, oxygen atoms on the metal oxide surface gain the enough energy to leave and introduce oxygen vacancies. At the presence of H<sub>2</sub> gas, more oxygen atoms could be removed from the metal and oxidized the reducing H<sub>2</sub> gas into water vapor as shown in reaction equation 2.16 [48, 49, 86]. More reducing H<sub>2</sub> gas, more oxygen could be removed from the bulk of metal oxides in the form H<sub>2</sub>O vapor.



This explains why more pores appear with increasing urea content for pre-treated N<sub>2</sub>-annealed WO<sub>3</sub> films. Water vapor itself can easily react with cyanic acid at high temperature to produces



Where MO indicates for metal oxide. More ammonia (NH<sub>3</sub>) [15, 51, 87] around the films which again can decompose to hydrogen reducing gas (H<sub>2</sub>).



This helps to remove more oxygen from the film bulk in form of water vapor (H<sub>2</sub>O) and hence creates more oxygen vacancies. More pores and voids appear in the film. The number of pores in the metal oxide films will increase by increasing urea content for pretreated films. The reason is that the increased H<sub>2</sub> gas can penetrate more into the bulk film to remove more oxygen and oxidize itself into H<sub>2</sub>O vapor.

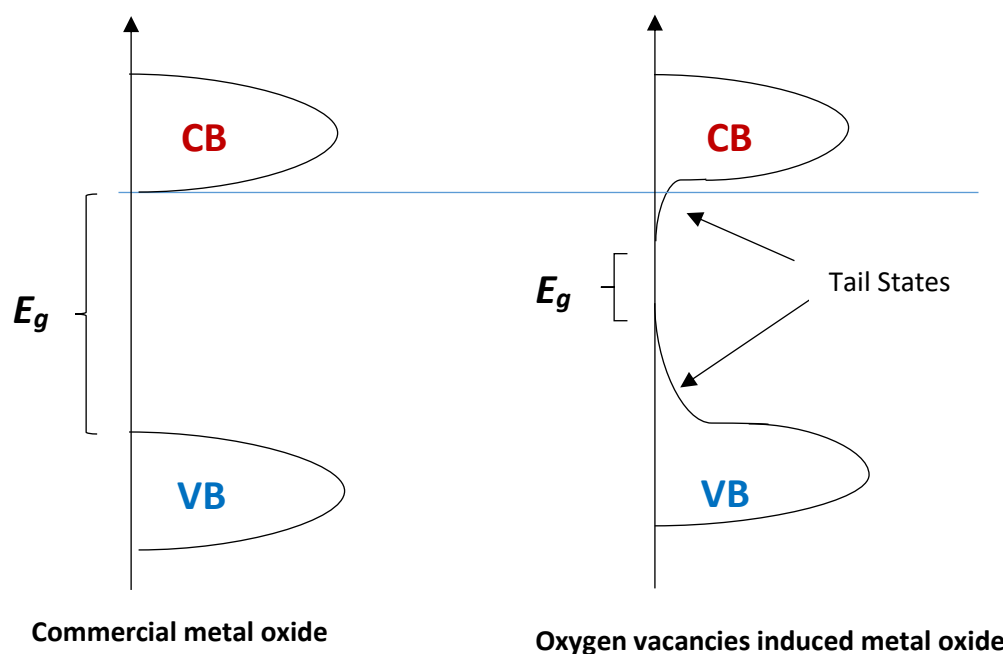


Figure 2.17 Diagram showing the effect of oxygen vacancies on metal oxide band gap.

## 2.10. Oxygen vacancy effect on the metal oxide band gap

The effect of oxygen vacancies or defects at the metal oxide surface has been studied to understand the electronic and chemical behaviors in photocatalysts and gas sensors. [1, 2, 7, 9, 10, 23, 28, 29, 32, 33, 88-92]. The introduction of oxygen vacancies has been done using different methods and techniques such as  $H_2$  treatment, chemical reduction, chemical oxidation, and anodization-annealing[13, 93, 94]. Oxygen vacancies will result in an excess of electrons produced in metal oxide therefore, the metal oxide will be more electron rich as an n-type semiconductor and the Fermi level will be negatively shifted closer to conduction band minima (CBM) level [14, 95]. Another effect of oxygen vacancies is the decrease of metal oxide band gap ( $E_g$ ). The band gap decrease was attributed to the introduction of energy band close to conduction band minima (CBM) and valance nad maxima (VBM). This new energy states will shift CBM level downward (positive shift)

and VBM level upward due to the extended tail states formation [14, 95] as shown in figure 2.17.

## Chapter 3: Experimental Procedures

### 3.1 Materials and device fabrication procedures

#### 3.1.1 Materials

All chemicals were used without further purification. Both  $\text{WO}_3$  (typically 99.9% pure, < 5 microns in average in particle size) and  $\text{SnO}_2$  (typically 99.9% pure, < 1 micron in average) were purchased from CERAC, Inc. (USA) while ZnO nanopowder was purchased from Sigma-Aldrich Corporation (St. Louis, MO). Fluorine-doped tin oxide (FTO) substrates were ordered from Hartford Glasses. Nanocrystalline  $\text{TiO}_2$  (Ti-Nanoxide HT/SP), scattering  $\text{TiO}_2$  (Ti-Nanooxide R/SP), N719 dye (Ruthenizer 535-bisTBA), and iodide/triiodide electrolyte (Iodolyte AN 50) were purchased from Solaronix. All materials were used as received except that  $\text{TiCl}_4$  was diluted in deionized water (DI) to prepare a 40 mM aqueous solution. All other materials were purchased from Sigma-Aldrich Corporation (St. Louis, MO).

#### 3.1.2 Counter electrode fabrication

The cleaning process is basic but very important to make high-efficiency DSSCs. FTO-glass (Harford Glass co. TEC-7, a sheet resistance of  $7 \Omega / \square$  and a thickness of 2.2 mm) was cleaned by sonication in detergent dissolved into deionized water (DI water), DI water, acetone and isopropyl alcohol (IPA) sequentially (15 min sonication each step). The purpose was to remove organic contaminants such as fingerprints which can be made during handling FTO-glass. Handling FTO-glass should be always done by plastic tweezers for preventing FTO-glass from contaminated by metals. Metal debris plays a role of strong recombination centers in DSSCs. Before using it, FTO-glass was completely dried by compressed nitrogen gas followed by UV- $\text{O}_3$  treatment for 20 min.



Five weight percentage concentrations (wt%) of urea treated  $\text{WO}_3$ ,  $\text{SnO}_2$ , and  $\text{ZnO}$  counter electrodes were prepared by mixing (0.1 gm each) powders of each metal oxide with 0.0033, 0.005, 0.01, 0.02, and 0.05 gm of urea individually to get ~ 3wt%, 5wt%, 9wt%, 16wt% and 33wt% of urea. Alpha-terpineol (100  $\mu\text{l}$ ) and 5 mg of ethyl cellulose as a binder were added to the urea/metal oxide mixture. The whole mixture was grinded in a mortar for 15 min. paste of the material was obtained. The paste was applied on a previously cleaned FTO substrate using doctor blading technique using 0.25  $\text{cm}^2$  mask then annealed under  $\text{N}_2$  environment at 470  $^\circ\text{C}$  for 2 hr in a tube furnace. The obtained counter electrodes were named as U3, U5, U9, U16 and U33 for urea concentrations of 3wt%, 5wt%, 9wt%, 16wt% and 33wt%, respectively. For comparison, two other metal oxide CEs were fabricated; the first is the pristine metal oxide, named as P- $\text{WO}_3$ , P- $\text{SnO}_2$ , and P- $\text{ZnO}$  CEs; the second is the  $\text{N}_2$ -annealed CE without any urea pre-treatment and denoted as N- $\text{WO}_3$ , N- $\text{SnO}_2$ , and N- $\text{ZnO}$ . Pristine  $\text{WO}_3$  and  $\text{SnO}_2$  CEs were prepared similarly but annealed in open air at 110  $^\circ\text{C}$  for 1 hr to remove any residual solvents. The reference Pt CE was fabricated by spin coating 20 mM of hydrogen hexachloroplatinate (IV) hexahydrate, 99.9% (trace metal basis), Acros Organics, in ethanol at 2000 rpm for 20 sec on top of FTO substrate, followed by annealing at 400  $^\circ\text{C}$  for 15 min. Figure 3.1 shows the different CEs fabricated from pristine films (P- $\text{WO}_3$ , P- $\text{SnO}_2$  and P- $\text{ZnO}$ ),  $\text{N}_2$ -annealed films (N- $\text{WO}_3$ , N- $\text{SnO}_2$  and N- $\text{ZnO}$ ) and urea pretreated  $\text{N}_2$ -annealed films with the different urea wt% (U3, U5, U9, U16, and U33).

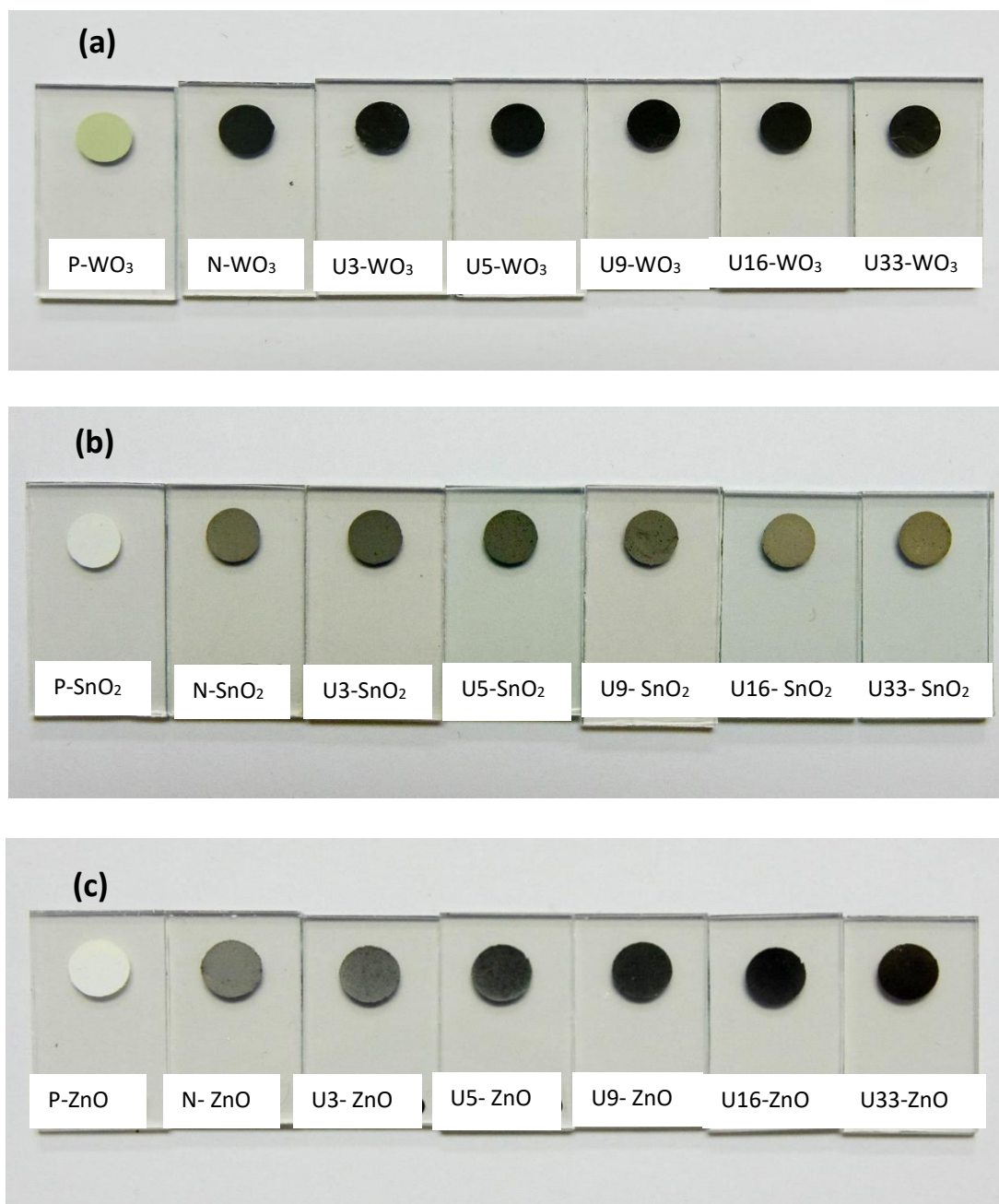


Figure 3.1 Different CEs fabricated from pristine films (P-WO<sub>3</sub>, P-SnO<sub>2</sub>, and P-ZnO), N<sub>2</sub>-annealed films (N-WO<sub>3</sub>, N-SnO<sub>2</sub>, and N-ZnO) and urea pretreated N<sub>2</sub>-annealed films with different wt% of urea-pretreated metal oxides (U3, U5, U9, U16, and U33).

### 3.1.3 Photoanode fabrication

To apply compact or blocking layer of TiO<sub>2</sub> layer, the cleaned FTO substrates were spin-coated with a 0.3 M of titanium di-isopropoxide bis (acetylacetonate) solution in anhydrous ethanol at a spin speed of 3,000 rpm for 20 sec in the ambient air. The spin coated films were pre-baked in ambient air for 30 min before sintered at 125 °C for 15 min then 475 °C for 30 min. A nanocrystalline mesoporous TiO<sub>2</sub> (Ti-Nanoxide HT/SP, Solaronix) film was doctor-bladed twice (the final thickness of two layers was ~ 12-13 μm) on top of the blocking layer using a mask of 3M Scotch tape with a circular opening of diameter ~ 4.5 mm (0.16 cm<sup>2</sup> area). Based on literature and experience, optimized total TiO<sub>2</sub> thickness exists between 12 μm and 18 μm. Although the great performance of DSSCs relies on a high surface area of mesoporous TiO<sub>2</sub>, thicker TiO<sub>2</sub> film also has a higher probability to recombine with a hole in the electrolyte and increases internal series resistance [1]. After each doctor-bladed layer, the film was left in air for about 10 min, and pre-baked at 125 °C for 15 min and 475 °C about 30 min. The reason of pre-baking is to minimize strain stress of TiO<sub>2</sub> film which can make cracks during annealing process and to protect fluidic TiO<sub>2</sub> paste film from dust or other debris during annealing. A light-scattering layer of TiO<sub>2</sub> (Ti-Nanoxide R/SP, Solaronix) was deposited onto the main layer (nanocrystalline TiO<sub>2</sub>) by doctor-blading, and then the film was sintered by the same way as previously described. The slow annealing and cooling down processes are very crucial to get crack-free TiO<sub>2</sub> film. The film was treated with a 40 mM aqueous solution of TiCl<sub>4</sub> and then sintered as described above. The purpose of this treatment is to increase roughness for enhancing dye-loading and improving the connectivity of TiO<sub>2</sub> particles. Finally, the film was cooled down to ~ 80 °C and then soaked in a 0.3 mM N-719 (Solaronix Ruthenizer

535-bisTBA) dye solution in acetonitrile / tert-butanol (1:1 by volume) for 24 hr. To avoid moisture on printed TiO<sub>2</sub>, it should be cooled down to 80 °C right before sensitizing. Moisture absorbed TiO<sub>2</sub> degrades dye molecules and desorbs dye molecules from TiO<sub>2</sub> under high temperature. Sensitization is performed under room temperature in the dark for 24 hr. Longer sensitization time can lead to dye-desorption depending on thermodynamic equilibrium relation. High temperature around 80 °C can accelerate dye absorption on TiO<sub>2</sub> to save time but evaporate solvents of the dye solution. After sensitization, extra dye-solution is washed out by anhydrous acetonitrile and then dried out by compressed nitrogen.

#### **3.1.4 Dye-sensitized solar cell device assembly**

Figure 3.2 shows the assembling of a DSSC. The dye-sensitized photo-anodes were washed with acetonitrile to remove unanchored dye from the TiO<sub>2</sub> film and then dried with compressed nitrogen gas. Both photo-anode and CE were then assembled using a thermoplastic sealant (Meltonix, Solaronix Co). The thermoplastic sealant was cut into a rectangular shape with the dimensions of about 2.5 cm × 1.5 cm. A circular hole of about 9 mm in diameter was made in the sealant using a puncher. Outside the hole, two narrow channels of about 1 mm width were made along the line of the diameter of the hole for the injection of the electrolyte. The sealant was kept on FTO surface in such a way metal oxide CE films were located at the center of the hole. The CE with the sealant was kept on a hot plate in such a way that the glass side of the CE was in contact with the hot plate.

The CE was heated at 80°C, and the sealant was gently pressed with a cotton tip so that the sealant stuck to the FTO without melting the sealant. Then the photo-anode was placed on at the sealant so that the dye-sensitized TiO<sub>2</sub> film was located directly over the hole on the sealant and above the circular CE film. The assembled layers of the photo-anode, the sealant, and the CE were heated on the hot plate from the glass side of the CE at ~110 °C for less than 2 min while pressed together from the glass side of the photo-anode. Once the sealant was melted with simultaneous application of heat and pressure, the cell was immediately removed from the hot plate and cooled down to room temperature. An electrolyte (Iodolyte AN-50) was injected into the cell through one of the channels made on the sealant using a plastic pipette. Once the space between the photoanode and the CE was filled with the electrolyte, the holes at the ends of the channels were sealed with hot glue (Adhesive Tech, melting point of 193 °C).

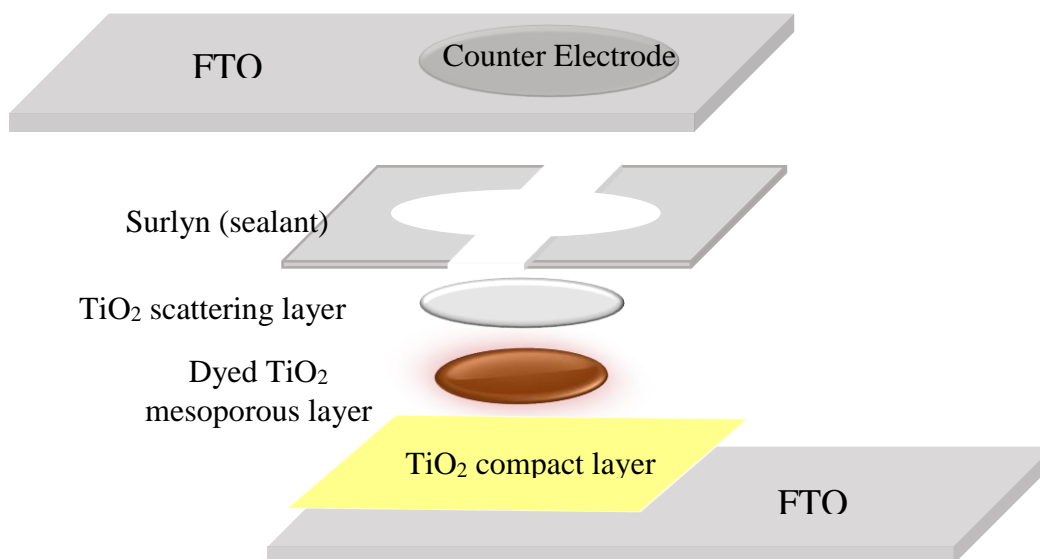


Figure 3.2 Schematic of DSSC device assembly.

## 3.2 Materials and device characterizations

### 3.2.1 Calculation of optical band gap value from UV-Visible absorbance spectra

The optical band gap for all metal oxide CEs has been evaluated from the absorption spectra in UV-Vis region using *Tauc's* relation [96]

$$\alpha h\nu = A(h\nu - E_g)^n \quad (3.1)$$

Where  $A$  is a constant,  $h\nu$  is the photon energy,  $E_g$  is the optical band gap,  $\alpha$  is the absorption coefficient and  $n$  is the exponent coefficient which denotes the nature of electron transition from valence to conduction band. The value of exponent coefficient ( $n$ ) depends on if the electronic transition from valence to conduction band either direct or indirect transition. For direct band gap transition materials,  $n$  takes value of  $1/2$  while in the case of indirect band gap transition materials,  $n$  takes value of 2. As shown in figure 3.3 an example of *Tauc* plot for TCO thin film which shows indirect band gap transition. The resulting plot has a linear regime which denotes the onset of the absorption. Thus, by extrapolating this linear region, optical band gap ( $E_g$ ) could be calculated from the intercept of the line extension with the x-axis (photon Energy  $h\nu$ ).

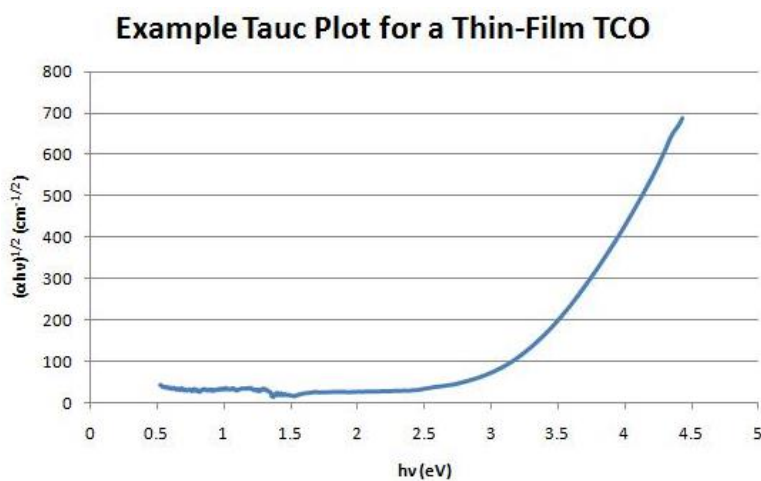


Figure 3.3 Example of a *Tauc* plot.

UV-Visible absorption measurements were conducted using Agilent 8853 spectrophotometer that had a mercury lamp for ultraviolet (UV) source and a tungsten lamp for visible and near infrared radiation shown in Figure 3.4.

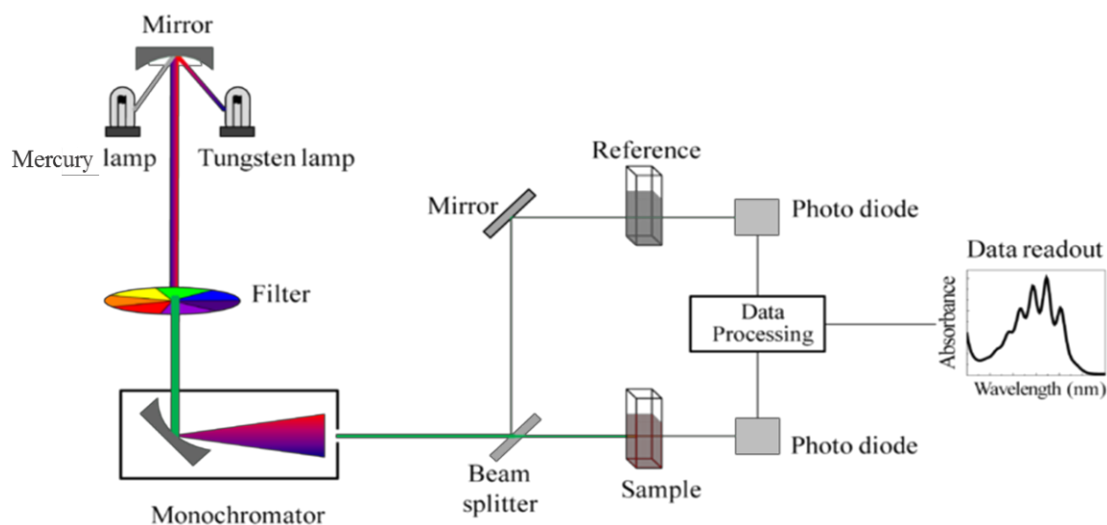


Figure 3.4 Schematic of UV-Visible absorption spectroscopy [97].

Light from the mercury and tungsten lamp was reflected from a mirror onto a filter. The filtered beam was passed through a monochromator grating to output monochromatic light. The monochromatic light was incident on the sample and compared with reference to output the sample absorption over different wavelengths. The absorbance of all fabricated metal oxide CE films was measured, and absorption coefficient ( $\alpha$ ) values were calculated using equation  $\alpha = 2.303 \frac{A}{d}$ , where  $A$  is the absorbance and  $d$  is the film thickness.

### 3.2.2 Raman Spectroscopy

Raman spectroscopy was performed using Horiba Scientific LabRam HR spectrophotometer for all fabricated metal oxide CE films and was excited with 784.32 nm laser. The laser intensity was attenuated using neutral density filters to avoid local burning

of the film. Raman spectra were collected from 200 to 900  $\text{cm}^{-1}$  and performed at several different areas on the sample to ensure the validity of data. The acquisition time was kept at 5 sec and averaged over two scans to reduce noise. 1800 grating spectrometer was used to attain higher resolution spectra.

### 3.2.3 Scanning electron microscopy

The morphology and element wt% measurements of all metal oxide CEs fabricated were examined using a Hitachi-S3400 N scanning electron microscope (SEM) with electron dispersive x-ray (EDX) at an applied bias of 5 KV.

### 3.2.4 Current-voltage (I-V) characterizations

Figure 3.5 shows the schematic of the experimental arrangement used to measure the  $J-V$  for DSSCs. The measurement was performed sweeping voltage from 0 to voltage and measuring the current under illumination. A Xenon lamp (Newport, Model 67005) with AM 1.5 filter was used as the illumination source. The power source to the solar simulator was set to 300 watts, and the lamp was turned on about 20 min before the calibration of the light intensity from the solar simulator. Agilent 4155C semiconductor parameter analyzer equipped with current and voltage source meters was used for voltage sweep from 0 V to 1 V with an increment of 10 mV. The current was simultaneously calculated at each step voltage. Prior to measurements, the light intensity was calibrated by optimizing the distance between the lamp and photodetector as shown in figure 3. 5.

This was done using NREL calibrated Hamamatsu photodetector (S1133). The distance was calibrated to attain short circuit current ( $I_{sc}$ ) of 753  $\mu\text{A}$ , and open circuit voltage ( $V_{oc}$ ) of 0.65 V. The incident illumination power density at this distance was 100



$\text{mW}/\text{cm}^2$ . The solar cells were kept at the same distance and position as the photodetector. AM 1.5 illumination was incident on the solar cells through the transparent FTO photoanode side. Agilent desktop expert software was used to communicate with the semiconductor parameter analyzer to perform the current-voltage sweep. Current-voltage readings were recorded under dark and illumination conditions. Solar cell parameters such as  $J_{sc}$ ,  $V_{oc}$ ,  $FF$ , and efficiency were calculated using the equations explained in section 2.3.

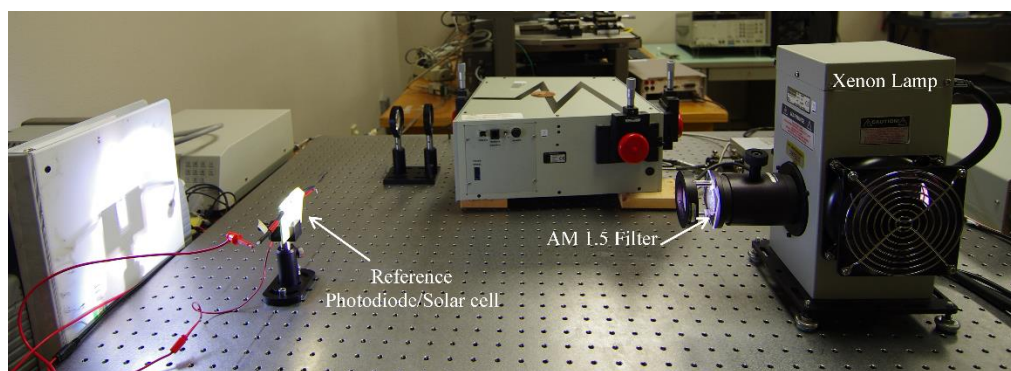


Figure 3.5 Photograph of the current-voltage measurement setup.

### 3.2.5 Electrochemical impedance spectroscopy

The catalytic properties of metal oxides CEs were compared with that with solution based reference Pt substrate with the techniques of electrochemical impedance spectroscopy (*EIS*), cyclic voltammetry (*CV*) and Mott-Schottky measurements. Figure 3.6 shows a schematic of a symmetrical electrochemical cell used for electrochemical impedance spectroscopy (*EIS*) measurement. The procedures for fabrication of symmetrical cells with the electrodes based on metal oxides films. Two similar metal oxide-film-coated FTOs were assembled following the similar procedures described in

section 3.1.2. The electrolyte of the same composition as that used in real DSSCs was injected into the symmetrical cell following the procedure as described in section 3.1.4. Similarly, symmetrical cells having platinum coated FTOs as two the electrodes enclosing the same electrolyte used in the previously described metal oxide-film-based symmetrical cells were fabricated.

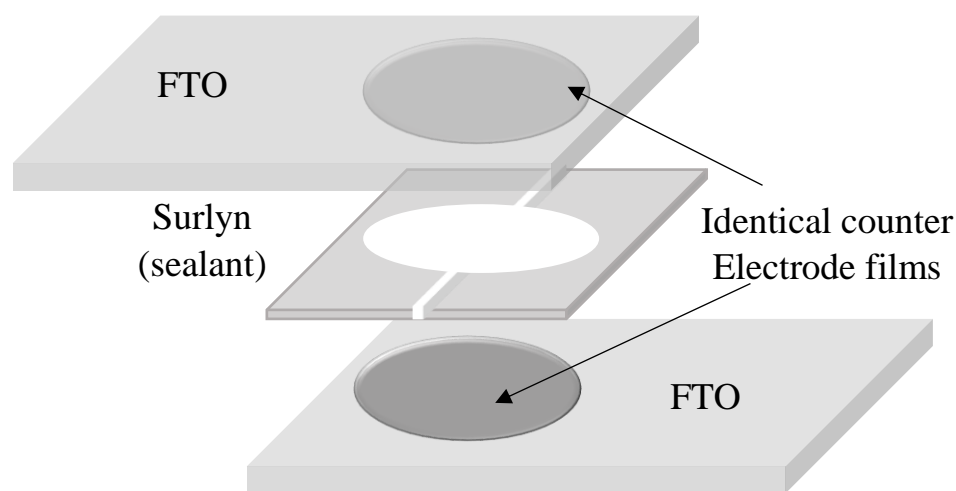


Figure 3.6 Schematic of a symmetrical electrochemical cell used for EIS measurement.

Figure 3.7 shows the functional diagram of an electrochemical impedance spectroscopy (EIS) experiment run to evaluate the catalytic property of ECNs and platinum using symmetrical cells. Ametek VERSASTAT3-200 Potentiostat with a frequency analysis module (FDA) was used for the EIS measurement. The EIS was carried out for symmetrical cells as follows. First, the reference probe and the CE probe from Ametek VERSASTAT3-200 Potentiostat with frequency analysis module (FDA) were connected together at one electrode of the symmetrical cell, and the working electrode and the sensor

probes of the Ametek VERSASTAT3-200 Potentiostat were connected together to the other electrode of the symmetrical cell. The Nyquist plots were obtained at a zero bias voltage with 10 mV AC signal having a frequency sweep from 10 Hz to 100 KHz.

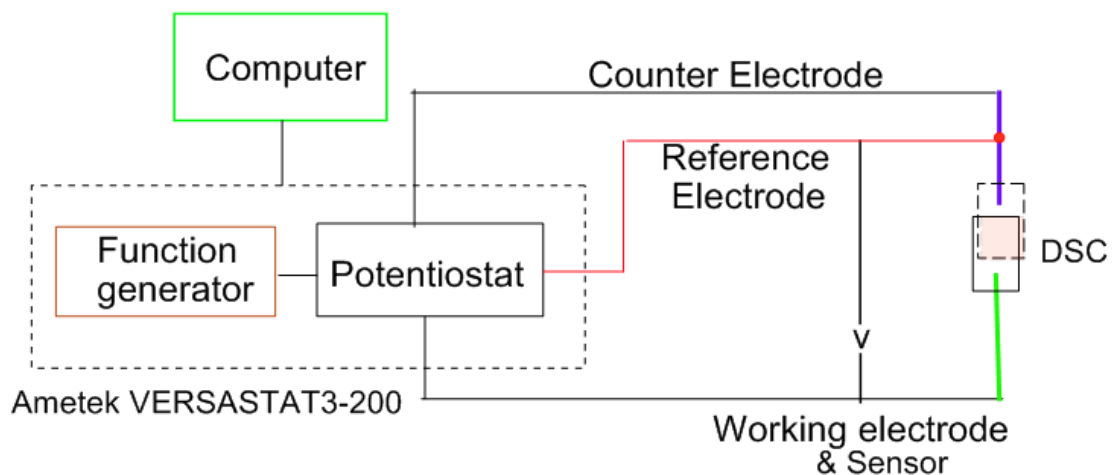


Figure 3.7 The functional diagram of an EIS experiment.

### 3.2.6 Cyclic voltammetry and Mott-Schottky measurements

Figure 3.8 shows a functional diagram of a cyclic voltammetry (CV) and Mott-Schottky experimental setup used to evaluate the catalytic property of the different metal oxides and platinum counter electrodes. The cyclic voltammetry was carried out in a solution of acetonitrile as a solvent and 10 mM lithium iodide (LiI) and 0.5mM of iodide (I<sub>2</sub>) as solutes with 0.1mM, tetrabutylammonium hexafluorophosphate, (CH<sub>3</sub>CH<sub>2</sub>CH<sub>2</sub>CH<sub>2</sub>)<sub>4</sub>N(PF<sub>6</sub>), or 0.1M tetra-n-butylammonium tetrafluoroborate as a supporting electrolyte. The metal oxide CEs, Ag/AgCl, and a platinum wire were used as the working electrode, the reference electrode, and the CE, respectively [81]. The cyclic potential sweep with an initial potential of -0.5 V, a maximum potential (or vertex potential) of 1.5 V, and a scan rate of 0.05Vs<sup>-1</sup> was applied at the working electrode. Mott-

Scottkey measurement was conducted with the same experimental setup and as CV characterization. The difference was that AC signal of 20 mV amplitude and fixed frequency of 100 Hz was applied while the DC voltage bias was swept from -1 V to 1 V with an increment of 0.05 V.

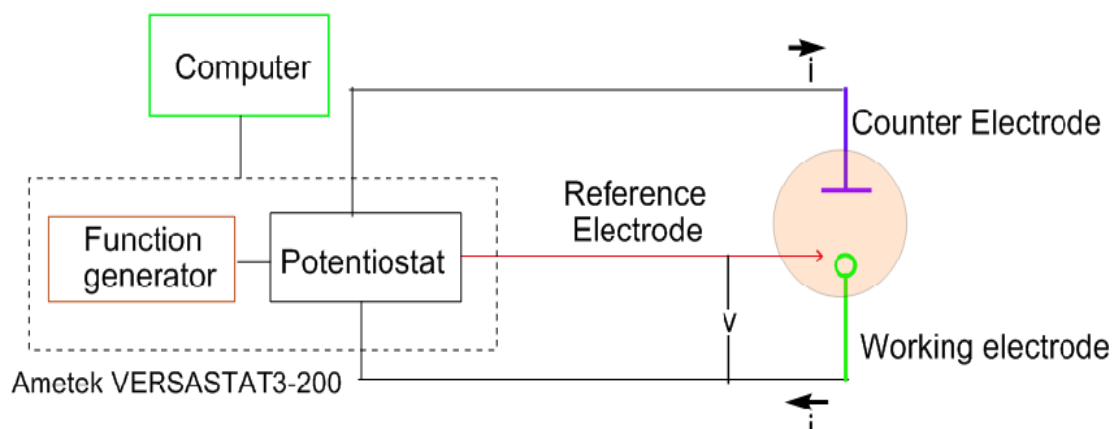


Figure 3.8 Functional diagram of cyclic voltammetry (CV).

## Chapter 4: Results and analysis

### 4.1 Scanning electron microscopy (SEM) and energy dispersive X-ray spectroscopy (EDS)

#### 4.1.1 SEM and EDS for WO<sub>3</sub> CE films before and after urea-pretreatment

The surface morphology of fabricated WO<sub>3</sub> CE films before and after urea-pretreatment with different urea wt% was performed and characterized by SEM and shown in figure 4.1. The surface morphology of pristine WO<sub>3</sub> CE (P-WO<sub>3</sub>) was found to be compact with little and tiny pores and cracks which considered as a disadvantage of preventing more electrolyte solution to get penetrated inside the CE and the overall triiodide ions reduction will be slow and inefficient and hence the overall catalytic activity of CE. The surface morphology of N<sub>2</sub>-annealed WO<sub>3</sub> films in N<sub>2</sub> environment (N-WO<sub>3</sub>) without urea pre-treatment was found to be very similar to pristine (P-WO<sub>3</sub>) without significant change in film compactness with a little number of pores. On the other hand, when 0.3 wt% of urea was used for WO<sub>3</sub> pretreatment prior annealing in N<sub>2</sub> atmosphere (U3-WO<sub>3</sub> CE), pores and cracks were introduced in the film. The number of pores and voids increased when urea wt% increase to 5wt% for U5-WO<sub>3</sub> CE. The number of pores was further increased linearly by increasing the wt% of urea to 9wt% for U9-WO<sub>3</sub> CE, 16wt% for U16-WO<sub>3</sub> and 33wt% for U33-WO<sub>3</sub> CE. The increase in pores and cracks linearly with increasing the urea wt% is due to the increase in the reducing H<sub>2</sub> gas produced as a result of urea decomposition. More H<sub>2</sub> gas produced by increasing urea wt% will lead to extract more oxygen atoms from metal oxide film in form of H<sub>2</sub>O vapor evolution which leave more pores and cracks in metal oxide films.

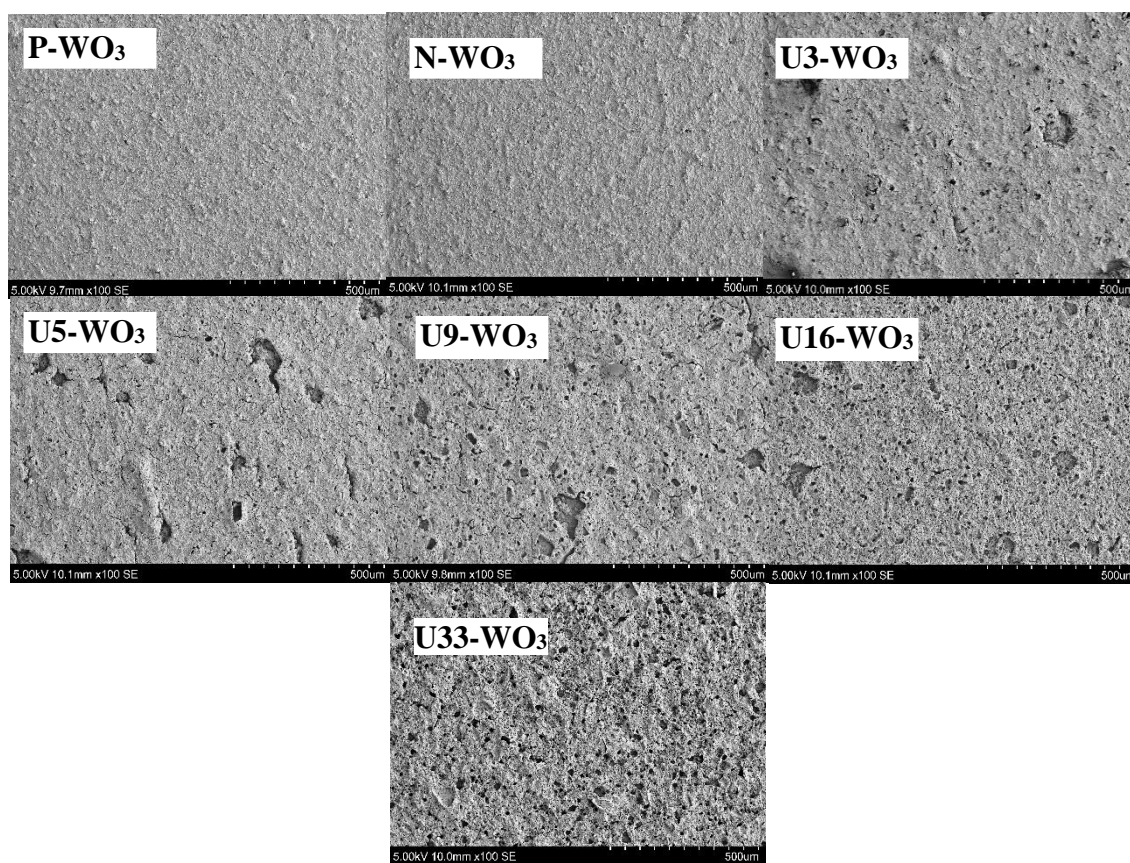


Figure 4.1. SEM images for pristine  $\text{WO}_3$  (P- $\text{WO}_3$ ),  $\text{N}_2$ -annealed  $\text{WO}_3$  (N- $\text{WO}_3$ ) and urea pre-treated  $\text{N}_2$ -annealed  $\text{WO}_3$  with different urea wt% (U3- $\text{WO}_3$ , U5- $\text{WO}_3$ , U9- $\text{WO}_3$ , U16- $\text{WO}_3$ , and U33- $\text{WO}_3$ ).

Energy dispersive X-ray spectroscopy was performed for all  $\text{WO}_3$  CE films before and after applying urea with the different urea wt%. This measurement was conducted to calculate the oxygen wt% inside the films by increasing the urea content for the pre-treated films. Figure 4.2 shows the plot of oxygen wt% and the different type of metal oxide CE from the plot. It was found that the oxygen wt% for pristine (P- $\text{WO}_3$ ) metal oxide is the highest with a value of  $\sim 4.9\%$  after annealing in  $\text{N}_2$  atmosphere. The oxygen wt% in N- $\text{WO}_3$  CE film decreased to  $\sim 4.4\%$  which indicates that oxygen vacancies were introduced after annealing. The oxygen wt% value decreased with increasing urea content for pre-

treatment. Oxygen wt% has the values of 4.2%, 3.7%, 3.3%, 3% and 2.6% for U3-WO<sub>3</sub>, U5-WO<sub>3</sub>, U9-WO<sub>3</sub>, U16-WO<sub>3</sub> and U33-WO<sub>3</sub> CEs respectively. The decrease in Oxygen wt% by increasing urea wt% is a direct support for the hypothesis that higher urea content leads to losing of more oxygen for pre-treated WO<sub>3</sub> metal oxide films.

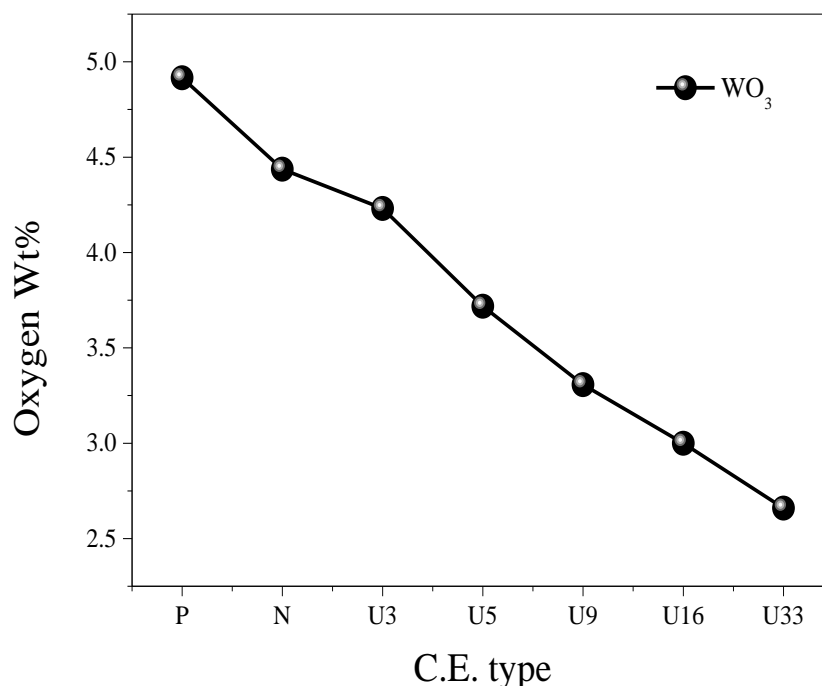


Figure 4.2. Oxygen Wt% for WO<sub>3</sub> film before and after urea pre-treatment with different urea wt%.

#### 4.1.2 SEM and EDS for SnO<sub>2</sub> CE films before and after urea-pretreatment

The surface morphology of fabricated SnO<sub>2</sub> CE films before and after urea-pretreatment with different urea wt% was performed and characterized by SEM, as shown in figure 4.3. The surface morphology of pristine SnO<sub>2</sub> CE (P-SnO<sub>2</sub>) was found to be compact with little, tiny pores and cracks. This led to a disadvantage that less electrolyte solution penetrates inside the CE. The overall triiodide ions reduction will be slow and inefficient and hence the overall catalytic activity of CE is low.

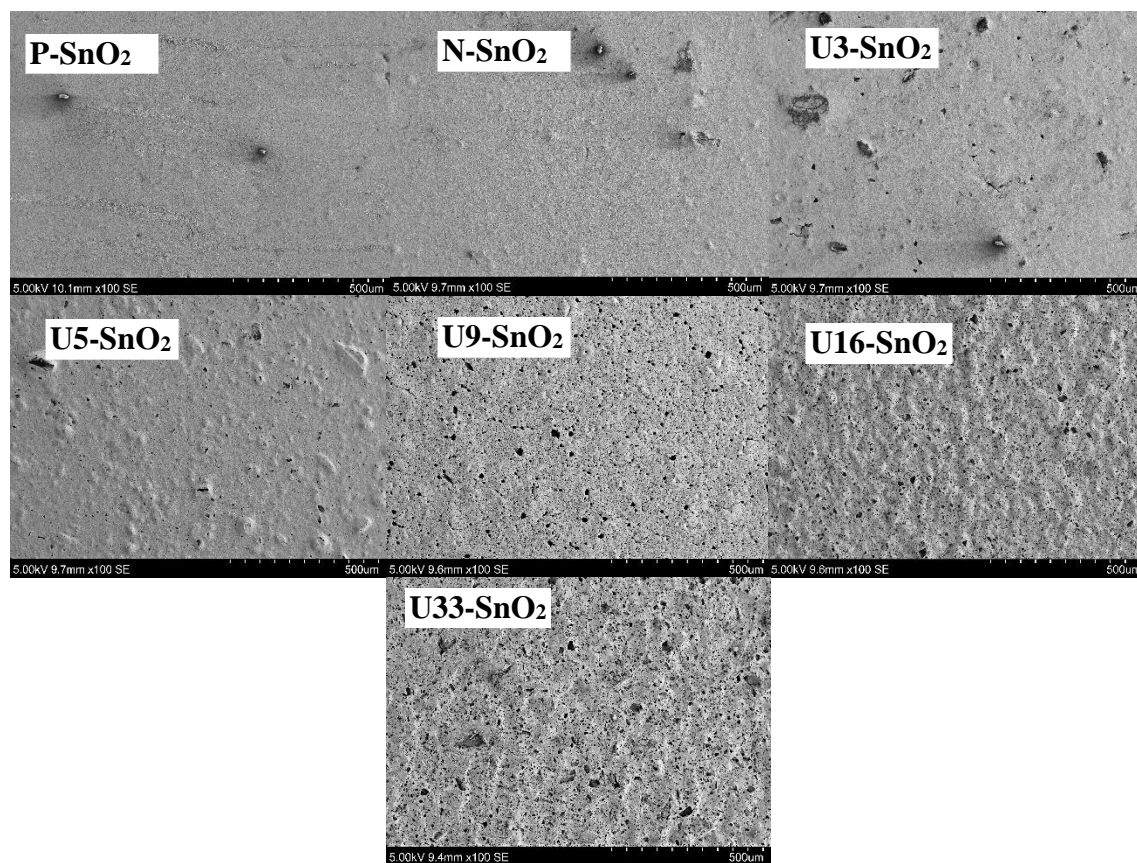


Figure 4.3. SEM images for pristine  $\text{SnO}_2$  (P- $\text{SnO}_2$ ),  $\text{N}_2$ -annealed  $\text{SnO}_2$  (N- $\text{SnO}_2$ ) and urea pre-treated  $\text{N}_2$ -annealed  $\text{SnO}_2$  with different urea wt% (U3-  $\text{SnO}_2$ , U5- $\text{SnO}_2$ , U9- $\text{SnO}_2$ , U16- $\text{SnO}_2$ , and U33- $\text{SnO}_2$ ).

The surface morphology of  $\text{N}_2$ -annealed  $\text{SnO}_2$  films in  $\text{N}_2$  environment (N- $\text{SnO}_2$ ) without urea pre-treatment was found to be very similar to pristine (P- $\text{SnO}_2$ ) without significant change in film compactness with a little number of pores. On the other hand, when 3wt. % of urea was used for  $\text{SnO}_2$  pretreatment prior to annealing in  $\text{N}_2$  atmosphere (U3- $\text{SnO}_2$  CE), pores and cracks were introduced in the film. The number of pores and voids increased when urea wt% increase to 5wt% for U5- $\text{SnO}_2$  CE. The number of pores was further increased linearly by increasing the wt% of urea to 9wt% for U9-  $\text{SnO}_2$  CE,



16wt% for U16-SnO<sub>2</sub> and 33wt% for U33-SnO<sub>2</sub> CE. The increase in films pores and cracks linearly with increasing the urea wt% is due to the increase in the reducing H<sub>2</sub> gas produced as a result of urea decomposition. More H<sub>2</sub> gas evolution will lead to extract more oxygen atoms from metal oxide film in form H<sub>2</sub>O vapor evolution which leave more pores and cracks in metal oxide films.

Energy dispersive X-ray spectroscopy was performed for all SnO<sub>2</sub> CE films before and after applying urea with the different urea wt%. This measurement was conducted to calculate the oxygen wt% inside the films by increasing the urea content for the pre-treated films. Figure 4.4 shows the plot of Oxygen wt% and the different type of metal oxide CE. It was found that the oxygen wt% for pristine (P-SnO<sub>2</sub>) metal oxide is the highest with a value of ~ 4.7% after annealing in N<sub>2</sub> atmosphere, the oxygen wt% in N-SnO<sub>2</sub> C film was decreased to ~ 4.5% which indicates that oxygen vacancies were introduced after annealing. The oxygen wt% value decreased early with increasing urea content for pretreatment. Oxygen wt% has the values of ~3.8%, ~ 3.4%, ~ 3.2%, ~ 3% and ~ 2.5% for U3-SnO<sub>2</sub>, U5-SnO<sub>2</sub>, U9-SnO<sub>2</sub>, U16- SnO<sub>2</sub> and U33-SnO<sub>2</sub> CEs, respectively. The decrease in oxygen wt% by increasing urea wt% is direct support for the proposed hypothesis that higher urea content leads to losing of more oxygen for pre-treated SnO<sub>2</sub> metal oxide film.

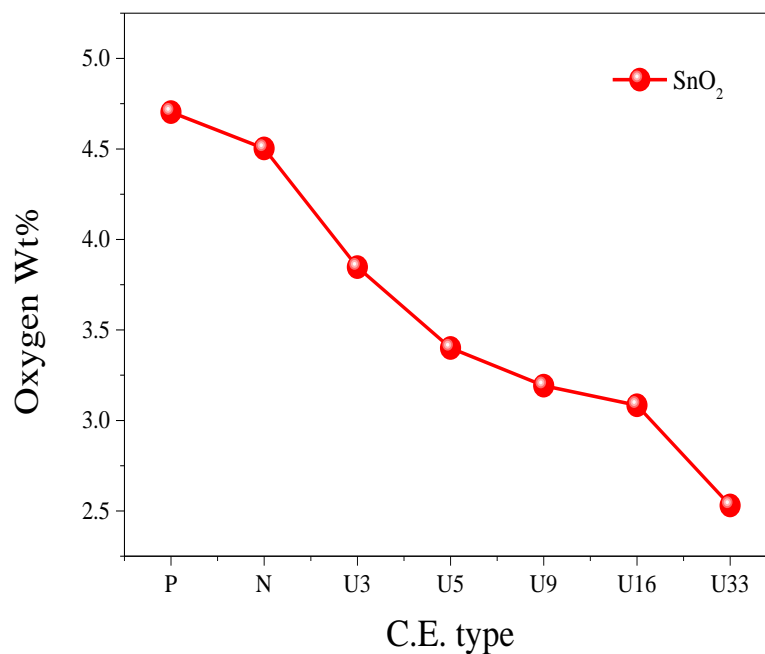


Figure 4.4. Oxygen wt% for SnO<sub>2</sub> film before and after urea pre-treatment with different urea wt%.

#### 4.1.3 SEM and EDS for ZnO CE films before and after urea-pretreatment

The surface morphology of fabricated ZnO CE films before and after urea-pretreatment with different urea wt% was performed and characterized by SEM and shown in figure 4.5. The surface morphology of pristine ZnO CE (P- ZnO) was found to be compact with little and tiny pores and cracks which considered as a disadvantage of preventing more electrolyte solution to get penetrated inside the CE and the overall triiodide ions reduction will be slow and inefficient and hence the overall catalytic activity of CE. The surface morphology of N<sub>2</sub>-annealed ZnO films in N<sub>2</sub> environment (N- ZnO) without urea pre-treatment was found to be very similar to pristine (P- ZnO) without significant change in film compactness with a small number of pores. On the other hand, when 3 wt% of urea was used for ZnO pretreatment prior to annealing in N<sub>2</sub> atmosphere

(U3-ZnO CE), pores and cracks were introduced in the film. The number of pores and voids increased when urea wt% increased to 5wt% for U5-ZnO CE. The number of pores was further increased linearly by increasing the wt% of urea to 9wt% for U9-ZnO CE, 16wt% for U16-ZnO and 16wt% for U16-ZnO CE. The increase in films pores and cracks linearly with increasing the urea wt% is due to the increase in the reducing  $H_2$  gas produced as a result of urea decomposition. More  $H_2$  gas evolution will lead to extract more oxygen atoms from metal oxide film in form  $H_2O$  vapor evolution which leaves more pores and cracks in metal oxide films.

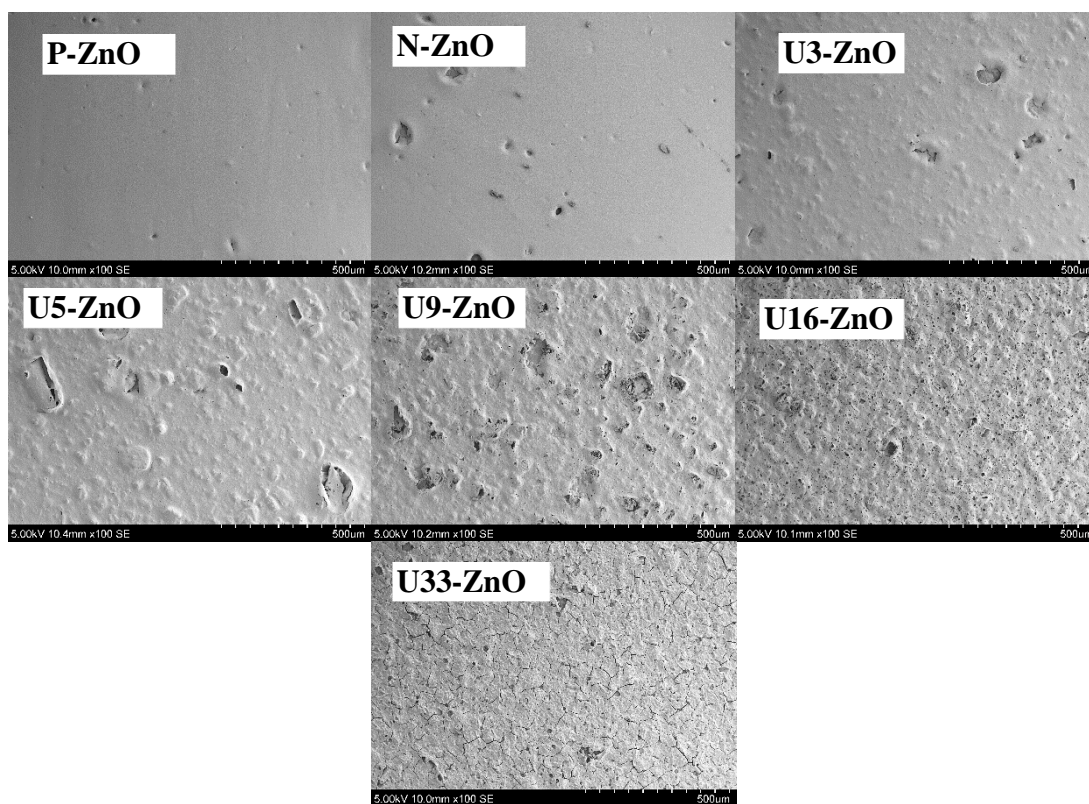


Figure 4.5. SEM images for pristine ZnO (P- ZnO),  $N_2$ -annealed ZnO (N-ZnO) and urea pre-treated  $N_2$ -annealed ZnO with different urea wt% (U3-ZnO, U5-ZnO, U9-ZnO, U16-ZnO, and U33-ZnO).

Energy dispersive X-ray spectroscopy was performed for all ZnO CE films before and after applying urea with the different urea wt%. This measurement was conducted to calculate the oxygen wt% inside the films by increasing the urea content for the pre-treated films. Figure 4.6 shows the plot of oxygen wt% and the different types of metal oxide CEs. It was found that the oxygen wt% for pristine (P-ZnO) metal oxide is the highest with a value of  $\sim 5.6\%$  after annealing in  $N_2$  atmosphere, the oxygen wt% in N-ZnO CE film decreased to  $\sim 5.3\%$  which indicates oxygen vacancies introduction after annealing. The oxygen wt% value decreased with increasing urea content for pre-treatment. Oxygen wt% has the values of  $\sim 5\%$ ,  $\sim 4.8\%$ ,  $\sim 4.45\%$ ,  $\sim 4.3\%$  and  $\sim 4.2\%$  for U3-ZnO, U5-ZnO, U9-ZnO, U16-ZnO and U33-ZnO CEs, respectively. The decrease in oxygen wt% by increasing urea wt% is direct support for the proposed hypothesis that higher urea content leads to lose of more oxygen for pre-treated ZnO metal oxide film.

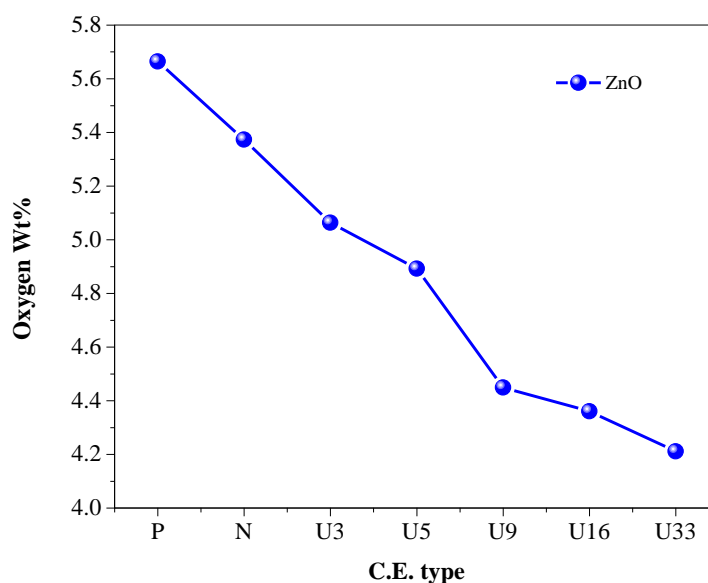


Figure 4.6. Oxygen wt% for ZnO films before and after urea pre-treatment with different urea wt%.

## 4.2 Mott-Schottky measurement for Band structure analysis

### 4.2.1 Mott-Schottky plot for n-type WO<sub>3</sub> metal oxide in triiodide/iodide electrolyte

Figure 4.7 shows the Mott-Schottky plot ( $1/Csc^2$  vs.  $V_A$ ) for pristine P-WO<sub>3</sub>, N<sub>2</sub>-annealed N-WO<sub>3</sub>, and different urea wt% pre-treated N<sub>2</sub>-annealed CEs. The intercept values of the linear plot with x-axis determine the values of  $V_{fb}$  which calculated and summarized in table 4.1. For pristine P-WO<sub>3</sub> CE the value of  $V_{fb}$  was -0.326 (vs. Ag/AgCl). For N<sub>2</sub> annealed non-treated N-WO<sub>3</sub> CEs, the  $V_{fb}$  value was positively increased to -0.227 (vs. Ag/AgCl). This positive increase in  $V_{fb}$  which is attributed to the introduction of oxygen vacancies which can cause an increase in the electron affinity of metal oxide and hence the conduction band minima (CBM) of metal oxide will be down-shifted and the potential difference between CBM of metal oxide and Fermi-level of electrolyte will be reduced. Therefore, the potential needed to flatten the band bending at the interface between the metal oxide and electrolyte will decrease. The value of  $V_{fb}$  was further positively increased to be  $\sim -0.084$  for U3-WO<sub>3</sub> CE,  $-0.01$  for U5-WO<sub>3</sub> CE,  $\sim +0.053$  for U9-WO<sub>3</sub> CE,  $\sim +0.149$  for U16-WO<sub>3</sub> CE and  $\sim +0.288$  for U33-WO<sub>3</sub>. This positive increase in  $V_{fb}$  values with increasing the urea wt% pre-treatment is attributed to the increase in oxygen vacancies and hence the electron affinity of WO<sub>3</sub> will increase. The increase in electron affinity will lead to a downshift of CBM level of metal oxide to be closer in a position to the Fermi-level of redox electrolyte. It is noticed from figure 4.7 that the value of  $V_{fb}$  for U5-WO<sub>3</sub> CE is the lowest and this indicate both of CBM level of U5-WO<sub>3</sub> CE and redox potential level of electrolyte are aligned leading to no band bending will occur at the interface. Electrons will efficiently transfer through the interface between U5-WO<sub>3</sub> CE and electrolyte. Beyond this optimum condition, by increasing urea contents

for U9-WO<sub>3</sub>, U16-WO<sub>3</sub>, and U33-WO<sub>3</sub>,  $V_{fb}$  potential was found to be converted from negative to a positive potential. This could be attributed to that the position for CBM level down-shifted more to be lower than the redox potential level of electrolyte. Band bending will increase in the opposite direction at the interface between CE and electrolyte. Therefore, a positive potential is needed to flatten the band bending.

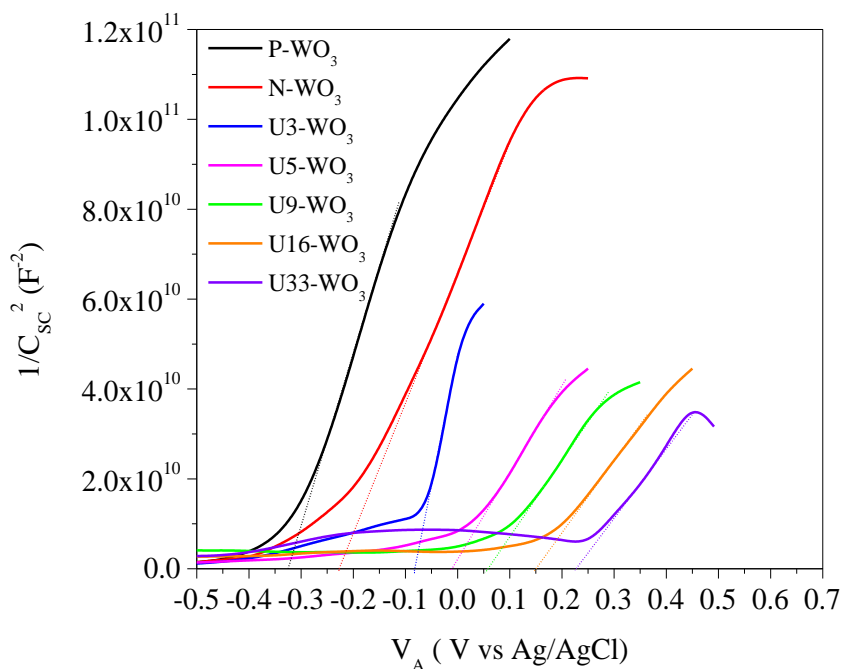


Figure 4.7. Mott-Schottky plot for WO<sub>3</sub> CE before and after urea pre-treatment with different urea wt%.

#### 4.2.2 Mott-Schottky plot for n-type SnO<sub>2</sub> metal oxide in triiodide/iodide electrolyte

Figure 4.8 shows the Mott-Schottky plot ( $1/C_{sc}^2$  vs.  $V_A$ ) for pristine P-SnO<sub>2</sub>, N<sub>2</sub>-annealed N-SnO<sub>2</sub>, and different urea wt% pre-treated N<sub>2</sub>-annealed CEs. The intercept values of the linear plot with x-axis determine the values of  $V_{fb}$  which calculated and summarized in table 4.1. For pristine P-SnO<sub>2</sub> CE, the value of  $V_{fb}$  was -0.307 (vs. Ag/AgCl). For N<sub>2</sub> annealed non-treated N-SnO<sub>2</sub> CEs, the  $V_{fb}$  value was positively increased

to -0.259 (vs. Ag/AgCl). This positive increase in  $V_{fb}$  which is attributed to the introduction of oxygen vacancies which can cause an increase in the electron affinity of metal oxide and hence the conduction band minima (CBM) of metal oxide will be down-shifted and the potential difference between CBM of metal oxide and Fermi-level of electrolyte will be reduced. Therefore, the potential needed to flatten the band bending at the interface between the metal oxide and electrolyte will decrease. The value of  $V_{fb}$  was further positively increased to be  $\sim -0.166$  for U3- SnO<sub>2</sub> CE,  $-0.093$  for U5- SnO<sub>2</sub> CE,  $\sim -0.7.6 \times 10^{-6}$  for U9- SnO<sub>2</sub> CE,  $\sim + 0.02$  for U16- SnO<sub>2</sub> CE, and  $\sim + 0.082$  for U33- SnO<sub>2</sub> CE. This positive increase in  $V_{fb}$  values with increasing the urea wt% pre-treatment is attributed to the increase in oxygen vacancies and hence the electron affinity of SnO<sub>2</sub> will increase. The increase in electron affinity will lead to a downshift of CBM level of metal oxide to be closer in a position to the Fermi-level (or redox potential) of redox electrolyte. It is noticed from figure 4.7 that the value of  $V_{fb}$  for U9- SnO<sub>2</sub> CE is the lowest which indicate that both of CBM level of U9-SnO<sub>2</sub> CE and redox potential level of electrolyte are aligned leading to no band bending will occur at the interface. As a result, electrons will efficiently transfer through the interface between U9-SnO<sub>2</sub> CE and electrolyte. Beyond this optimum condition, by increasing urea contents for U16-SnO<sub>2</sub>, and U33-SnO<sub>2</sub>,  $V_{fb}$  potential was found to be converted from negative to a positive potential. This could be attributed to that the position for CBM level down-shifted more to be lower than the redox potential level of electrolyte. As a result, band bending will increase in the opposite direction at the interface between CE and electrolyte. Therefore, a positive potential is needed to flatten the band bending.

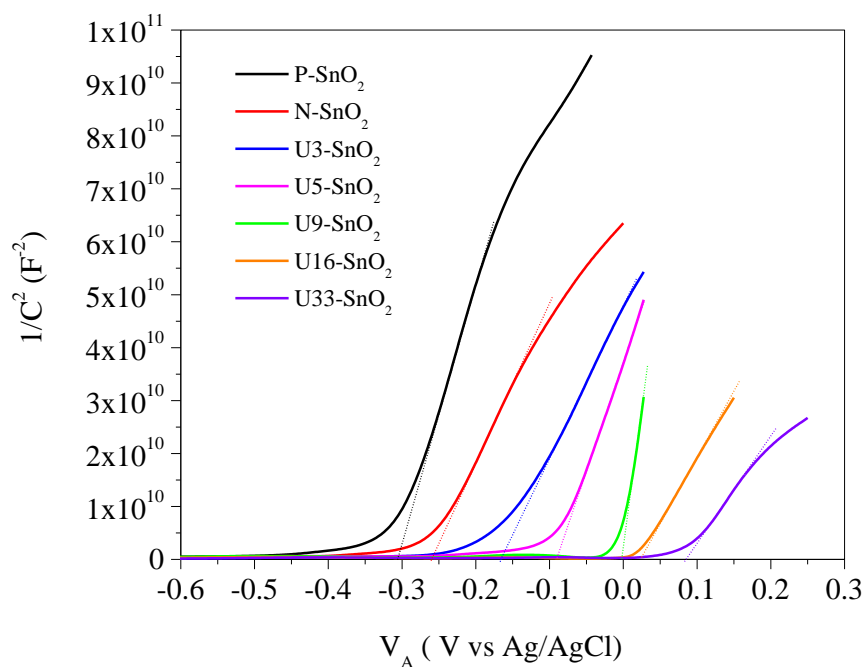


Figure 4.8. Mott-Schottky plot for SnO<sub>2</sub> CE before and after urea pre-treatment with different urea wt%.

#### 4.2.3 Mott-Schottky plot for n-type ZnO metal oxide in triiodide/iodide electrolyte

Figure 4.9 shows the Mott-Schottky plot ( $1/C_{sc}^2$  vs.  $V_A$ ) for pristine P-ZnO, N<sub>2</sub>-annealed N- SnO<sub>2</sub> and different urea wt% pre-treated N<sub>2</sub>-annealed CEs. The intercept values of the linear plot with x-axis determine the values of  $V_{fb}$  which calculated and summarized in table 4.1. For pristine P- ZnO CE, the value of  $V_{fb}$  was -0.313 (vs. Ag/AgCl). For N<sub>2</sub> annealed non-treated N- ZnO CEs, the  $V_{fb}$  value was positively increased to -0.287 (vs. Ag/AgCl). This positive increase in  $V_{fb}$  which is attributed to the introduction of oxygen vacancies which can cause an increase in the electron affinity of metal oxide and hence the conduction band minima (CBM) of metal oxide will be down-shifted and the potential difference between CBM of metal oxide and Fermi-level of electrolyte will be reduced. Therefore, the potential needed to flatten the band bending at the interface



between the metal oxide and electrolyte will decrease. The value of  $V_{fb}$  was further positively increased to be  $\sim -0.252$  for U3-ZnO CE,  $-0.191$  for U5-ZnO CE,  $\sim -0.1$  for U9-ZnO CE,  $\sim -0.02$  for U16-ZnO CE, and  $\sim +0.081$  for U33-ZnO. This positive increase in  $V_{fb}$  values with increasing the urea wt% pre-treatment is attributed to the increase in oxygen vacancies and hence the electron affinity of ZnO will increase. The increase in electron affinity will lead to a downshift of CBM level of metal oxide to be closer in a position to the Fermi-level of redox electrolyte. It is noticed from figure 4.7 that the value of  $V_{fb}$  for U9- ZnO CE. is the lowest which indicate that both of CBM level of U16-ZnO CE and redox potential level of electrolyte are aligned leading to no band bending will occur at the interface. Electrons will efficiently transfer through the interface between U16- ZnO CE and electrolyte. Beyond this optimum condition, by increasing urea contents for U33-ZnO,  $V_{fb}$  potential was found to be converted from negative to a positive potential. This could be attributed to that the position for CBM level down-shifted more to be lower than the redox potential level of electrolyte. As a result, band bending will increase in the opposite direction at the interface between CE and electrolyte. Therefore, a positive potential is needed to flatten the band bending.

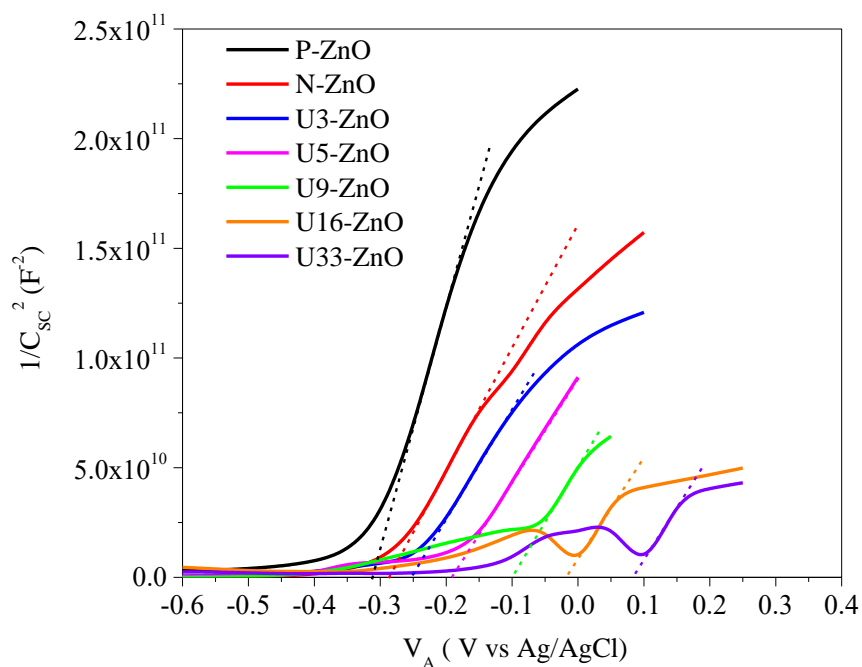


Figure 4.9. Mott-Schottky plot for ZnO CE before and after urea pre-treatment with different urea wt%.

Table 4.1 Flat band potential values ( $V_{fb}$ ) calculated from Mott-Schottky plot for  $\text{WO}_3$ ,  $\text{SnO}_2$ , and ZnO CEs before and after urea treatment with different mass ratios.

CE	Flat band potential $V_{fb}$ (vs. Ag/AgCl)
P-WO3	-0.32
N-WO3	-0.228
U3-WO3	-0.084
U5-WO3	-0.01
U9-WO3	+0.053
U16-WO3	+0.149
U33-WO3	+0.288
P-SnO2	-0.307

N-SnO <sub>2</sub>	-0.259
U3-SnO <sub>2</sub>	-0.166
U5-SnO <sub>2</sub>	-0.093
U9-SnO <sub>2</sub>	-7.6×10 <sup>-6</sup>
U16-SnO <sub>2</sub>	+0.02
U33-SnO <sub>2</sub>	+0.082
P-ZnO	-0.313
N-ZnO	-0.287
U3-ZnO	-0.252
U5-ZnO	-0.191
U9-ZnO	-0.1
U16-ZnO	-0.02
U33-ZnO	+0.081

### 4.3 Raman spectroscopy analysis

#### 4.3.1 Raman spectroscopy for WO<sub>3</sub> CE films before and after urea pre-treatment

Figure 4.10 shows Raman spectrum of WO<sub>3</sub> films before and after urea-pretreatment. Pristine WO<sub>3</sub> CE film shows four main peaks at 264 cm<sup>-1</sup>, 324 cm<sup>-1</sup>, 710 cm<sup>-1</sup> and 801 cm<sup>-1</sup>. The four peaks are attributed to the monoclinic crystal structure of WO<sub>3</sub> [77]. Raman peaks become broader with less peak intensity for N<sub>2</sub>-annealed WO<sub>3</sub> (N-WO<sub>3</sub>) suggesting a degradation of WO<sub>3</sub> crystallinity as a result of oxygen vacancies introduction to producing WO<sub>3-x</sub>. By applying urea pre-treatment and annealing in N<sub>2</sub> gas, Raman peaks becomes broader and lower in intensity. The peaks intensity becomes even broader by increasing urea content until the peaks almost disappear in the case of the

highest urea wt% for U33-WO<sub>3</sub>. This result is very consistent with the previous reported Raman spectrum of WO<sub>2.9</sub> [77] which support the hypothesis that higher urea content increases oxygen vacancies for the pre-treated WO<sub>3</sub> CE.

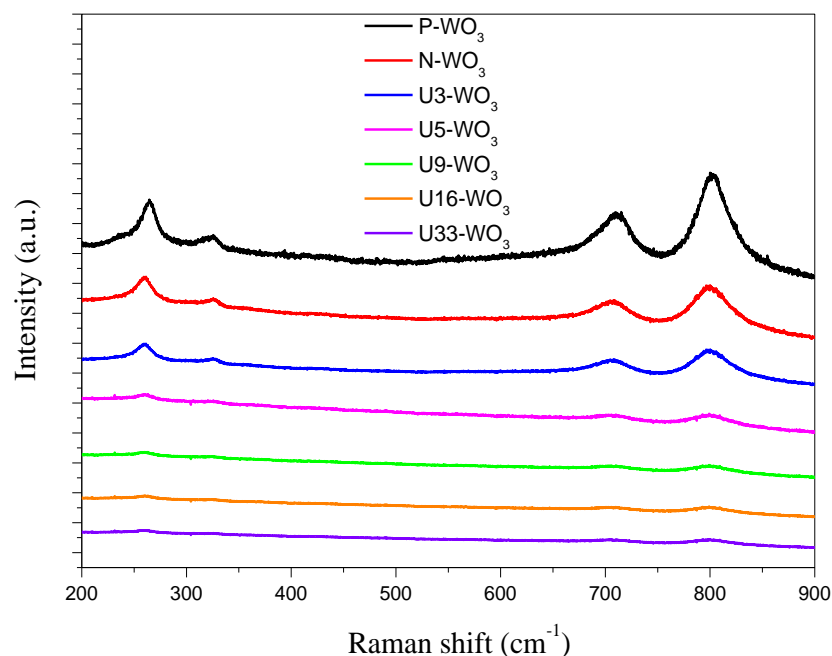


Figure 4.10. Raman spectroscopy of WO<sub>3</sub> CE before and after urea pre-treatment with different urea wt%.

#### 4.3.2 Raman spectroscopy for SnO<sub>2</sub> CE films before and after urea pre-treatment

Figure 4.11 shows Raman spectrum of SnO<sub>2</sub> films before and after urea-pre-treatment. Pristine SnO<sub>2</sub> CE film shows three main peaks at 472 cm<sup>-1</sup>, 631 cm<sup>-1</sup>, and 770 cm<sup>-1</sup>. The peak at 472 cm<sup>-1</sup> can be assigned to  $E_g$  mode, which is related to the vibration of oxygen in the oxygen plane [98]. The intensity of this peak was reduced significantly after annealing SnO<sub>2</sub> in N<sub>2</sub> (N- SnO<sub>2</sub>) due to the reduction of SnO<sub>2</sub> and the creation of oxygen vacancies. Peak intensity was further decreased and becomes broader by increasing urea

wt% for pre-treatment due to losing more oxygen atoms and creation of more oxygen vacancies until the peak almost disappears in the case of U33-SnO<sub>2</sub>. The other two peaks at 631 and 770 cm<sup>-1</sup> are assigned to the vibration modes induced by the expansion and contraction vibration mode of Sn-O bonds. It was found that the peaks were shifted towards lower energy and a decrease in intensity for these peaks after N<sub>2</sub> annealing and urea treatment. This is consistent with losing oxygen atoms by reducing the bonding energy of Sn-O. The peaks continue to be shifted towards lower energy as well as decreasing in intensity linearly with increasing the urea content of pre-treated CEs. Overall, SnO<sub>2</sub> was successfully reduced, and SnO<sub>2</sub> crystallinity decreased.

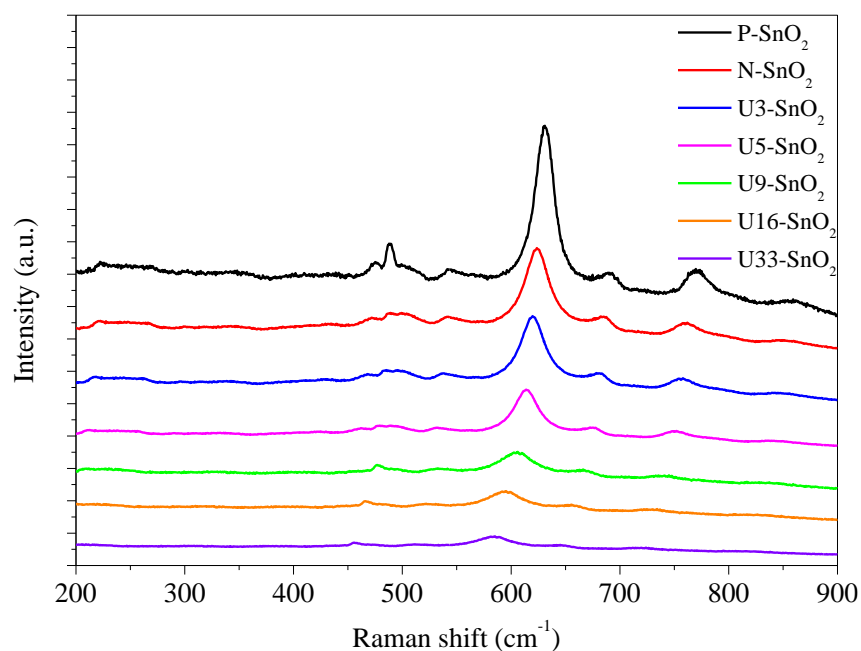


Figure 4.11. Raman spectroscopy of SnO<sub>2</sub> CE before and after urea pre-treatment with different urea wt%.

### 4.3.1 Raman spectroscopy for ZnO CE films before and after urea pre-treatment

Figure 4.12 shows Raman spectrum of ZnO films before and after urea pre-treatment. Pristine ZnO (P-ZnO) CE film shows three main peaks at  $345\text{ cm}^{-1}$ ,  $394\text{ cm}^{-1}$ , and  $450\text{ cm}^{-1}$ . The strongest peaks at  $345\text{ cm}^{-1}$  and  $450\text{ cm}^{-1}$  are attributed to the vibrational motion of oxygen atoms [45, 46]. The intensity of these peaks was significantly decreased in  $\text{N}_2$ -annealed ZnO (N-ZnO) CE film due to oxygen atoms being removed from ZnO by annealing under  $\text{N}_2$ . The peak intensity even decreased more by increasing urea content for pre-treated ZnO CE. This decrease is a direct indication of creating more oxygen vacancies by increasing urea wt% pre-treatment. Therefore, the crystallinity of ZnO was degraded by reducing ZnO to  $\text{ZnO}_{1-x}$ .

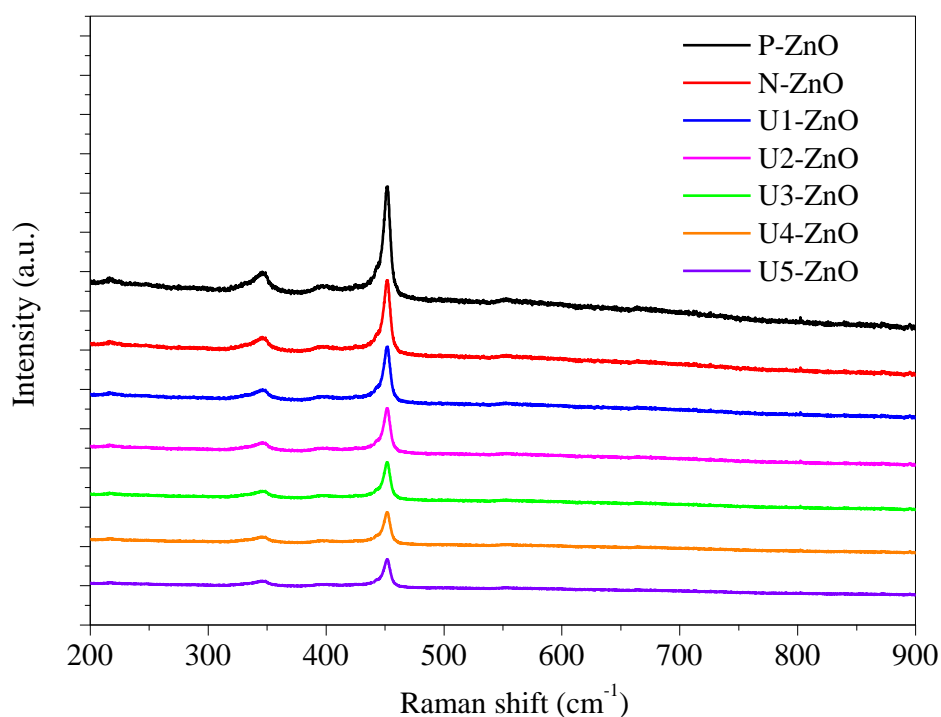


Figure 4.12. Raman spectroscopy of ZnO CE before and after urea pre-treatment with different urea wt%.

## 4.4 Optical band gap determination

### 4.4.1 Optical band gap values of WO<sub>3</sub> CE films before and after urea pre-treatment

Figure 4.13 shows *Tauc's* plots for pristine (P-WO<sub>3</sub>) WO<sub>3</sub>, N<sub>2</sub>-annealed (N-WO<sub>3</sub>) WO<sub>3</sub>, and urea pre-treated N<sub>2</sub>-annealed WO<sub>3</sub> with different urea wt% U3-WO<sub>3</sub>, U5-WO<sub>3</sub>, U9-WO<sub>3</sub>, U16-WO<sub>3</sub>, and U33-WO<sub>3</sub>. The electronic band gap transition is indirect band gap transition for WO<sub>3</sub> metal oxide where the exponent coefficient value (*n*) in equation 3.1 has a value of 2. The indirect optical band gap transition of WO<sub>3</sub> was confirmed previously by other studies [96, 99]. The intercept of curve lines with the x-axis as shown in figure 4.13 determines the value of the optical band gap (*E<sub>g</sub>*). The optical band value for pristine WO<sub>3</sub> (P-WO<sub>3</sub>) was calculated ~ 2.85 eV. After annealing in N<sub>2</sub>, the optical band gap was reduced to ~ 2.79 eV, and this decrease is attributed to the introduction of oxygen vacancies inside WO<sub>3</sub> metal oxide when annealed under N<sub>2</sub> atmosphere. As discussed in section 2.10, mid-gap donor states will be introduced close to both conduction and valence bands of metal oxide which lead to tail states formation and hence the band gap will be reduced. The optical band gap (*E<sub>g</sub>*) was further decreased to reach ~ 2.61 eV for U3-WO<sub>3</sub> CE. More oxygen vacancies mean more mid-gap donor states will be formed and as a result, the band gap will be reduced. The theory is consistent with the experimental results where the optical band gap (*E<sub>g</sub>*) values of WO<sub>3</sub> CEs were inversely proportional with urea wt% treatment. The value of *E<sub>g</sub>* was found to be ~ 2.45 eV, 2.34 eV, 2.22 eV and 2.08 eV for U5-WO<sub>3</sub>, U9-WO<sub>3</sub>, U16-WO<sub>3</sub> and U33-WO<sub>3</sub> CEs.

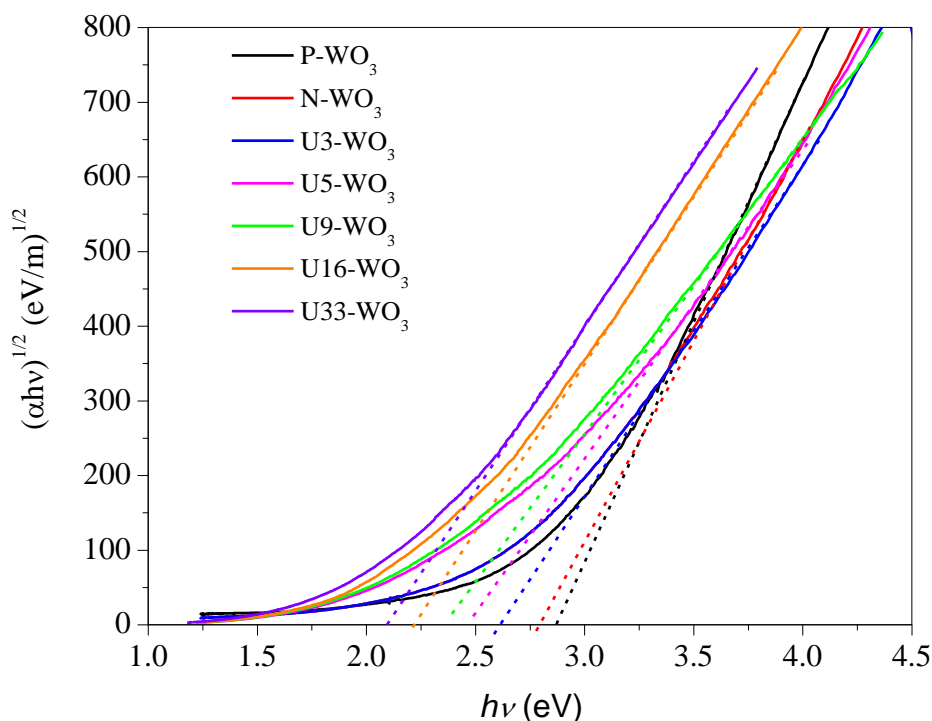


Figure 4.13 Tauc plot for  $\text{WO}_3$  before and after urea pre-treatment with different urea wt%.

#### 4.4.2 Optical band gap values of $\text{SnO}_2$ CE films before and after urea pre-treatment

Figure 4.14 shows *Tauc's* plots for pristine ( $\text{P-SnO}_2$ )  $\text{SnO}_2$ ,  $\text{N}_2$ -annealed ( $\text{N-SnO}_2$ )  $\text{SnO}_2$  and urea pre-treated  $\text{N}_2$ -annealed  $\text{SnO}_2$  with different urea wt%  $\text{U3-SnO}_2$ ,  $\text{U5-SnO}_2$ ,  $\text{U9-SnO}_2$ ,  $\text{U16-SnO}_2$ , and  $\text{U33-SnO}_2$ . The electronic band gap transition is indirect band gap transition for  $\text{SnO}_2$  metal oxide where the exponent coefficient value ( $n$ ) in equation 3.1 has a value of  $1/2$ . The indirect optical band gap transition of  $\text{SnO}_2$  was confirmed previously by other studies previously from other studies [42, 100]. The intercept of curve lines with the x-axis as shown in figure 4.13 determine the value of the optical band gap ( $E_g$ ). The optical band value for pristine  $\text{SnO}_2$  ( $\text{P-SnO}_2$ ) was calculated  $\sim 3.24$  eV. After annealing in  $\text{N}_2$ , the optical band gap was reduced to  $\sim 3.04$  eV, and this decrease is attributed to the introduction of oxygen vacancies inside  $\text{SnO}_2$  metal oxide when annealed



under  $N_2$  atmosphere. As discussed in section 2.10, mid-gap donor states will be introduced close to both conduction and valence bands of metal oxide which lead to tail states formation and hence the band gap will be reduced. The optical band gap ( $E_g$ ) was further decreased to reach  $\sim 2.86$  eV for U3-SnO<sub>2</sub> CE. More oxygen vacancies mean more mid-gap donor states will be formed and as a result, the band gap will be reduced. The theory is consistent with the experimental results where the optical band gap ( $E_g$ ) values of WO<sub>3</sub> CEs were inversely proportional with urea Wt% treatment. The value of  $E_g$  was found to be  $\sim 2.59$  eV, 2.49 eV, 2.38 eV and 2.27 eV for U5-SnO<sub>2</sub>, U9-SnO<sub>2</sub>, and U16-SnO<sub>2</sub> and U33-SnO<sub>2</sub> CEs.

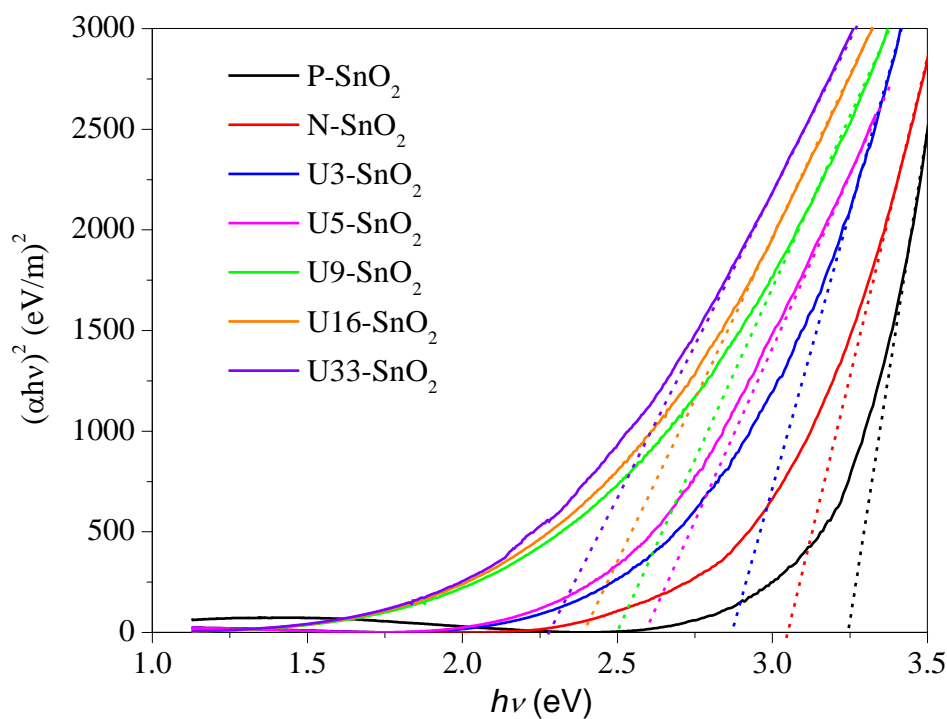


Figure 4.14 Tauc plots for SnO<sub>2</sub> before and after urea pre-treatment with different urea wt%.

#### 4.4.3 Optical band gap values of ZnO CE films before and after urea pre-treatment

Figure 4.15 shows  $Tauc$  plots for pristine (P-ZNO) ZnO, N<sub>2</sub>-annealed (N-ZnO) ZnO and urea pre-treated N<sub>2</sub>-annealed ZnO with different urea wt% U3-ZnO, U5-ZnO, U9-ZnO, U16-ZnO, and U33-ZnO. The electronic band gap transition is indirect band gap transition for ZnO metal oxide where the exponent coefficient value ( $n$ ) in equation 3.1 has a value of 1/2. The indirect optical band gap transition of ZnO was confirmed previously by other studies previously from other studies [34, 101]. The intercept of curve lines with the x-axis as shown in figure 4.14 determine the value of the optical band gap ( $E_g$ ). The optical band value for pristine ZnO (P-ZnO) was calculated ~ 3.14 eV. After annealing in N<sub>2</sub>, the optical band gap was reduced to ~ 2.95 eV, and this decrease is attributed to the introduction of oxygen vacancies inside ZnO metal oxide when annealed under N<sub>2</sub> atmosphere. As discussed in section 2.10, mid-gap donor states will be introduced close to both conduction and valence bands of metal oxide which lead to tail states formation and hence the band gap will be reduced. The optical band gap ( $E_g$ ) was further decreased to reach ~ 2.73 eV for U3-ZnO CE. More oxygen vacancies mean more mid-gap donor states will be formed and as a result, the band gap will be reduced. The theory is consistent with the experimental results where the optical band gap ( $E_g$ ) values of WO<sub>3</sub> CEs were inversely proportional with urea wt% treatment. The value of  $E_g$  was found to be ~ 2.63 eV, 2.49 eV, 2.31 eV and 2.25 eV for U5-ZnO, U9-ZnO, and U16-ZnO and U33-ZnO CEs.

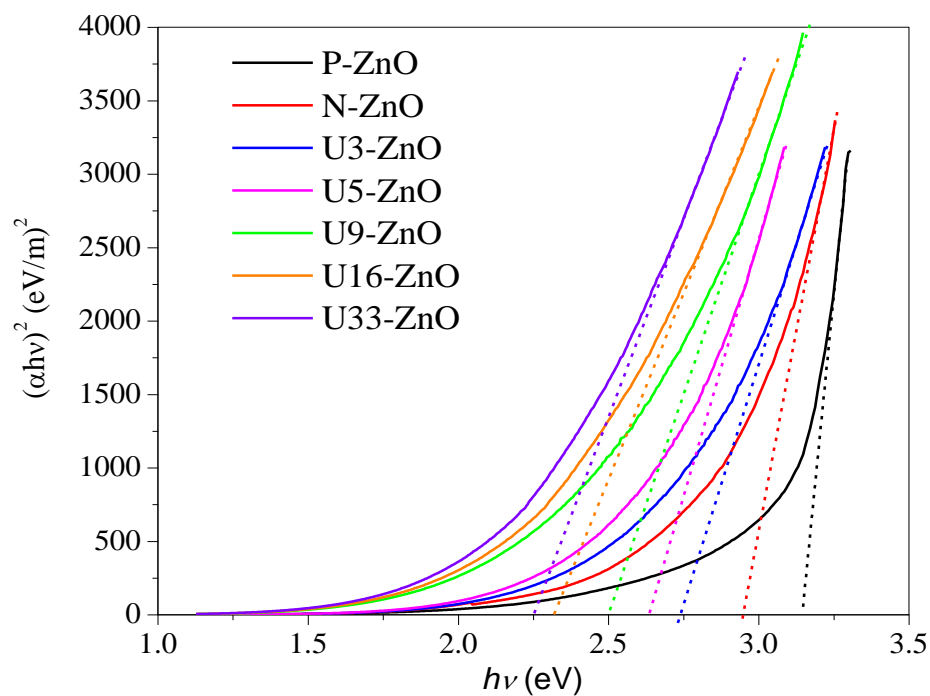


Figure 4.15 Tauc plot for ZnO before and after urea pre-treatment with different urea wt%.

#### 4.5 Cyclic voltammetry measurements (CV)

Cyclic voltammetry (CV) is the most widely used technique for acquiring qualitative information about the electrochemical reaction. Figure 4.16 shows an example of cyclic voltammetry plot in case of redox ( $I^-/I_3^-$ ) iodide/triiodide electrolyte.

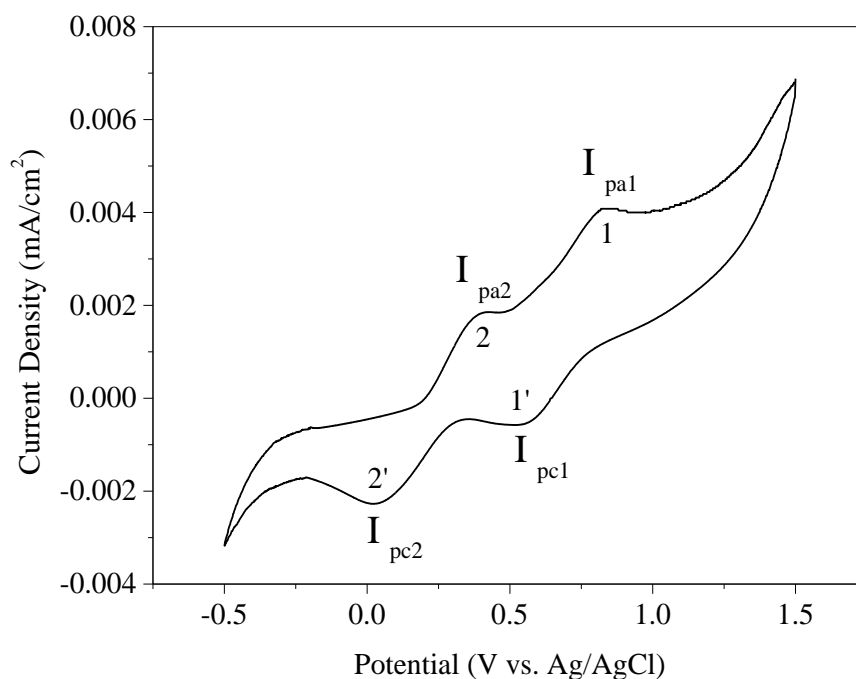
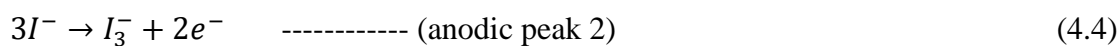
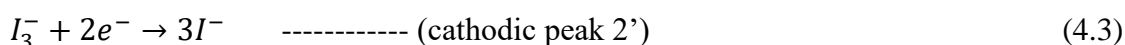
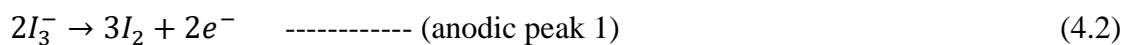
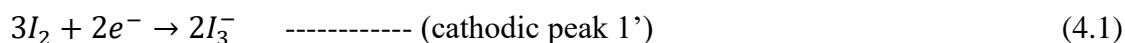


Figure 4.16 Cyclic voltammetry plot for iodide/ triiodide electrolyte.

Figure 4.16 shows two pairs of peaks (1, 1') and (2, 2') each peak is attributed to different reaction as follows:



The first two reactions do not affect significantly on the catalytic performance of the CE comparing to the last two reactions [41, 102]. The catalytic activity of CE toward iodide/triiodide redox electrolyte determined by the value of both anodic and cathodic currents ( $I_{pc}$  and  $I_{pa}$ ).

#### 4.5.1 Cyclic voltammetry measurements of WO<sub>3</sub> CE before and after urea pre-treatment

Figure 4.17 shows the cyclic voltammetry plot (current density mA/cm<sup>2</sup> vs. potential) for pristine WO<sub>3</sub> (P-WO<sub>3</sub>), N<sub>2</sub>-annealed (N-WO<sub>3</sub>) WO<sub>3</sub> film as well as urea pre-treated WO<sub>3</sub> CE with different urea wt% (U3-WO<sub>3</sub>, U5-WO<sub>3</sub>, U9-WO<sub>3</sub>, U16-WO<sub>3</sub>, and U33-WO<sub>3</sub>). The cyclic voltammetry plot shows almost straight line with neither cathodic nor anodic peaks for P-WO<sub>3</sub> film and this because the pristine film is catalytic inactive toward redox electrolyte. By annealing WO<sub>3</sub> film under N<sub>2</sub> atmosphere, both cathodic and anodic peak currents (I<sub>pc</sub> and I<sub>pa</sub>) increased. This increase is attributed to the introduction of oxygen vacancies which acts as active sites for triiodide (I<sub>3</sub><sup>-</sup>) ions reduction and hence improving the catalytic activity of the CE. By treating WO<sub>3</sub> CE films with urea, two pairs of peaks start to appear. Anodic and cathodic peaks pair on the right which attributed to the reactions in equations 4.1 and 4.2 are insignificant for determining the catalytic performance of the CE. The left anodic and cathodic peak pair which attribute to the reactions in equations 4.3 and 4.4 are the most significant peaks for determining the catalytic performance of CE. The anodic and cathodic current intensities for the later peaks were increased by increasing urea wt%. The increase could be attributed to more oxygen introduced and hence more reduction active sites for triiodide ions. However, the enhancement in WO<sub>3</sub> CE catalytic performance did not increase unlimitedly. The optimum catalytic performance was assigned to U5-WO<sub>3</sub> CE with 5 wt% of urea treatment of WO<sub>3</sub>. This result is very consistent with Mott-Schottky results in which U5-WO<sub>3</sub> CE was expected to has the highest catalytic performance due to the alignment of both conduction band minima (CBM) of U5-WO<sub>3</sub> CE and redox potential of electrolyte leading to the

minimal band bending and better electron transfer at the interface between U5-WO<sub>3</sub> CE and electrolyte. Beyond this optimum urea wt%, the overall catalytic performance decreased by increasing urea wt% in case of U9-WO<sub>3</sub>, U16-WO<sub>3</sub>, and U33-WO<sub>3</sub> CEs. This reduction in catalytic performance is attributed to the increase of band bending at the interface between U9-WO<sub>3</sub>, U16-WO<sub>3</sub> and U33-WO<sub>3</sub> CEs and electrolyte as discussed in Mott-Schottky analysis. As a result, the electron transfer from counter electrode to electrolyte will be slower and inefficient.

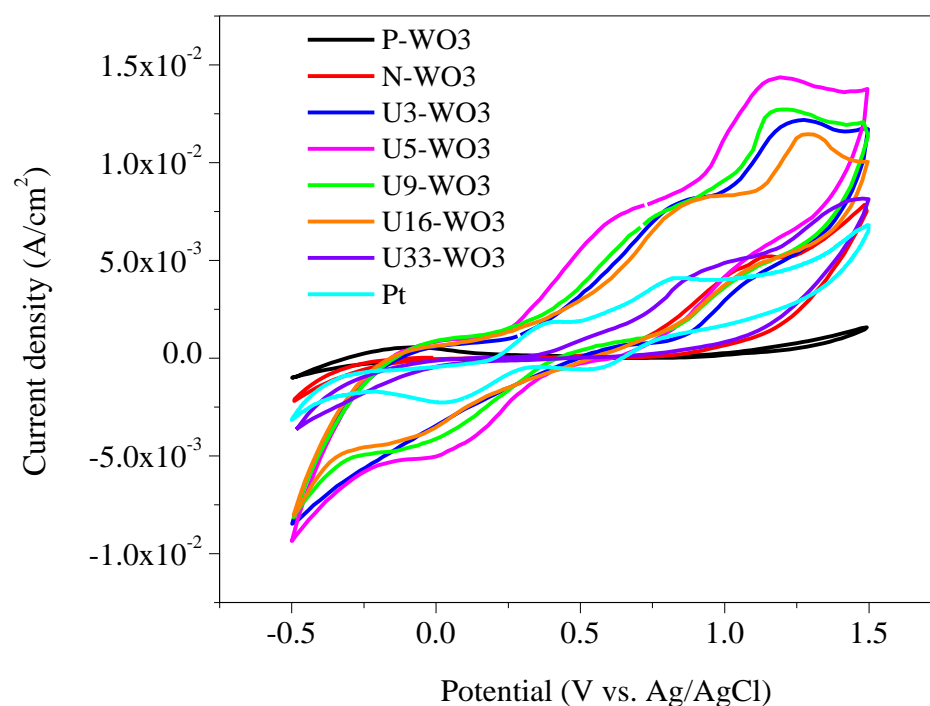


Figure 4.17 Cyclic voltammetry plots for iodide/ triiodide electrolyte with WO<sub>3</sub> CE before and after urea pre-treatment with different urea wt%.

#### 4.5.2 Cyclic voltammetry measurements of SnO<sub>2</sub> CE before and after urea pre-treatment

Figure 4.18 shows the cyclic voltammetry plot (current density mA/cm<sup>2</sup> vs potential) for pristine SnO<sub>2</sub> (P-SnO<sub>2</sub>), N<sub>2</sub>-annealed (N- SnO<sub>2</sub>) SnO<sub>2</sub> film as well as urea pre-treated SnO<sub>2</sub> CE with different urea wt% (U3- SnO<sub>2</sub>, U5- SnO<sub>2</sub>, U9- SnO<sub>2</sub>, U16- SnO<sub>2</sub> and U33- SnO<sub>2</sub>). The cyclic voltammetry plot shows almost straight line with neither cathodic nor anodic peaks for P- SnO<sub>2</sub> film and this because the pristine film is catalytic inactive toward redox electrolyte. By annealing SnO<sub>2</sub> film under N<sub>2</sub> atmosphere, both cathodic and anodic peak currents ( $I_{PC}$  and  $I_{Pa}$ ) increased. This increase is attributed to the introduction of oxygen vacancies which acts as active sites for triiodide (I<sub>3</sub><sup>-</sup>) ions reduction and hence improving the catalytic activity of the CE. By treating SnO<sub>2</sub> CE films with urea, two pairs of peaks start to appear. Anodic and cathodic peaks pair on the right which attributed to the reactions in equations 4.1 and 4.2 are insignificant for determining the catalytic performance of the CE. The left anodic and cathodic peak pair which attribute to the reactions in equations 4.3 and 4.4 are the most significant peaks for determining the catalytic performance of CE. The anodic and cathodic current intensities for the later peaks were increased by increasing urea wt%. The increase could be attributed to more oxygen introduced and hence more reduction active sites for triiodide ions. However, the enhancement in SnO<sub>2</sub> CE catalytic performance did not increase unlimitedly. The optimum catalytic performance was assigned to U9-SnO<sub>2</sub> CE with 9wt% of urea treatment of SnO<sub>2</sub>. This result is very consistent with Mott-Schottky results in which U9-SnO<sub>2</sub> CE was expected to has the highest catalytic performance due to the alignment of both conduction band minima (CBM) of U9-SnO<sub>2</sub> CE and redox potential of electrolyte leading to the

minimal band bending and better electron transfer at the interface between U9-SnO<sub>2</sub> CE and electrolyte. Beyond this optimum urea wt%, the overall catalytic performance decreased by increasing urea wt% in case of U16- SnO<sub>2</sub> and U33-WO<sub>3</sub> CEs. This reduction in catalytic performance is attributed to the increase of band bending at the interface between U16-SnO<sub>2</sub> and U33-SnO<sub>2</sub> CEs and electrolyte as discussed in Mott-Schottky analysis. As a result, the electron transfer from counter electrode to electrolyte will be slower and inefficient.

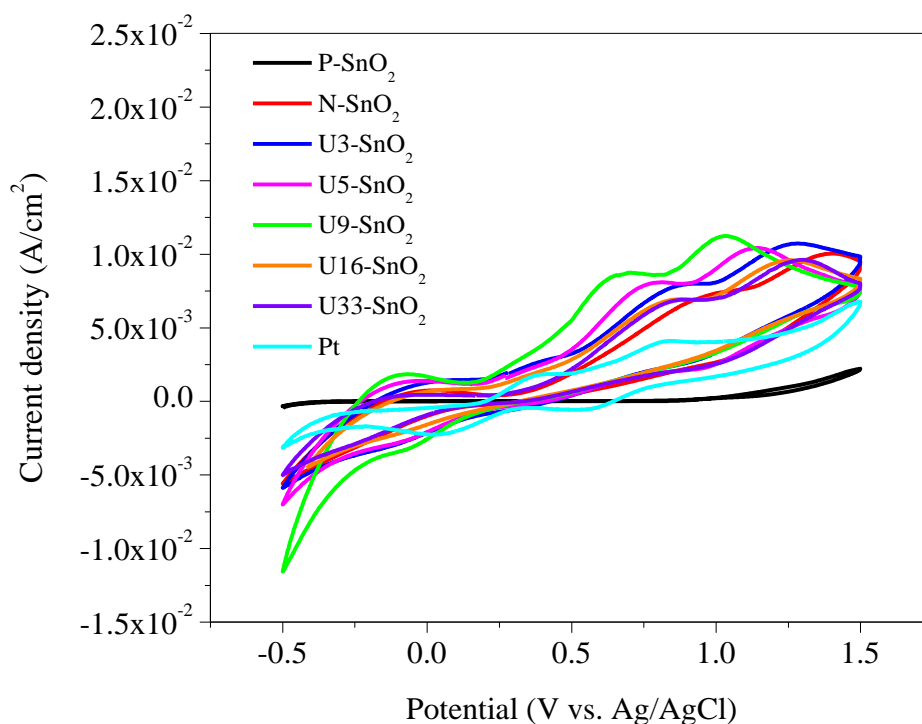


Figure 4.18 Cyclic voltammetry plots for iodide/ triiodide electrolyte with SnO<sub>2</sub> CE before and after urea pre-treatment with different urea wt%.



### 4.5.3 Cyclic voltammetry measurements of ZnO CE before and after urea pre-treatment

Figure 4.19 shows the cyclic voltammetry plot (current density mA/cm<sup>2</sup> vs. potential) for pristine ZnO (P- ZnO), N<sub>2</sub>-annealed (N- ZnO) ZnO film as well as urea pre-treated SnO<sub>2</sub> CE with different urea wt% (U3-ZnO, U5-ZnO, U9-ZnO, U16-ZnO, and U33-ZnO). The cyclic voltammetry plot shows almost straight line with neither cathodic nor anodic peaks for P-ZnO film and this because the pristine film is catalytic inactive toward redox electrolyte. By annealing ZnO film under N<sub>2</sub> atmosphere, both cathodic and anodic peak currents (I<sub>PC</sub> and I<sub>Pa</sub>) increased. This increase is attributed to the introduction of oxygen vacancies which acts as active sites for triiodide (I<sub>3</sub><sup>-</sup>) ions reduction and hence improving the catalytic activity of the CE. By treating ZnO CE films with urea, two pairs of peaks start to appear. Anodic and cathodic peaks pair on the right which attributed to the reactions in equations 4.1 and 4.2 are insignificant for determining the catalytic performance of the CE. The left anodic and cathodic peak pair which attribute to the reactions in equations 4.3 and 4.4 are the most significant peaks for determining the catalytic performance of CE. The anodic and cathodic current intensities for the later peaks were increased by increasing urea wt%. The increase could be attributed to more oxygen introduced and hence more reduction active sites for triiodide ions. However, the enhancement in ZnO CE catalytic performance did not increase unlimitedly. The optimum catalytic performance was assigned to U16-ZnO CE with 16wt% of urea treatment of ZnO. This result is very consistent with Mott-Schottky results in which U16- ZnO CE was expected to has the highest catalytic performance due to the alignment of both conduction band minima (CBM) of U16- ZnO CE and redox potential of electrolyte leading to the

minimal band bending and better electron transfer at the interface between U16-ZnO CE and electrolyte. Beyond this optimum urea wt%, the overall catalytic performance decreased by increasing urea wt% in case of U33-ZnO CE. This reduction in catalytic performance is attributed to the increase of band bending at the interface between U33-ZnO CE and electrolyte as discussed in Mott-Schottky analysis. As a result, the electron transfer from counter electrode to electrolyte will be slower and inefficient.

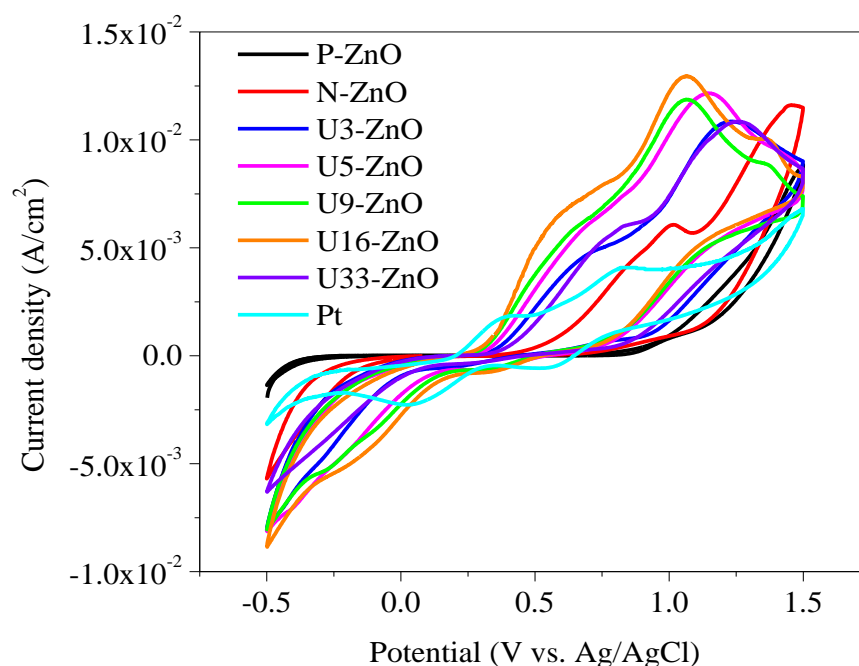


Figure 4.19 Cyclic voltammetry plots for iodide/ Triiodide electrolyte with ZnO CE before and after urea pre-treatment.

#### 4.6 Electrochemical impedance spectroscopy (EIS)

Electrochemical impedance spectroscopy (EIS) is another helpful technique to determine the catalytic performance of CEs towards electrolyte. By calculating the complex impedance of the interface between catalyst (CE) and electrolyte  $Z = Z' \pm iZ''$

where  $Z'$  and  $Z''$  are the real and imaginary components of the complex impedance  $Z$  when AC signal is applied to perturb the system. EIS measurement was performed for dummy cells. Two identical CEs sealed together with electrolyte in between. The equivalent electrical circuit if figure 4.19 is used for modeling to calculate series resistance ( $R_S$ ) which determine the electronic conductivity of the CE, charge transfer resistance ( $R_{CT}$ ) which determine interface resistance for electron transfer between CE / Electrolyte, and constant phase element (CPE) or imperfect double layer capacitance as shown in figure 4.20. All fitting process were done by EC-lab® software, BioLogic Science Instruments.

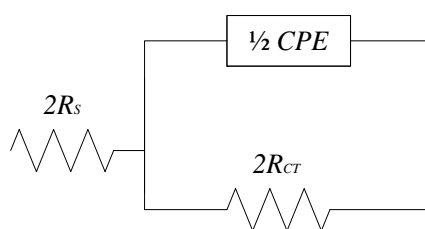


Figure 4.20 Equivalent circuit used of symmetric dummy cell used for EIS measurement modeling and fitting.

#### 4.6.1 Electrochemical impedance spectroscopy of $\text{WO}_3$ CE before and after urea pre-treatment

Figure 4.21 shows Nyquist plot of pristine  $\text{WO}_3$  (P- $\text{WO}_3$ ) CE,  $\text{N}_2$ -annealed  $\text{WO}_3$  (N- $\text{WO}_3$ ) and  $\text{N}_2$ -annealed of urea pre-treated  $\text{WO}_3$  CE dummy cells with different urea wt% (U3- $\text{WO}_3$ , U5- $\text{WO}_3$ , U9- $\text{WO}_3$ , U16- $\text{WO}_3$  and U33- $\text{WO}_3$ ). All fitted parameters were summarized in table 4.2. Pristine  $\text{WO}_3$  (P- $\text{WO}_3$ ) CE shows the lowest catalytic performance represented by the highest series resistance ( $R_S$ ) and higher charge transfer resistance ( $R_{CT}$ ). By annealing  $\text{WO}_3$  CE under  $\text{N}_2$ , both  $R_S$  and  $R_{CT}$  values were decreased, and the overall catalytic performance was improved. This improvement is attributed to the

introduction of oxygen vacancies which acts as reduction active sites to facilitate the electrons transport from the CE to the electrolyte. The catalytic performance of  $\text{WO}_3$  CE was further improved for urea treated U3- $\text{WO}_3$  CE with 3wt% of urea. The improvement was represented by a decrease in both  $R_S$  and  $R_{CT}$  values due to the increase of oxygen vacancies or reduction active sites for better electrolyte reduction process. The optimum catalytic performance was assigned for U5- $\text{WO}_3$  CE with 5wt% urea pre-treatment which has the lowest  $R_S$  and  $R_{CT}$  values. This result is very consistent with both Mott-Schottky and Cyclic voltammetry results in which U5- $\text{WO}_3$  CE has the optimum catalytic performance toward iodide/triiodide electrolyte. Beyond this optimum urea wt%, the overall catalytic performance decreased by increasing urea wt% in case of U9- $\text{WO}_3$ , U16- $\text{WO}_3$ , and U33- $\text{WO}_3$  CEs. This reduction in catalytic performance is attributed to the increase of band bending at the interface between U9- $\text{WO}_3$ , U16- $\text{WO}_3$  and U33- $\text{WO}_3$  CEs and electrolyte as discussed in Mott-Schottky analysis. As a result, the electron transfer from counter electrode to electrolyte will be slower and inefficient.

Compared to Pt CE, the catalytic performance of U5- $\text{WO}_3$  CE is better represented by lower  $R_{CT}$  and  $R_S$  values. The Same trend was observed in catalytic performance in cyclic voltammetry measurement. The same trend was found for the capacitance values calculated and summarized in table 4.2. The lowest capacitance was found to be for Pt CE due to its planner interfacial active surface area in contact with the electrolyte. The interfacial surface area and capacitance of P- $\text{WO}_3$  CE are close to the capacitance value of Pt CE capacitance. This is consistent with SEM images for P- $\text{WO}_3$  surface morphology showing a compact and dense film with no porosity. The higher capacitance for urea pre-treated CEs is attributed to its porous structure as confirmed from SEM images in section

4.1.1. The highest capacitance value was found for U5-WO<sub>3</sub> CE indicating the higher interfacial active surface area in contact with triiodide ions for efficient reduction process.

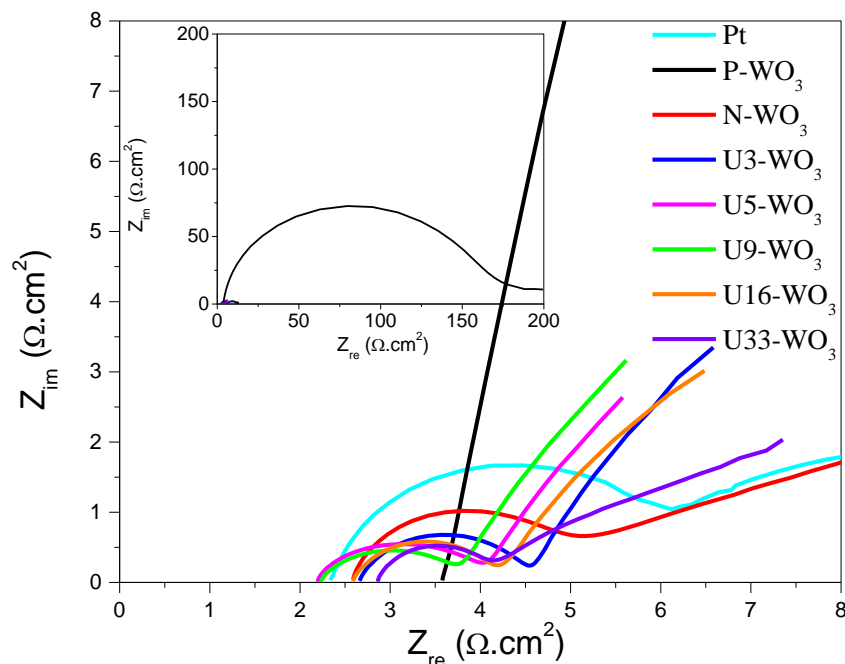


Figure 4.21 Nyquist plots for symmetrical dummy cells of WO<sub>3</sub> CE before and after urea pre-treatment with different urea wt%.

#### 4.6.2 Electrochemical impedance spectroscopy of SnO<sub>2</sub> CE before and after urea pre-treatment

Figure 4.22 shows Nyquist plot of pristine SnO<sub>2</sub> (P- SnO<sub>2</sub>) CE, N<sub>2</sub>-annealed SnO<sub>2</sub> (N- SnO<sub>2</sub>) and N<sub>2</sub>-annealed of urea pre-treated SnO<sub>2</sub> CE dummy cells with different urea wt% (U3- SnO<sub>2</sub>, U5- SnO<sub>2</sub>, U9- SnO<sub>2</sub>, U16- SnO<sub>2</sub> and U33- SnO<sub>2</sub>). All fitted parameters were summarized in table 4.2. Pristine SnO<sub>2</sub> (P- SnO<sub>2</sub>) CE shows the lowest catalytic performance represented by the highest series resistance ( $R_s$ ) and higher charge transfer resistance ( $R_{CT}$ ). By annealing SnO<sub>2</sub> CE under N<sub>2</sub>, both  $R_s$  and  $R_{CT}$  values were decreased,

and the overall catalytic performance was improved. This improvement is attributed to the introduction of oxygen vacancies which acts as reduction active sites to facilitate the electrons transport from the CE to the electrolyte. The catalytic performance of SnO<sub>2</sub> CE was further improved for urea treated U3-SnO<sub>2</sub> and U5-SnO<sub>2</sub> CEs with 3wt% and 5wt% of urea, respectively. The improvement was represented by a decrease in both  $R_S$  and  $R_{CT}$  values due to the increase of oxygen vacancies or reduction active sites for better electrolyte reduction process. The optimum catalytic performance was assigned for U9-SnO<sub>2</sub> CE with 9wt% urea pre-treatment which has the lowest  $R_S$  and  $R_{CT}$  values. This result is very consistent with both Mott-Schottky and Cyclic voltammetry results in which U9-SnO<sub>2</sub> CE has the optimum catalytic performance toward iodide/triiodide electrolyte. Beyond this optimum urea wt%, the overall catalytic performance decreased by increasing urea wt% in case of U16-SnO<sub>2</sub> and U33-SnO<sub>2</sub> CEs. This reduction in catalytic performance is attributed to the increase of band bending at the interface between U16-SnO<sub>2</sub> and U33-SnO<sub>2</sub> CEs and electrolyte as discussed in Mott-Schottky analysis. As a result, the electron transfer from counter electrode to electrolyte will be slower and inefficient.

Compared to Pt CE, the catalytic performance of U9-SnO<sub>2</sub> CE is better represented by lower  $R_{CT}$  and  $R_S$  values. The Same trend was observed in catalytic performance in cyclic voltammetry measurement. The same trend was found for the capacitance values calculated and summarized in table 4.2. The lowest capacitance was found to be for Pt CE due to its planner interfacial active surface area in contact with the electrolyte. The interfacial surface area and capacitance of P-SnO<sub>2</sub> CE are close to the capacitance value of Pt CE capacitance. This is consistent with SEM images for P- SnO<sub>2</sub> surface morphology showing a compact and dense film with no porosity. The higher capacitance for urea pre-

treated CEs is attributed to its porous structure as confirmed from SEM images in section 4.1.2. The highest capacitance value was found for U9-SnO<sub>2</sub> CE indicating the higher interfacial active surface area in contact with triiodide ions for efficient reduction process.

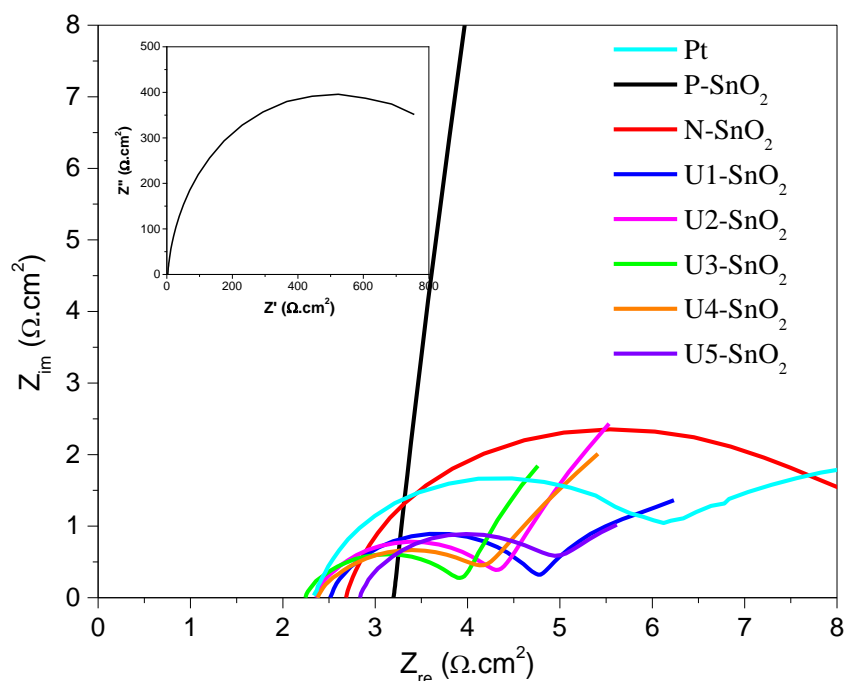


Figure 4.22 Nyquist plots for symmetrical dummy cells of SnO<sub>2</sub> CE before and after urea pre-treatment with different urea wt%.

#### 4.6.3 Electrochemical impedance spectroscopy of ZnO CE before and after urea pre-treatment

Figure 4.23 shows Nyquist plot of pristine ZnO (P-ZnO) CE, N<sub>2</sub>-annealed ZnO (N-ZnO) and N<sub>2</sub>-annealed of urea pre-treated ZnO CE dummy cells with different urea wt% (U3-ZnO, U5-ZnO, U9-ZnO, U16-ZnO and U33-ZnO). All fitted parameters were summarized in table 4.2. Pristine ZnO (P-ZnO) CE shows the lowest catalytic performance represented by the highest series resistance ( $R_s$ ) and higher charge transfer resistance ( $R_{CT}$ ).

By annealing SnO<sub>2</sub> CE under N<sub>2</sub>, both  $R_S$  and  $R_{CT}$  values were decreased, and the overall catalytic performance was improved. This improvement is attributed to the introduction of oxygen vacancies which acts as reduction active sites to facilitate the electrons transport from the CE to the electrolyte. The catalytic performance of ZnO CE was further improved for urea treated U3- ZnO, U5-ZnO and U9-ZnO CEs with 3wt%, 5wt% and 9wt% of urea, respectively. The improvement was represented by a decrease in both  $R_S$  and  $R_{CT}$  values due to the increase of oxygen vacancies or reduction active sites for better electrolyte reduction process. The optimum catalytic performance was assigned for U16- ZnO CE with 16wt% urea pre-treatment which has the lowest  $R_S$  and  $R_{CT}$  values. This result is very consistent with both Mott-Schottky and Cyclic voltammetry results in which U16- ZnO CE has the optimum catalytic performance toward iodide/triiodide electrolyte. Beyond this optimum urea wt%, the overall catalytic performance decreased by increasing urea wt% in case of U33- ZnO CEs. This reduction in catalytic performance is attributed to the increase of band bending at the interface between U33- ZnO CEs and electrolyte as discussed in Mott-Schottky analysis. As a result, the electron transfer from counter electrode to electrolyte will be slower and inefficient.

Compared to Pt CE, the catalytic performance of U16-ZnO CE is better represented by lower  $R_{CT}$  and  $R_S$  values. The Same trend was observed in catalytic performance in cyclic voltammetry measurement. The same trend was found for the capacitance values calculated and summarized in table 4.2. The lowest capacitance was found to be for Pt CE due to its planner interfacial active surface area in contact with the electrolyte. The interfacial surface area and capacitance of P-ZnO CE are close to the capacitance value of Pt CE capacitance. This is consistent with SEM images for P-ZnO surface morphology



showing a compact and dense film with no porosity. The higher capacitance for urea pre-treated CEs is attributed to its porous structure as confirmed from SEM images in section 4.1.3. The highest capacitance value was found for U16- ZnO CE indicating the higher interfacial active surface area in contact with triiodide ions for efficient reduction process.

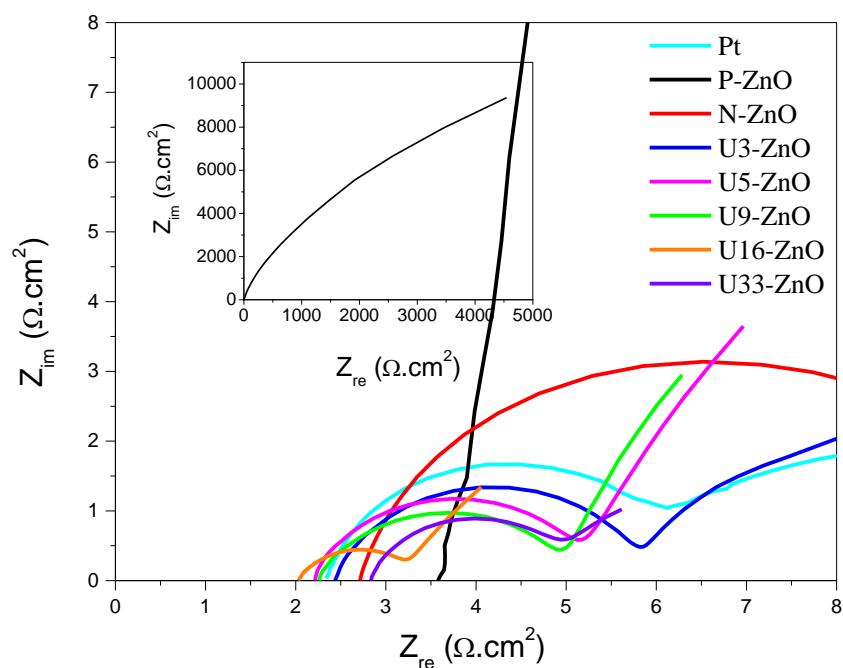


Figure 4.23 Nyquist plots for symmetrical dummy cells of ZnO CE before and after urea pre-treatment with different urea wt%.

Table 4.2. EIS fitted parameters extracted from Nyquist plots of respective dummy cells with WO<sub>3</sub>, SnO<sub>2</sub>, and ZnO CEs before and after urea treatment with different mass ratios in comparison to Pt CE based device.

CE	R <sub>s</sub> (Ω.cm <sup>2</sup> )	R <sub>CT</sub> (Ω.cm <sup>2</sup> )	C (F/cm <sup>2</sup> )
Pt	2.33	1.16	5.1 × 10 <sup>-6</sup>
P-WO <sub>3</sub>	3.57	85.3	8.14 × 10 <sup>-5</sup>
N-WO <sub>3</sub>	2.58	1.13	1 × 10 <sup>-4</sup>
U3-WO <sub>3</sub>	2.66	0.76	4 × 10 <sup>-4</sup>
<b>U5-WO<sub>3</sub></b>	<b>2.19</b>	<b>0.58</b>	<b>1.76 × 10<sup>-3</sup></b>
U9-WO <sub>3</sub>	2.23	0.75	1.82 × 10 <sup>-3</sup>
U16-WO <sub>3</sub>	2.58	0.9	3.9 × 10 <sup>-4</sup>
U33-WO <sub>3</sub>	2.86	0.91	1.44 × 10 <sup>-4</sup>
P-SnO <sub>2</sub>	3.18	925	2.36 × 10 <sup>-6</sup>
N- SnO <sub>2</sub>	2.68	2.5	4.45 × 10 <sup>-6</sup>
U3-SnO <sub>2</sub>	2.51	1.14	10.73 × 10 <sup>-6</sup>
U5-SnO <sub>2</sub>	2.36	0.99	2.77 × 10 <sup>-5</sup>
<b>U9-SnO<sub>2</sub></b>	<b>2.24</b>	<b>0.87</b>	<b>4.67 × 10<sup>-5</sup></b>
U16-SnO <sub>2</sub>	2.37	1.02	6.9 × 10 <sup>-5</sup>
U33-SnO <sub>2</sub>	2.83	1.14	1.4 × 10 <sup>-5</sup>
P-ZnO	3.57	26 × 10 <sup>3</sup>	5.22 × 10 <sup>-6</sup>
N-ZNO	2.71	7.8	2.9 × 10 <sup>-5</sup>
U3-ZnO	2.43	3.51	7.8 × 10 <sup>-4</sup>
U5-ZnO	2.26	3.07	1.44 × 10 <sup>-4</sup>
U9-ZnO	2.22	2.7	8.1 × 10 <sup>-3</sup>
<b>U16-ZnO</b>	<b>2.04</b>	<b>1.27</b>	<b>1.38 × 10<sup>-3</sup></b>
U33-ZnO	2.83	2.33	1.22 × 10 <sup>-4</sup>

#### 4.7 Current density-voltage characteristics (J-V)

Current-Voltage characteristics measurements determine the photovoltaic performance of the solar cell. Three main parameters can be extracted from **J-V** characteristics curve, short circuit current **J<sub>SC</sub>**, open circuit voltage (**V<sub>OC</sub>**) and curve Fill Factor (**FF**). Short circuit current (**J<sub>SC</sub>**) is the current value when the solar cell is in short circuit condition, or no voltage is applied to the solar cell (V=0) and mainly affected by the sensitizers used in DSSC cell and also affected by the charge recombination in the solar

cell. Open circuit voltage ( $V_{OC}$ ) is the voltage value when the solar cell is at open circuit condition or no current is extracted from the cell device ( $J=0$ ), and the value of  $V_{OC}$  is mainly determined by the potential value between the Fermi level of n-type material ( $\text{TiO}_2$  in DSSC device) and the redox potential of electrolyte. The fill factor parameter (FF) is the indication of curve squareness so high fill factor, a square shape the curve looks and the ideal  $FF$  value is  $\sim 1$  however this value will be for the ideal solar cell with no energy loss. In the real solar cell,  $FF$  value is ranging between 50-80% because of both series and shunt resistance of solar cell which can reduce the  $FF$  value. For higher  $FF$  value, series resistance should be lower, and shunt resistance should be higher.

#### **4.7.1 Current density-voltage (J-V) curves of $\text{WO}_3$ CE before and after urea pre-treatment**

Figure 4.24 shows J-V curve DSSC device made of the different CEs, pristine  $\text{WO}_3$  (P-  $\text{WO}_3$ ) CE,  $\text{N}_2$ -annealed  $\text{WO}_3$  (N-  $\text{WO}_3$ ) and  $\text{N}_2$ -annealed urea pre-treated  $\text{WO}_3$  with different urea wt% (U3- $\text{WO}_3$ , U5- $\text{WO}_3$ , U9- $\text{WO}_3$ , U16- $\text{WO}_3$ , and U33- $\text{WO}_3$ ) CEs. All photovoltaics parameters were calculated summarized in table 4.3. Pristine (P- $\text{WO}_3$ ) CE based device showed the lowest photovoltaics performance with power conversion efficiency (PCE %) of  $\sim 3.3\%$ , FF of  $\sim 24\%$  and  $V_{OC}$  of  $\sim 0.78$  V. The reason for the low photovoltaic performance of P- $\text{WO}_3$  based device is the poor catalytic activity of P- $\text{WO}_3$  CE toward triiodide ions reduction and hence inefficient dye regeneration from electrolyte lead to lower  $FF$ ,  $V_{OC}$ , and  $J_{SC}$  values. The photovoltaic performance was significantly increased for  $\text{N}_2$ -annealed  $\text{WO}_3$  (N- $\text{WO}_3$ ) CE based device. The overall power conversion efficiency (PCE %) value jumped from  $\sim 3.3\%$  to  $\sim 8.44\%$ . The most significant change was the increase in FF value from  $\sim 24\%$  to  $\sim 55\%$  by annealing the CE in  $\text{N}_2$  atmosphere.

This improvement in FF is attributed to the introduction of oxygen vacancies which facilitate the electron transfer from CE to the electrolyte. The value of  $V_{OC}$  also was slightly increased from 0.78 V to .08 V due to the increase of electron affinity after annealing in  $N_2$  leading to down shift of conduction band minima (CBM) of N- $WO_3$  CE. The result is consistent with Mott-Schottky results obtained. The overall device photovoltaic performance was further increased by applying urea-pretreatment of  $WO_3$  with different wt%. For U3- $WO_3$  CE-based device, PCE % value increased from 8.44% to 9.97% due to the increase of all photovoltaic parameters,  $FF$ ,  $V_{OC}$  and  $J_{SC}$  and this improvement is attributed to the creation more oxygen vacancies after applying urea pre-treatment which allows more electrons to reach electrolyte for more efficient  $I_3^-$  reduction and hence better overall device performance. This improvement was even increased for U5- $WO_3$  CE based device due to higher wt% of urea pre-treatment and hence more oxygen vacancies to facilitate more electrons for more efficient reduction of  $I_3^-$  ions. Fill factor was significantly increased to ~ 65% as well as  $V_{OC}$  value was increased to 0.85 V in the case of U5- $WO_3$  CE based device. As expected from Mott-Schottky, Cyclic voltammetry, and EIS measurements, U5- $WO_3$  CE based device has the optimum overall PCE % value due to the highest catalytic activity of U5- $WO_3$  CE. Beyond this optimum urea wt%, the overall catalytic performance decreased by increasing urea wt% in case of U9- $WO_3$ , U16- $WO_3$ , and U33- $WO_3$  CEs and therefore, the overall device performance will decrease. Short circuit current values ( $J_{SC}$ ) does not change significantly for the different types of CEs because  $J_{SC}$  value would change mainly depends on upon to the dye sensitizer. The optimum device performance was for U5- $WO_3$  CE based device with PCE value of ~ 11%

which is significantly higher than that the device performance for Pt CE with PCE value of  $\sim 9.5\%$ .

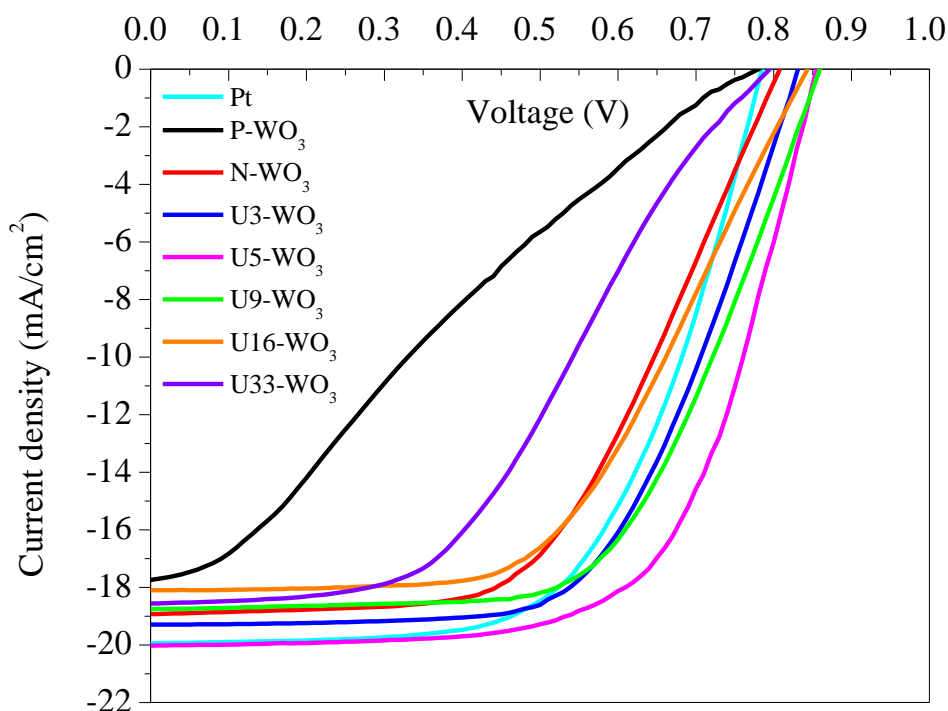


Figure 4.24 Current density-voltage ( $J$ - $V$ ) curves for DSSC devices with  $\text{WO}_3$  CEs before and after urea treatment with different wt% in comparison with Pt CE based devices.

DSSC devices based on U5- $\text{WO}_3$  CE were fabricated with different thicknesses of 5  $\mu\text{m}$ , 10  $\mu\text{m}$ , 15  $\mu\text{m}$ , 20  $\mu\text{m}$  and 25  $\mu\text{m}$  of CE to determine the optimum thickness of the highest device PCE%. Figure 4.25 shows the  $J$ - $V$  curves of DSSC devices based on U5- $\text{WO}_3$  CE with different thicknesses. By increasing the CE thickness, the fill factor of DSSC device increased until 15  $\mu\text{m}$  thickness based device which shows the highest  $FF$ . The reason for lower  $FF$  at smaller thicknesses could be attributed to the low interfacial surface area between electrolyte and CE due to the lower thickness and less material leading to

lower active sites for triiodide ions reduction. At higher thicknesses, the decrease in  $FF$  is mainly caused by the increase of series resistance of CE. Photovoltaic parameters were calculated for U5-WO<sub>3</sub> CE based device with different CE thicknesses and summarized in table 4.4.

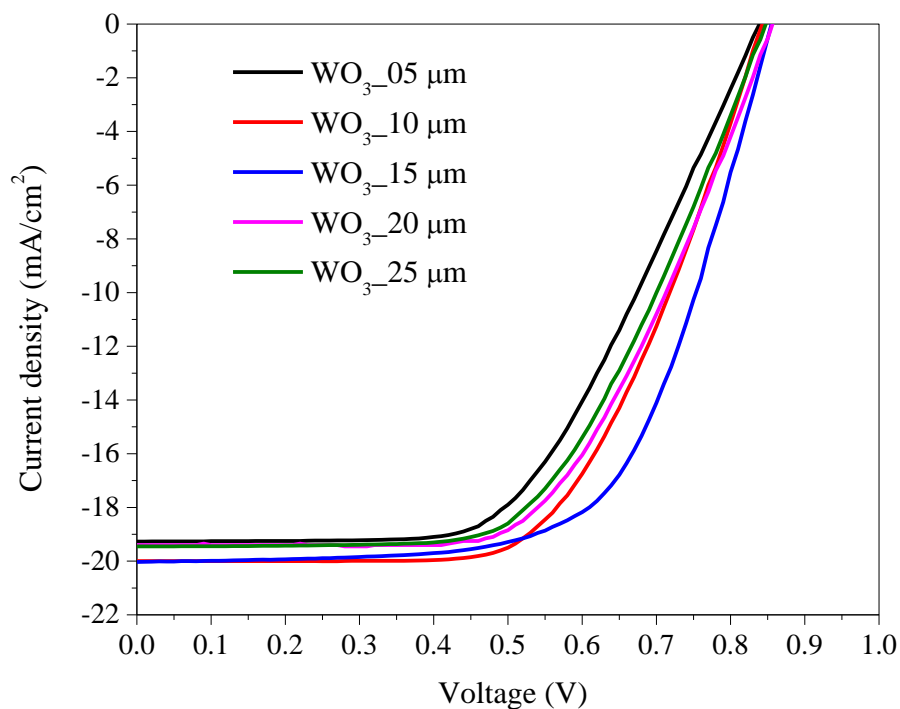


Figure 4.25 Current density-voltage ( $J$ - $V$ ) curves for DSSCs devices with U5-WO<sub>3</sub> CEs with different thicknesses.

#### 4.7.2 Current density - voltage characteristics ( $J$ - $V$ ) of SnO<sub>2</sub> CE before and after urea pre-treatment

Figure 4.26 shows  $J$ - $V$  curve DSSC device made of the different CEs, pristine SnO<sub>2</sub> (P-SnO<sub>2</sub>) CE, N<sub>2</sub>-annealed SnO<sub>2</sub> (N-SnO<sub>2</sub>) and N<sub>2</sub>-annealed urea pre-treated SnO<sub>2</sub> with different urea wt% (U3-SnO<sub>2</sub>, U5-SnO<sub>2</sub>, U9-SnO<sub>2</sub>, U16-SnO<sub>2</sub>, and U33-SnO<sub>2</sub>) CEs. All

photovoltaic parameters were calculated summarized in table 4.3. Pristine (P-SnO<sub>2</sub>) CE based device showed the lowest photovoltaic performance with power conversion efficiency (PCE %) of 2.76%, *FF* of 22% and *V<sub>OC</sub>* of ~ 0.73 V. The reason for the low photovoltaic performance of P-SnO<sub>2</sub> based device is the poor catalytic activity of P-SnO<sub>2</sub> CE toward triiodide ions reduction and hence inefficient dye regeneration from electrolyte lead to lower *FF*, *V<sub>OC</sub>*, and *J<sub>SC</sub>* values. The photovoltaic performance was significantly increased for N<sub>2</sub>-annealed SnO<sub>2</sub> (N-SnO<sub>2</sub>) CE based device. The overall power conversion efficiency (PCE %) value jumped from ~ 3.3% to ~ 7.1%. The most significant change was the increase in *FF* value from ~ 24% to ~ 55% by annealing the CE in N<sub>2</sub> atmosphere. This improvement in *FF* is attributed to the introduction of oxygen vacancies which facilitate the electron transfer from CE to the electrolyte. The value of *V<sub>OC</sub>* also was slightly increased from 0.73 V to .075 V due to the increase of electron affinity after annealing in N<sub>2</sub> leading to down shift of conduction band minima (CBM) of N-SnO<sub>2</sub> CE. The result is consistent with Mott-Schottky results obtained. The overall device photovoltaic performance was further increased by applying urea-pretreatment of SnO<sub>2</sub> with different wt%. For U3-SnO<sub>2</sub> CE-based device, PCE % value increased from ~ 7.1% to ~ 9.04% due to the increase of all photovoltaic parameters, *FF*, *V<sub>OC</sub>* and *J<sub>SC</sub>* and this improvement is attributed to the creation more oxygen vacancies after applying urea pre-treatment which allows more electrons to reach electrolyte for more efficient I<sub>3</sub><sup>-</sup> reduction and hence better overall device performance. This improvement was even increased for U5-WO<sub>3</sub> CE based device due to higher wt% of urea pre-treatment and hence more oxygen vacancies to facilitate more electrons for more efficient reduction of I<sub>3</sub><sup>-</sup> ions. Fill factor was significantly increased to 63.7% and ~ 65.1% as well as *V<sub>OC</sub>* value was increased to 0.81 V and 0.83 V

for U5- SnO<sub>2</sub> and U9-SnO<sub>3</sub>CEs based devices, respectively. As expected from Mott-Schottky, Cyclic voltammetry, and EIS measurements, U9-SnO<sub>2</sub> CE based device has the optimum overall PCE % value due to the highest catalytic activity of U9-SnO<sub>2</sub> CE. Beyond this optimum urea wt%, the overall catalytic performance decreased by increasing urea wt% in case of U16-SnO<sub>2</sub> and U33-SnO<sub>2</sub> CEs and therefore, the overall device performance will decrease. Short circuit current values ( $J_{SC}$ ) does not change significantly for the different types of CEs because  $J_{SC}$  value would change mainly depends on upon to the dye sensitizer. The optimum device performance was for U9-SnO<sub>2</sub> CE based device with PCE value of ~ 10.41% which is significantly higher than that the device performance for Pt CE with PCE value of ~ 9.5%.

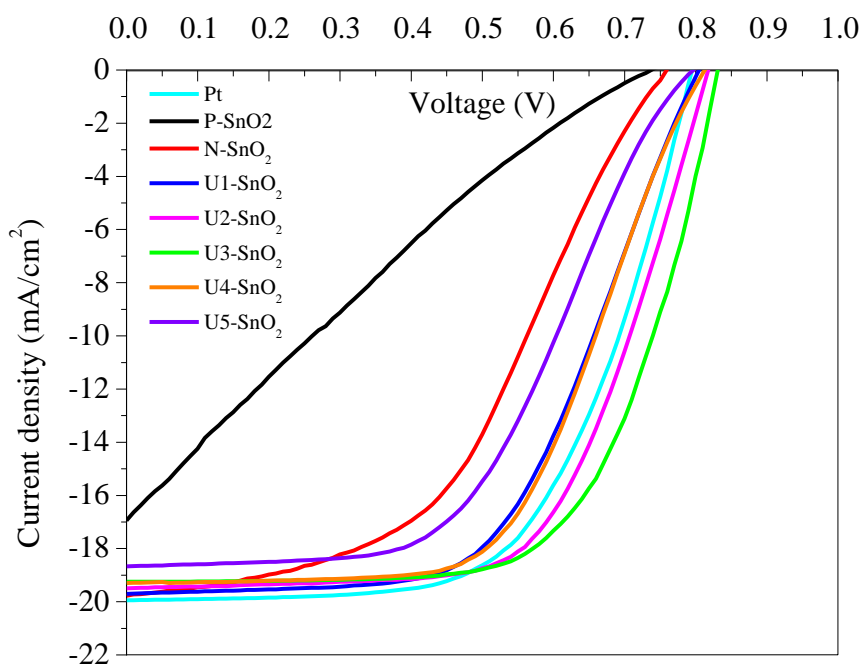


Figure 4.26 Current density-voltage (J-V) for DSSC devices with SnO<sub>2</sub> CEs before and after urea treatment with different urea mass ratios in comparison to Pt CE based devices.



DSSC devices based on U9-SnO<sub>2</sub> CE were fabricated with different thicknesses of 5 μm, 10 μm, 15 μm, 20 μm and 25 μm of CE to determine the optimum thickness of the highest device PCE%. Figure 4.27 shows the *J-V* curves of DSSC devices based on U9-SnO<sub>2</sub> CE with different thicknesses. By increasing the CE thickness, the fill factor of DSSC device increased until 15 μm thickness based device which shows the highest *FF*. The reason for lower *FF* at smaller thicknesses could be attributed to the low interfacial surface area between electrolyte and CE due to the lower thickness and less material leading to lower active sites for triiodide ions reduction. At higher thicknesses, the decrease in *FF* is mainly caused by the increase of series resistance of CE. Photovoltaic parameters were calculated for U9-SnO<sub>2</sub> CE based device with different CE thicknesses and summarized in table 4.4.

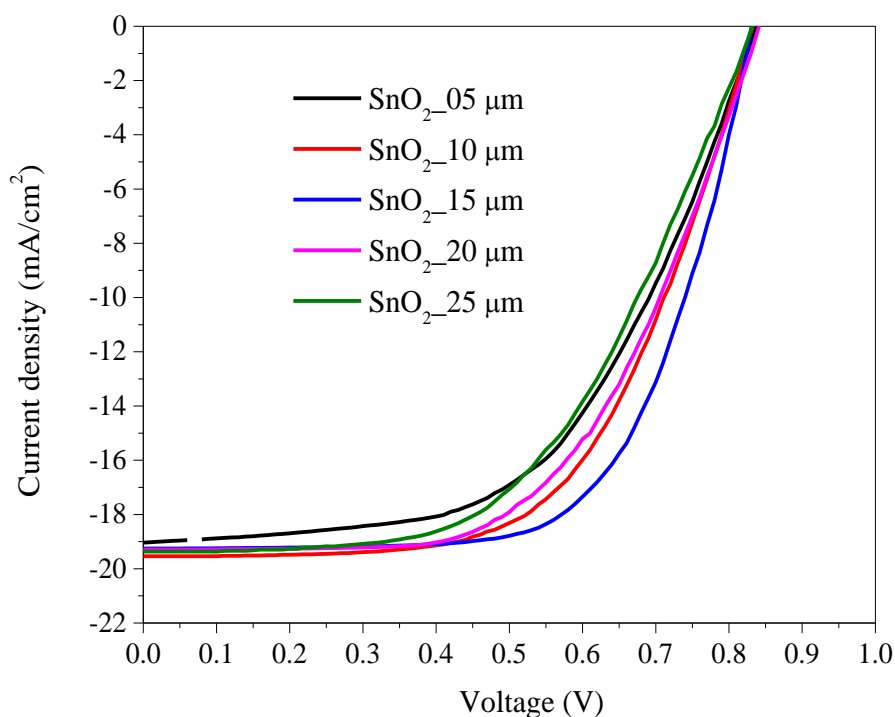


Figure 4.27 Current density-voltage (*J-V*) curves for DSSCs devices with U9-SnO<sub>2</sub> CEs with different thicknesses.

### 4.7.3 Current density-voltage characteristics (J-V) of ZnO CE before and after urea pre-treatment

Figure 4.28 shows J-V curve DSSC device made of the different CEs, pristine ZnO (P- ZnO) CE, N<sub>2</sub>-annealed ZnO (N- ZnO) and N<sub>2</sub>-annealed urea pre-treated ZnO with different urea wt% (U3-ZnO, U5-ZnO, U9-ZnO, U16-ZnO, and U33-ZnO) CEs. All photovoltaics parameters were calculated summarized in table 4.3. Pristine (P-ZnO) CE based device showed the lowest photovoltaics performance with power conversion efficiency (PCE %) of 1.25%, *FF* of 37% and *V<sub>OC</sub>* of ~ 0.33 V. The reason for the low photovoltaic performance of P-ZnO based device is the poor catalytic activity of P-ZnO CE toward triiodide ions reduction and hence inefficient dye regeneration from electrolyte lead to lower *FF*, *V<sub>OC</sub>*, and *J<sub>SC</sub>* values. The photovoltaic performance was significantly increased for N<sub>2</sub>-annealed ZnO (N-ZnO) CE based device. The overall power conversion efficiency (PCE %) value jumped from ~ 1.25% to ~ 3.3%. The value of *FF* increased slightly to 34.1% by the CE in N<sub>2</sub> atmosphere. This improvement in *FF* is attributed to the introduction of oxygen vacancies which facilitate the electron transfer from CE to the electrolyte. The value of *V<sub>OC</sub>* also was slightly increased from ~ 0.33V to ~ 0.78V due to the increase of electron affinity after annealing in N<sub>2</sub> leading to down shift of conduction band minima (CBM) of N-SnO<sub>2</sub> CE. The result is consistent with Mott-Schottky results obtained. The overall device photovoltaic performance was further increased by applying urea-pretreatment of SnO<sub>2</sub> with different wt%. For U3-ZnO CE-based device, PCE % value increased from ~ 3.3% to ~ 4.66% due to the increase of all photovoltaic parameters, *FF*, *V<sub>OC</sub>* and *J<sub>SC</sub>* and this improvement is attributed to the creation more oxygen vacancies after applying urea pre-treatment which allows more electrons to reach electrolyte for more

efficient  $I_3^-$  reduction and hence better overall device performance. This improvement was even increased for U5-ZnO and U9-ZnO and U16-ZnO CE based devices due to higher wt% of urea pre-treatment and hence more oxygen vacancies to facilitate more electrons for more efficient reduction of  $I_3^-$  ions. Fill factor was significantly increased to  $\sim 41.6\%$ ,  $\sim 43.7\%$ , and  $67.1\%$ , as well as  $V_{OC}$  value, was increased to 0.77 V, 0.79 V and 0.82 V for U5-ZnO and U9-ZnO and U16-ZnO CEs based devices, respectively. As expected from Mott-Schottky, Cyclic voltammetry, and EIS measurements, U16-ZnO CE based device has the optimum overall PCE % value due to the highest catalytic activity of U16-ZnO CE. Beyond this optimum urea wt%, the overall catalytic performance decreased by increasing urea wt% in case of U33-SnO<sub>2</sub> CE and therefore, the overall device performance will decrease. Short circuit current values ( $J_{SC}$ ) does not change significantly for the different types of CEs because  $J_{SC}$  value would change mainly depends on upon to the dye sensitizer. The optimum device performance was for U16-ZnO CE based device with PCE value of  $\sim 10.46\%$  which is significantly higher than that the device performance for Pt CE with PCE value of  $\sim 9.5\%$ .

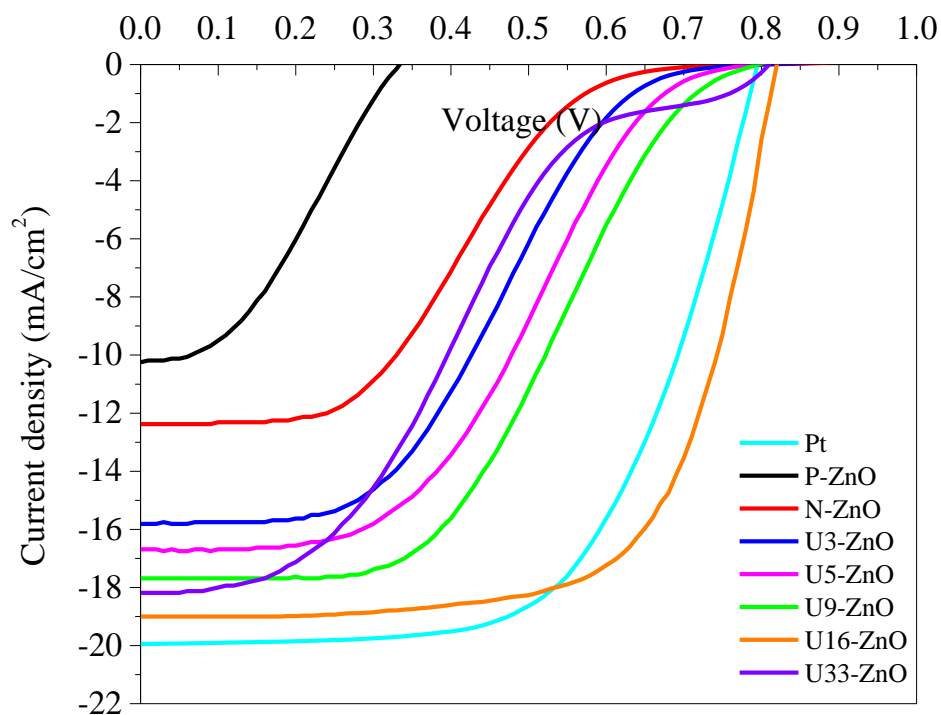


Figure 4.28 Current density-voltage ( $J$ - $V$ ) curves for DSSC devices with ZnO CEs before and after urea treatment with different urea mass ratios in comparison to Pt CE based devices.

DSSC devices based on U16-ZnO CE were fabricated with different thicknesses of 5  $\mu\text{m}$ , 10  $\mu\text{m}$ , 15  $\mu\text{m}$ , 20  $\mu\text{m}$  and 25  $\mu\text{m}$  of CE to determine the optimum thickness of the highest device PCE%. Figure 4.29 shows the  $J$ - $V$  curves of DSSC devices based on U9-ZnO CE with different thicknesses. By increasing the CE thickness, the fill factor of DSSC device increased until 15  $\mu\text{m}$  thickness based device which shows the highest  $FF$ . The reason for lower  $FF$  at smaller thicknesses could be attributed to the low interfacial surface area between electrolyte and CE due to the lower thickness and less material leading to lower active sites for triiodide ions reduction. At higher thicknesses, the decrease in  $FF$  is

mainly caused by the increase of series resistance of CE. Photovoltaic parameters were calculated for U16-ZnO CE based device with different CE thicknesses and summarized in table 4.4.

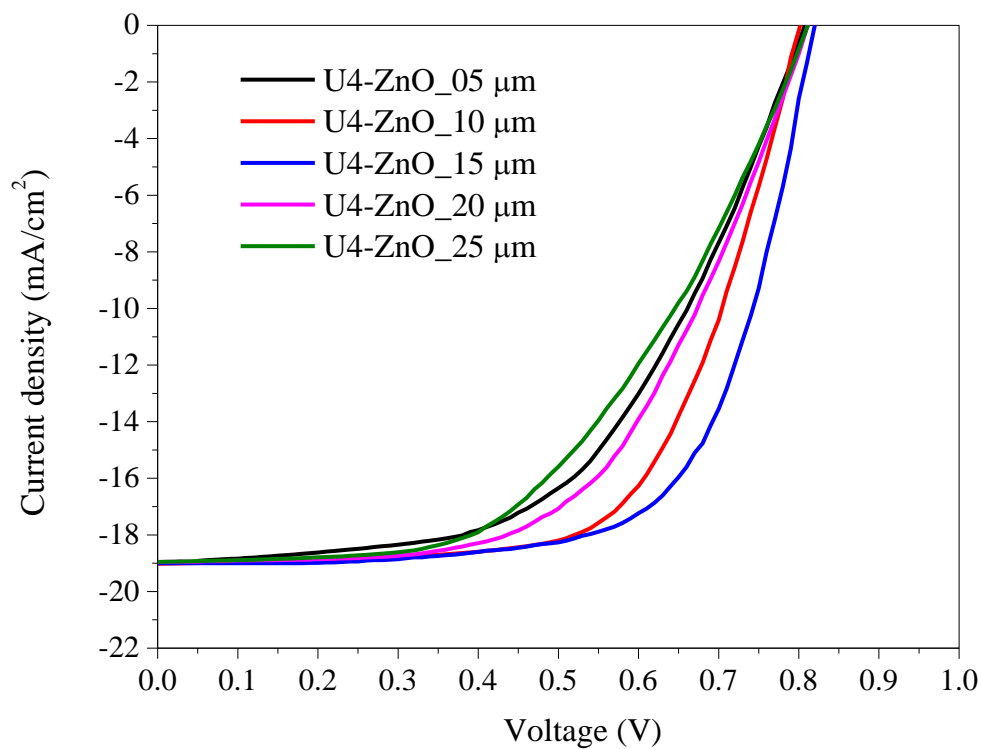


Figure 4.28 Current density-voltage ( $J$ - $V$ ) curves for DSSCs devices with U16-ZnO CEs with different thicknesses.

Table 4.3 Performance of DSSC devices based on WO<sub>3</sub>, SnO<sub>2</sub> and ZnO CEs before and after urea treatment with different mass ratios in comparison to Pt CE based device.

Counter electrode	$J_{SC}$ (mA/cm <sup>2</sup> )	$V_{OC}$ (volt)	$FF$ %	$PCE$ %
<b>Pt</b>	19.94	0.78	61	<b>9.5</b>
P-WO <sub>3</sub>	17.74	0.78	24	3.3
N-WO <sub>3</sub>	18.93	0.8	55	8.44
U3-WO <sub>3</sub>	20.51	0.84	56	9.79
<b>U5-WO<sub>3</sub></b>	20.03	0.85	65	<b>11.1</b>
U9-WO <sub>3</sub>	18.75	0.85	61.7	9.83
U16-WO <sub>3</sub>	18.1	0.84	55.1	8.4
U33-WO <sub>3</sub>	18.56	0.79	44	6.49
P-SnO <sub>2</sub>	16.95	0.73	22	2.76
N-SnO <sub>2</sub>	19.77	0.75	47.8	7.1
U3-SnO <sub>2</sub>	19.7	0.8	57.3	9.04
U5-SnO <sub>2</sub>	19.5	0.81	63.7	10.06
<b>U9-SnO<sub>2</sub></b>	19.25	0.83	65.1	<b>10.41</b>
U16-SnO <sub>2</sub>	19.3	0.81	58.9	9.21
U33-SnO <sub>2</sub>	18.66	0.79	52.7	7.77
P-ZnO	10.25	0.33	37	1.25
N-ZnO	12.37	0.78	34	3.3
U3-ZnO	15.81	0.79	37.3	4.66
U5-ZnO	16.75	0.79	41.6	5.51
U9-ZnO	17.68	0.79	43.68	5.95
<b>U16-ZnO</b>	19	0.82	67.1	<b>10.46</b>
U33-ZnO	18.1	0.81	30	4.4

Table 4.4. The performance of DSSCs with different thicknesses of CE for both U5-WO<sub>3</sub>, U9-SnO<sub>2</sub> and U16-ZnO under illumination.

<b>CE</b>	<b>Thickness (<math>\mu\text{m}</math>)</b>	<b><math>J_{sc}</math> (mA/cm<sup>2</sup>)</b>	<b><math>V_{oc}</math> (V)</b>	<b><math>FF</math> %</b>	<b><math>PCE</math> %</b>
U5-WO <sub>3</sub>	5	19.27	0.83	56.4	9.022
	10	20	0.84	60.6	10.2
	<b>15</b>	<b>20.03</b>	<b>0.85</b>	<b>64.66</b>	<b>11%</b>
	20	19.45	0.85	59.1	9.77
	25	19.45	0.84	58.23	9.51
U9-SnO <sub>2</sub>	5	19.03	0.83	55.6	8.78
	10	19.53	0.83	59.7	9.67
	<b>15</b>	<b>19.25</b>	<b>0.83</b>	<b>65.18</b>	<b>10.41</b>
	20	19.29	0.84	57.2	9.27
	25	19.36	0.83	53.73	8.63
U16-ZnO	5	18.89	0.8	54.7	8.31
	10	19	0.8	64.3	9.79
	<b>15</b>	<b>19</b>	<b>0.82</b>	<b>67.1</b>	<b>10.46</b>
	20	18.96	0.81	57	8.75
	25	18.95	0.81	50.8	7.79

## Chapter 5: Conclusions

### 5.1 Summary

The demand for energy is increasing, and the need for renewable, sustainable sources of energy is vital to replace the fossil fuel energy source. Photovoltaic cells are environmentally clean compared to the conventional fossil fuels as sources of energy. However, the materials and fabrication costs of the conventional Si-based solar cells are high, thus making solar electricity more expensive than that of fossil fuels. Dye-sensitized solar cells (DSSCs) can be cost-effective alternative to the high-cost commercial Si solar cells due to its low-cost materials and simple fabrication methods.

The most widely used material as CEs was platinum (Pt) in DSSCs during last two decades. Because of its low abundance and high cost, alternative materials were searched to replace Pt as CE. Other materials such as carbon based materials and polymer were used as an alternative to Pt. Metal oxide materials such as  $\text{WO}_3$ ,  $\text{SnO}_2$ ,  $\text{Fe}_2\text{O}_3$ ,  $\text{MoO}_3$ , and  $\text{Nb}_2\text{O}_5$  were investigated and used as CEs for DSSCs devices. Commercial metal oxides were found to have oxygen vacancy defects which make them good candidates as catalysts in DSSC device. They have lower cost and higher abundance compared to the expensive and rare Pt. To improve the catalytic performance of metal oxides, many researchers tried to anneal metal oxides in an inert gas such as  $\text{N}_2$  at high temperatures of 470-500 °C. By annealing, oxygen vacancies inside metal oxides were introduced hence increasing the active sites for triiodide ions reduction. However, it was found that the overall catalytic performance of metal oxides is still lower than Pt CEs. Also, metal oxides were annealed at the same temperature range under  $\text{H}_2$  environment, and the catalytic performance was found to be improved comparing to annealing under  $\text{N}_2$  gas. Hydrogen was used instead of



$N_2$  due to its capability as reducing gas to introduce more oxygen vacancies and hence increase the overall catalytic performance of metal oxides. The catalytic performance of metal oxides was further increased by annealing in ammonia gas ( $NH_3$ ) atmosphere, and the power conversion efficiency was comparable to the Pt CE based device catalytic performance. However, there was no enough detailed explanation about how ammonia would improve the catalytic activity of metal oxides. In addition, use of ammonia gas is not safe due to the health problems from ammonia. In this dissertation work, a more efficient, controllable and safer method was developed for the first time to optimize and control oxygen vacancies using urea pre-treatment of  $N_2$ -annealed metal oxides with different urea concentrations.

Different mass wt% urea was mixed with metal oxides, binder and surfactant material to make a paste. The paste was doctor bladed on top of cleaned FTO and then annealed in  $N_2$  atmosphere at  $470\text{ }^\circ\text{C}$ . Urea can decompose at high temperature  $\sim 470\text{ }^\circ\text{C}$  to ammonia gas ( $NH_3$ ) and cyanic acid ( $HCNO$ ).  $NH_3$  gas also will decompose at high temperature to produce  $H_2$  and  $N_2$  gases. Increasing the urea wt% pre-treatment will increase the amount of reducing  $H_2$  gas. This helps to remove more oxygen forming a metal oxide and create more oxygen vacancies. By changing urea content, the number of oxygen vacancies could be optimized for optimum CE catalytic performance. Different experimental characterizations were performed. SEM and EDS measurements were conducted for surface morphology and elementary wt% for oxygen atoms. EIS and CV measure nets were performed to measure the catalytic performance of all counter electrodes. Raman spectroscopy was conducted for all metal oxides films to prove the crystallinity degradation of metal oxides by increasing urea pre-treatment. Photovoltaic

characterization such as current density-voltage measurements was also performed for all DSSC devices based on the different counter electrodes.

SEM images for three metal oxides including  $\text{WO}_3$ ,  $\text{SnO}_2$  and  $\text{ZnO}$  show that more pores and voids were created in metal oxide films by increasing urea content. This indicates that more oxygen atoms were released due to the increasing amount of  $\text{H}_2$  gas that reduces metal oxide. The porous structure formed after urea pretreatment is another advantage because it allows more electrolyte to reach the reduction active sites for better catalytic performance. EDS measurement was used to calculate oxygen wt% inside metal oxides before and after urea pre-treatment. The oxygen wt% linearly decreased by increasing the urea wt% which indicated oxygen vacancies were created by increasing the wt% of urea.

Mott-Schottky measurement showed that U5- $\text{WO}_3$ , U9- $\text{SnO}_2$ , and U16- $\text{ZnO}$  CEs pre-treated with 5wt%, 9wt% and 16 wt% of urea have the lowest band bending at the interface between CE. These suggest that CEs are expected to be the optimum CEs regarding the catalytic performance towards electrolyte. Raman spectra show that the characteristics peaks for all metal oxides were reduced in intensity by increasing urea content for pre-treatment. The peaks almost disappear at high wt% of urea, indicating a successful reduction of  $\text{WO}_3$ ,  $\text{SnO}_2$ , and  $\text{ZnO}$  to  $\text{WO}_{3-x}$ ,  $\text{SnO}_{2-x}$ , and  $\text{ZnO}_{1-x}$ . Optical band gap measurement was performed for all investigated metal oxide CEs. The optical band gap values were calculated using *Tauc's* plot. Band gap values were found to decrease linearly with increasing urea wt% for all metal oxides. This decrease was attributed to the creation of oxygen vacancies that can shift both conduction band minima (CBM) and valence band maxima (VBM) levels and hence reducing the band gap. The hypothesis that increasing oxygen vacancies will reduce the band gap was also supported by Mott-

Schottky measurement and a change in the film color before and after urea pre-treatment. The catalytic performance of all investigated CEs was measured using CV and EIS. In cyclic voltammetry, U5-WO<sub>3</sub>, U9-SnO<sub>2</sub> and U16-ZnO CEs pre-treated with 5wt%, 9wt% and 16 wt% of urea have the optimum catalytic activity as expected from Mott-Schottky results. To determine solar cell performance, J-V measurements were conducted for all investigated CEs. In consistent with all previous characterizations, U5-WO<sub>3</sub>, U9-SnO<sub>2</sub>, and U16-ZnO CEs based devices show the optimum PCE of 11.1%, 10.41%, and 10.46%. These are higher than Pt-based device performance of 9.5%. The optimum CE thickness for all three metal oxides was found to be ~ 15 μm.

## **5.2 Conclusion**

Commercial WO<sub>3</sub>, SnO<sub>2</sub>, and ZnO metal oxides were successfully used to replace expensive and rare Pt as CE of DSSCs. Urea pre-treatment was found to be an efficient new technique to control the density of oxygen vacancies in metal oxides in a safer way than using NH<sub>3</sub> gas. Surface morphology of pre-treated metal oxides exhibited more porosity structure than the pristine untreated metal oxide. Mott-Schottky and optical measurements showed that U5-WO<sub>3</sub>, U9-SnO<sub>2</sub>, and U16-ZnO metal oxides have no band bending at the interface between CEs and electrolyte. The optimum catalytic performance was found for U5-WO<sub>3</sub>, U9-SnO<sub>2</sub>, and U16-ZnO CEs. DSSC device performance shows higher PCE values of 11.1%, 10.41% and 10.46% for U5-WO<sub>3</sub>, U9-SnO<sub>2</sub>, and U16-ZnO, respectively compared to Pt-based device of ~ 9.5%.

## **5.3 Future work**

Because band gap of metal oxides reduced significantly by applying urea pre-treatment, this could be an advantage of using urea pre-treated metal oxides as efficient

photocathodes in water splitting and hydrogen gas production in fuel cells. Due to its excellent catalytic performance and porous structure, urea pre-treated metal oxides could also be used as the anode in Li-ion batteries to replace the commercial graphite anode.

## References

- [1] H. Meixner, J. Gerblinger, U. Lampe, and M. Fleischer, "Thin-film gas sensors based on semiconducting metal oxides," *Sensors and Actuators B: Chemical*, vol. 23, pp. 119-125, 1995/02/01 1995.
- [2] X. Fu, L. A. Clark, Q. Yang, and M. A. Anderson, "Enhanced Photocatalytic Performance of Titania-Based Binary Metal Oxides:  $\text{TiO}_2/\text{SiO}_2$  and  $\text{TiO}_2/\text{ZrO}_2$ ," *Environmental Science & Technology*, vol. 30, pp. 647-653, 1996/01/01 1996.
- [3] EIA. (2016, July 30<sup>th</sup> ). *U.S. Energy Information Administration INTERNATIONAL ENERGY OUTLOOK 2014*. Available: <http://www.eia.gov>
- [4] NEI. (2016, July 11th ). *Nuclear Energy Institute NEW NUCLEAR ENERGY FACILITIES*. Available: [www.nei.org](http://www.nei.org)
- [5] NREL. (2016, July 11th ). *U.S. Department of Energy 2014 Renewable Energy Data Book* Available: <http://www.nrel.gov>
- [6] C. Stewart. (July 11th). *Geothermal energy - Effects on the environment* Available: <http://www.teara.govt.nz/en/geothermal-energy/page-5>
- [7] M. Anpo, H. Nakaya, S. Kodama, Y. Kubokawa, K. Domen, and T. Onishi, "Photocatalysis over binary metal oxides. Enhancement of the photocatalytic activity of titanium dioxide in titanium-silicon oxides," *The Journal of Physical Chemistry*, vol. 90, pp. 1633-1636, 1986/04/01 1986.
- [8] A. E. Becquerel, "Recherches sur les effets de la radiation chimique de la lumiere solaire au moyen des courants electriques " *Comptes Rendus de L'Academie des Sciences*, vol. 9, pp. 145-149, 1839.

- [9] X. Wang, K. Maeda, A. Thomas, K. Takanabe, G. Xin, J. M. Carlsson, *et al.*, "A metal-free polymeric photocatalyst for hydrogen production from water under visible light," *Nat Mater*, vol. 8, pp. 76-80, 01/print 2009.
- [10] J. Zhang, Y. Wu, M. Xing, S. A. K. Leghari, and S. Sajjad, "Development of modified N doped TiO<sub>2</sub> photocatalyst with metals, nonmetals and metal oxides," *Energy & Environmental Science*, vol. 3, pp. 715-726, 2010.
- [11] J. Zhao, A. Wang, and M. A. Green, "19.8% efficient, "honeycomb" textured, multicrystalline and 24.4% monocrystalline silicon solar cell," *Applied Physics Letters*, vol. 73, pp. 1991-1993, 1998.
- [12] X. Chen, L. Liu, P. Y. Yu, and S. S. Mao, "Increasing Solar Absorption for Photocatalysis with Black Hydrogenated Titanium Dioxide Nanocrystals," *Science*, vol. 331, pp. 746-750, 2011.
- [13] A. Naldoni, M. Allieta, S. Santangelo, M. Marelli, F. Fabbri, S. Cappelli, *et al.*, "Effect of Nature and Location of Defects on Bandgap Narrowing in Black TiO<sub>2</sub> Nanoparticles," *Journal of the American Chemical Society*, vol. 134, pp. 7600-7603, 2012/05/09 2012.
- [14] A. Sinhamahapatra, J.-P. Jeon, J. Kang, B. Han, and J.-S. Yu, "Oxygen-Deficient Zirconia (ZrO<sub>2-x</sub>): A New Material for Solar Light Absorption," *Scientific Reports*, vol. 6, p. 27218, 06/06/online 2016.
- [15] A. G. Aberle, "Thin-film solar cells," *Thin Solid Films*, vol. 517, pp. 4706-4710, 2009.
- [16] P. Lechner and H. Schade, "Photovoltaic thin-film technology based on hydrogenated amorphous silicon," *Progress in Photovoltaics: Research and Applications*, vol. 10, pp. 85-97, 2002.
- [17] P. Reinhard, A. Chirilă, P. Blösch, F. Pianezzi, S. Nishiwaki, S. Buecheler, *et al.*, "Review of progress toward 20% efficiency flexible CIGS solar cells and manufacturing issues of solar modules," *IEEE Journal of Photovoltaics*, vol. 3, pp. 572-580, 2013.

- [18] C. Candelise, M. Winkler, and R. Gross, "Implications for CdTe and CIGS technologies production costs of indium and tellurium scarcity," *Progress in Photovoltaics: Research and Applications*, vol. 20, pp. 816-831, 2012.
- [19] H. Gerischer, M. Michel-Beyerle, F. Reberndorf, and H. Tributsch, "Sensitization of charge injection into semiconductors with large band gap," *Electrochimica Acta*, vol. 13, pp. 1509-1515, 1968.
- [20] (July 11th ). U. S. Department of energy. "The History of Solar". Available: [http://www1.eere.energy.gov/solar/pdfs/solar\\_timeline.pdf](http://www1.eere.energy.gov/solar/pdfs/solar_timeline.pdf)
- [21] B. Oregan and M. Gratzel, "A Low-Cost, High-Efficiency Solar-Cell Based on Dye-Sensitized Colloidal TiO<sub>2</sub> Films," *Nature*, vol. 353, pp. 737-740, Oct 24 1991.
- [22] M. K. Nazeeruddin, A. Kay, I. Rodicio, R. Humphry-Baker, E. Mueller, P. Liska, *et al.*, "Conversion of light to electricity by cis-X<sub>2</sub>bis(2,2'-bipyridyl-4,4'-dicarboxylate)ruthenium(II) charge-transfer sensitizers (X = Cl<sup>-</sup>, Br<sup>-</sup>, I<sup>-</sup>, CN<sup>-</sup>, and SCN<sup>-</sup>) on nanocrystalline titanium dioxide electrodes," *J. Am. Chem. Soc.*, vol. 115, pp. 6382-6390, 1993.
- [23] R. Chandra Sekhar, H. Manu, A. Govindaraj, and C. N. R. Rao, "Ammonia sensors based on metal oxide nanostructures," *Nanotechnology*, vol. 18, p. 205504, 2007.
- [24] M. K. Nazeeruddin, P. Pechy, T. Renouard, S. M. Zakeeruddin, R. Humphry-Baker, P. Comte, *et al.*, "Engineering of Efficient Panchromatic Sensitizers for Nanocrystalline TiO<sub>2</sub>-Based Solar Cells," *J. Am. Chem. Soc.*, vol. 123, pp. 1613-1624, 2001.
- [25] S. Ito, P. Liska, P. Comte, R. Charvet, P. Pechy, U. Bach, *et al.*, "Control of dark current in photoelectrochemical (TiO<sub>2</sub>/I<sup>-</sup>/I<sub>3</sub><sup>-</sup>) and dye-sensitized solar cells," *Chemical Communications*, pp. 4351-4353, 2005.

- [26] A. Kay and M. Grätzel, "Low cost photovoltaic modules based on dye sensitized nanocrystalline titanium dioxide and carbon powder," *Solar Energy Materials and Solar Cells*, vol. 44, pp. 99-117, 1996.
- [27] T. N. Murakami, S. Ito, Q. Wang, M. K. Nazeeruddin, T. Bessho, I. Cesar, *et al.*, "Highly efficient dye-sensitized solar cells based on carbon black counter electrodes," *Journal of the Electrochemical Society*, vol. 153, pp. A2255-A2261, 2006.
- [28] H. Li, J. Xu, Y. Zhu, X. Chen, and Q. Xiang, "Enhanced gas sensing by assembling Pd nanoparticles onto the surface of SnO<sub>2</sub> nanowires," *Talanta*, vol. 82, pp. 458-463, 7/15/2010.
- [29] T. Waitz, T. Wagner, T. Sauerwald, C.-D. Kohl, and M. Tiemann, "Ordered Mesoporous In<sub>2</sub>O<sub>3</sub>: Synthesis by Structure Replication and Application as a Methane Gas Sensor," *Advanced Functional Materials*, vol. 19, pp. 653-661, 2009.
- [30] K. Imoto, K. Takahashi, T. Yamaguchi, T. Komura, J. Nakamura, and K. Murata, "High-performance carbon counter electrode for dye-sensitized solar cells," *Solar Energy Materials and Solar Cells*, vol. 79, pp. 459-469, Sep 30 2003.
- [31] K. Suzuki, M. Yamaguchi, M. Kumagai, and S. Yanagida, "Application of carbon nanotubes to counter electrodes of dye-sensitized solar cells," *Chemistry Letters*, vol. 32, pp. 28-29, Jan 5 2003.
- [32] N. Pinna, G. Neri, M. Antonietti, and M. Niederberger, "Nonaqueous Synthesis of Nanocrystalline Semiconducting Metal Oxides for Gas Sensing," *Angewandte Chemie*, vol. 116, pp. 4445-4449, 2004.
- [33] C. Wang, L. Yin, L. Zhang, D. Xiang, and R. Gao, "Metal Oxide Gas Sensors: Sensitivity and Influencing Factors," *Sensors*, vol. 10, p. 2088, 2010.



- [34] M. K. Debanath and S. Karmakar, "Study of blueshift of optical band gap in zinc oxide (ZnO) nanoparticles prepared by low-temperature wet chemical method," *Materials Letters*, vol. 111, pp. 116-119, 11/15/ 2013.
- [35] V. Srikant and D. R. Clarke, "On the optical band gap of zinc oxide," *Journal of Applied Physics*, vol. 83, pp. 5447-5451, 1998.
- [36] N. K. Elumalai, A. Saha, C. Vijila, R. Jose, Z. Jie, and S. Ramakrishna, "Enhancing the stability of polymer solar cells by improving the conductivity of the nanostructured MoO<sub>3</sub> hole-transport layer," *Physical Chemistry Chemical Physics*, vol. 15, pp. 6831-6841, 2013.
- [37] N. G. Park and K. Kim, "Transparent solar cells based on dye-sensitized nanocrystalline semiconductors," *physica status solidi (a)*, vol. 205, pp. 1895-1904, 2008.
- [38] A. J. Bard, L. R. Faulkner, J. Leddy, and C. G. Zoski, *Electrochemical methods: fundamentals and applications* vol. 2: Wiley New York, 1980.
- [39] A. Hauch and A. Georg, "Diffusion in the electrolyte and charge-transfer reaction at the platinum electrode in dye-sensitized solar cells," *Electrochimica Acta*, vol. 46, pp. 3457-3466, 2001.
- [40] A. Aboagye, H. Elbohy, A. D. Kelkar, Q. Qiao, J. Zai, X. Qian, *et al.*, "Electrospun carbon nanofibers with surface-attached platinum nanoparticles as cost-effective and efficient counter electrode for dye-sensitized solar cells," *Nano Energy*, vol. 11, pp. 550-556, 1// 2015.
- [41] H. Elbohy, A. Aboagye, S. Sigdel, Q. Wang, M. H. Sayyad, L. Zhang, *et al.*, "Graphene-embedded carbon nanofibers decorated with Pt nanoneedles for high efficiency dye-sensitized solar cells," *Journal of Materials Chemistry A*, vol. 3, pp. 17721-17727, 2015.

- [42] K. P. Gattu, K. Ghule, A. A. Kashale, V. B. Patil, D. M. Phase, R. S. Mane, *et al.*, "Bio-green synthesis of Ni-doped tin oxide nanoparticles and its influence on gas sensing properties," *RSC Advances*, vol. 5, pp. 72849-72856, 2015.
- [43] L. Kavan, J. H. Yum, and M. Gratzel, "Optically Transparent Cathode for Dye-Sensitized Solar Cells Based on Graphene Nanoplatelets," *ACS Nano*, vol. 5, pp. 165-172, Jan 2011.
- [44] J. D. Roy-Mayhew, D. J. Bozym, C. Punckt, and I. A. Aksay, "Functionalized Graphene as a Catalytic Counter Electrode in Dye-Sensitized Solar Cells," *ACS Nano*, vol. 4, pp. 6203-6211, Oct 2010.
- [45] G. Mohan Kumar, P. Ilanchezhian, J. Kawakita, M. Subramanian, and R. Jayavel, "Magnetic and optical property studies on controlled low-temperature fabricated one-dimensional Cr doped ZnO nanorods," *CrystEngComm*, vol. 12, pp. 1887-1892, 2010.
- [46] S. Kuriakose, B. Satpati, and S. Mohapatra, "Enhanced photocatalytic activity of Co doped ZnO nanodisks and nanorods prepared by a facile wet chemical method," *Physical Chemistry Chemical Physics*, vol. 16, pp. 12741-12749, 2014.
- [47] Z. Lenzion-Bielun, U. Narkiewicz, and W. Arabczyk, "Cobalt-based Catalysts for Ammonia Decomposition," *Materials*, vol. 6, p. 2400, 2013.
- [48] C. Prajapati and P. Sahay, "Studies on metal-oxide semiconductor ZnO as a hydrogen gas sensor," *Journal of Nano-and Electronic Physics*, vol. 3, p. 714, 2011.
- [49] M. M. Y. A. Alsaif, S. Balendhran, M. R. Field, K. Latham, W. Wlodarski, J. Z. Ou, *et al.*, "Two dimensional  $\alpha$ -MoO<sub>3</sub> nanoflakes obtained using solvent-assisted grinding and sonication method: Application for H<sub>2</sub> gas sensing," *Sensors and Actuators B: Chemical*, vol. 192, pp. 196-204, 3/1/ 2014.
- [50] H. Gu, Z. Wang, and Y. Hu, "Hydrogen gas sensors based on semiconductor oxide nanostructures," *Sensors*, vol. 12, pp. 5517-5550, 2012.

- [51] C. S. Sluder, J. M. Storey, S. A. Lewis, and L. A. Lewis, "Low temperature urea decomposition and SCR performance," SAE Technical Paper 0148-7191, 2005.
- [52] T. E. Bell and L. Torrente-Murciano, "H<sub>2</sub> Production via Ammonia Decomposition Using Non-Noble Metal Catalysts: A Review," *Topics in Catalysis*, vol. 59, pp. 1438-1457, 2016.
- [53] G. r. Li, F. Wang, Q. w. Jiang, X. p. Gao, and P. w. Shen, "Carbon Nanotubes with Titanium Nitride as a Low-Cost Counter-Electrode Material for Dye-Sensitized Solar Cells," *Angewandte Chemie International Edition*, vol. 49, pp. 3653-3656, 2010.
- [54] X. Mei, S. J. Cho, B. Fan, and J. Ouyang, "High-performance dye-sensitized solar cells with gel-coated binder-free carbon nanotube films as counter electrode," *Nanotechnology*, vol. 21, p. 395202, 2010.
- [55] Q. Jiang, G. Li, S. Liu, and X. Gao, "Surface-nitrided nickel with bifunctional structure as low-cost counter electrode for dye-sensitized solar cells," *The Journal of Physical Chemistry C*, vol. 114, pp. 13397-13401, 2010.
- [56] E. Ramasamy, W. J. Lee, D. Y. Lee, and J. S. Song, "Nanocarbon counterelectrode for dye sensitized solar cells," *Applied Physics Letters*, vol. 90, p. 173103, 2007.
- [57] L. R. F. Allen J. Bard, *Electrochemical Methods: Fundamentals and Applications, 2nd Edition*: Hoboken,NJ, 2001.
- [58] T. Matsubara, R. Sakaguchi, H. Nagai, K. Aramaki, and A. Katagiri, "Measurement and analysis of the series resistance in a dye-sensitized solar cell," *Electrochemistry*, vol. 73, pp. 60-66, 2005.
- [59] D. K. Schroder, *Semiconductor material and device characterization*: John Wiley & Sons, 2006.
- [60] S. O. Kapap, *Principles of Electronic Materials and Devices*: New Delhi: Tata McGraw Hill Education Private limited, 2007.

- [61] NREL. (2016, July 30<sup>th</sup>). *Reference Solar Spectral Irradiance: Air Mass 1.5*. Available: <http://rredc.nrel.gov/solar/spectra/am1.5/>
- [62] J. Zhao, Wang, A. and Green, M. A., "24.5% Efficiency silicon PERT cells on MCZ substrates and 24.7% efficiency PERL cells on FZ substrates," *Prog. Photovolt: Res. Appl.*, vol. 7, pp. 471–474, 1999.
- [63] Z. Huang, X. Liu, K. Li, D. Li, Y. Luo, H. Li, *et al.*, "Application of carbon materials as counter electrodes of dye-sensitized solar cells," *Electrochemistry Communications*, vol. 9, pp. 596-598, 2007.
- [64] M. Grätzel, "Conversion of sunlight to electric power by nanocrystalline dye-sensitized solar cells," *Journal of Photochemistry and Photobiology A: Chemistry*, vol. 164, pp. 3-14, 2004.
- [65] K. Hara, *Dye-sensitized solar cells*, in *Handbook of Photovoltaic Science and Engineering*: S. H. A. Luque, Ed., ed: John Wiley & Sons, Ltd, 2003.
- [66] M. Wang, A. M. Anghel, B. t. Marsan, N.-L. Cevey Ha, N. Pootrakulchote, S. M. Zakeeruddin, *et al.*, "CoS Supersedes Pt as Efficient Electrocatalyst for Triiodide Reduction in Dye-Sensitized Solar Cells," *Journal of the American Chemical Society*, vol. 131, pp. 15976-15977, 2009/11/11 2009.
- [67] C. Longo and M.-A. De Paoli, "Dye-sensitized solar cells: a successful combination of materials," *Journal of the Brazilian Chemical Society*, vol. 14, pp. 898-901, 2003.
- [68] M. Grätzel, "Solar energy conversion by dye-sensitized photovoltaic cells," *Inorganic chemistry*, vol. 44, pp. 6841-6851, 2005.
- [69] B. O'regan and M. Grfitzeli, "A low-cost, high-efficiency solar cell based on dye-sensitized," *nature*, vol. 353, pp. 737-740, 1991.

- [70] Y. Kazakevich. (2016, July 30<sup>th</sup>). *Beer-Lambart Law*. Available: <http://www2.chemistry.msu.edu/faculty/reusch/VirtTxtJml/Spectrpy/UV-Vis/spectrum.htm>
- [71] SERC. (2016, July 30<sup>th</sup>). *Single-crystal X-ray Diffraction*. Available: [http://serc.carleton.edu/research\\_education/geochemsheets/techniques/SXD.html](http://serc.carleton.edu/research_education/geochemsheets/techniques/SXD.html)
- [72] J. Zhao, A. Wang, M. A. Green, and F. Ferrazza, "19.8% efficient "honeycomb" textured multicrystalline and 24.4% monocrystalline silicon solar cells," *Applied Physics Letters*, vol. 73, pp. 1991-1993, 1998.
- [73] M. A. Green, J. Zhao, A. Wang, and S. R. Wenham, "Very high efficiency silicon solar cells-science and technology," *IEEE Transactions on electron devices*, vol. 46, pp. 1940-1947, 1999.
- [74] J. Zhao, A. Wang, and M. Green, "24% efficient PERL structure silicon solar cells," in *Photovoltaic Specialists Conference, 1990., Conference Record of the Twenty First IEEE*, 1990, pp. 333-335.
- [75] Renesas. (2016, July 30<sup>th</sup>). *Semiconductor between Conductors and Insulators*. Available: [http://www.renesas.com/edge\\_ol/engineer/02/index.jsp](http://www.renesas.com/edge_ol/engineer/02/index.jsp)
- [76] L. Cheng, Y. Hou, B. Zhang, S. Yang, J. W. Guo, L. Wu, *et al.*, "Hydrogen-treated commercial WO<sub>3</sub> as an efficient electrocatalyst for triiodide reduction in dye-sensitized solar cells," *Chemical Communications*, vol. 49, pp. 5945-5947, 2013.
- [77] G. Wang, Y. Ling, H. Wang, X. Yang, C. Wang, J. Z. Zhang, *et al.*, "Hydrogen-treated WO<sub>3</sub> nanoflakes show enhanced photostability," *Energy & Environmental Science*, vol. 5, pp. 6180-6187, 2012.
- [78] M. Wu, X. Lin, W. Guo, Y. Wang, L. Chu, T. Ma, *et al.*, "Great improvement of catalytic activity of oxide counter electrodes fabricated in N<sub>2</sub> atmosphere for dye-sensitized solar cells," *Chemical Communications*, vol. 49, pp. 1058-1060, 2013.

- [79] P. Uppachai, V. Harnchana, S. Pimanpang, V. Amornkitbamrung, A. P. Brown, and R. M. D. Brydson, "A substoichiometric tungsten oxide catalyst provides a sustainable and efficient counter electrode for dye-sensitized solar cells," *Electrochimica Acta*, vol. 145, pp. 27-33, 11/1/ 2014.
- [80] D. Song, Z. Chen, P. Cui, M. Li, X. Zhao, Y. Li, *et al.*, "NH<sub>3</sub>-treated WO<sub>3</sub> as low-cost and efficient counter electrode for dye-sensitized solar cells," *Nanoscale research letters*, vol. 10, p. 1, 2015.
- [81] C. Longo and M. A. De Paoli, "Dye-sensitized solar cells: A successful combination of materials," *Journal of the Brazilian Chemical Society*, vol. 14, pp. 889-901, Nov-Dec 2003.
- [82] M. Gratzel, "Conversion of sunlight to electric power by nanocrystalline dye-sensitized solar cells," *Journal of Photochemistry and Photobiology a-Chemistry*, vol. 164, pp. 3-14, Jun 1 2004.
- [83] N. Papageorgiou, W. F. Maier, and M. Gratzel, "An Iodine/Triiodide Reduction Electrocatalyst for Aqueous and Organic Media," *Journal of The Electrochemical Society*, vol. 144, pp. 876-884, 1997.
- [84] MSU.EDU. (2016, July 30th). *Visible and Ultraviolet Spectroscopy*. Available: <https://www2.chemistry.msu.edu/faculty/reusch/virttxtjml/spectrpy/uv-vis/spectrum.htm>
- [85] A. K. Hill and L. Torrente-Murciano, "In-situ H<sub>2</sub> production via low temperature decomposition of ammonia: Insights into the role of cesium as a promoter," *International Journal of Hydrogen Energy*, vol. 39, pp. 7646-7654, 5/15/ 2014.
- [86] S. Phanichphant, "Semiconductor Metal Oxides as Hydrogen Gas Sensors," *Procedia Engineering*, vol. 87, pp. 795-802, 2014/01/01 2014.
- [87] W. H. R. Shaw and J. J. Bordeaux, "The Decomposition of Urea in Aqueous Media," *Journal of the American Chemical Society*, vol. 77, pp. 4729-4733, 1955/09/01 1955.

- [88] S. Shubhda, J. Kiran, V. N. Singh, S. Sukhvir, N. Vijayan, D. Nita, *et al.*, "Faster response of NO<sub>2</sub> sensing in graphene–WO<sub>3</sub> nanocomposites," *Nanotechnology*, vol. 23, p. 205501, 2012.
- [89] M. Tiemann, "Porous Metal Oxides as Gas Sensors," *Chemistry – A European Journal*, vol. 13, pp. 8376-8388, 2007.
- [90] G. Korotcenkov, "Metal oxides for solid-state gas sensors: What determines our choice?," *Materials Science and Engineering: B*, vol. 139, pp. 1-23, 4/25/ 2007.
- [91] M. M. Khan, S. F. Adil, and A. Al-Mayouf, "Metal oxides as photocatalysts," *Journal of Saudi Chemical Society*, vol. 19, pp. 462-464, 9// 2015.
- [92] Y. Inoue, "Photocatalytic water splitting by RuO<sub>2</sub>-loaded metal oxides and nitrides with d0- and d10 -related electronic configurations," *Energy & Environmental Science*, vol. 2, pp. 364-386, 2009.
- [93] X. Chen, L. Liu, and F. Huang, "Black titanium dioxide (TiO<sub>2</sub>) nanomaterials," *Chemical Society Reviews*, vol. 44, pp. 1861-1885, 2015.
- [94] X. Chen, L. Liu, P. Yu, and S. Mao, "Increasing solar absorption for photocatalysis with black hydrogenated titanium dioxide nanocrystals," *Science (New York, N.Y.)*, vol. 331, pp. 746-750, 2011.
- [95] S. A. Ansari, M. M. Khan, S. Kalathil, A. Nisar, J. Lee, and M. H. Cho, "Oxygen vacancy induced band gap narrowing of ZnO nanostructures by an electrochemically active biofilm," *Nanoscale*, vol. 5, pp. 9238-9246, 2013.
- [96] M. E. Khan, M. M. Khan, and M. H. Cho, "Fabrication of WO<sub>3</sub> nanorods on graphene nanosheets for improved visible light-induced photocapacitive and photocatalytic performance," *RSC Advances*, vol. 6, pp. 20824-20833, 2016.
- [97] *Schematic of UV- visible spectrophotometer. Ultraviolet–visible spectroscopy*; (2016, July 30<sup>th</sup>), Available from: [http://en.wikipedia.org/wiki/File:Schematic\\_of\\_UV-](http://en.wikipedia.org/wiki/File:Schematic_of_UV-)

*\_visible\_spectrophotometer.png*.

- [98] L. Shi, Y. Xu, and Q. Li, "Controlled fabrication of SnO<sub>2</sub> arrays of well-aligned nanotubes and nanowires," *Nanoscale*, vol. 2, pp. 2104-2108, 2010.
- [99] M. Imai, M. Kikuchi, N. Oka, and Y. Shigesato, "Visible light-induced photocatalytic properties of WO<sub>3</sub> films deposited by dc reactive magnetron sputtering," *Journal of Vacuum Science & Technology A*, vol. 30, p. 031503, 2012.
- [100] J. Li, J. Wang, L. Zhang, and S. Zhang, "Nanocrystalline SnO<sub>2</sub> thin films prepared by anodization of sputtered Sn thin films," *Journal of Vacuum Science & Technology A*, vol. 33, p. 031508, 2015.
- [101] V. Srikant and D. R. Clarke, "On the optical band gap of zinc oxide," *Applied Physics Letters*, vol. 83, pp. 5447-5451, 1998.
- [102] A. Aboagye, H. Elbohy, A. D. Kelkar, Q. Qiao, J. Zai, X. Qian, *et al.*, "Electrospun carbon nanofibers with surface-attached platinum nanoparticles as cost-effective and efficient counter electrode for dye-sensitized solar cells," *Nano Energy*, vol. 11, pp. 550-556, 1// 2015.